Shock and Vibration

Condition Monitoring and Fault Diagnosis of Electrical Drive Systems

Lead Guest Editor: Muhammad Irfan
Guest Editors: Dong Zhen, Nordin Bin Saad, and Nursyarizal Bin Mohd. Nor

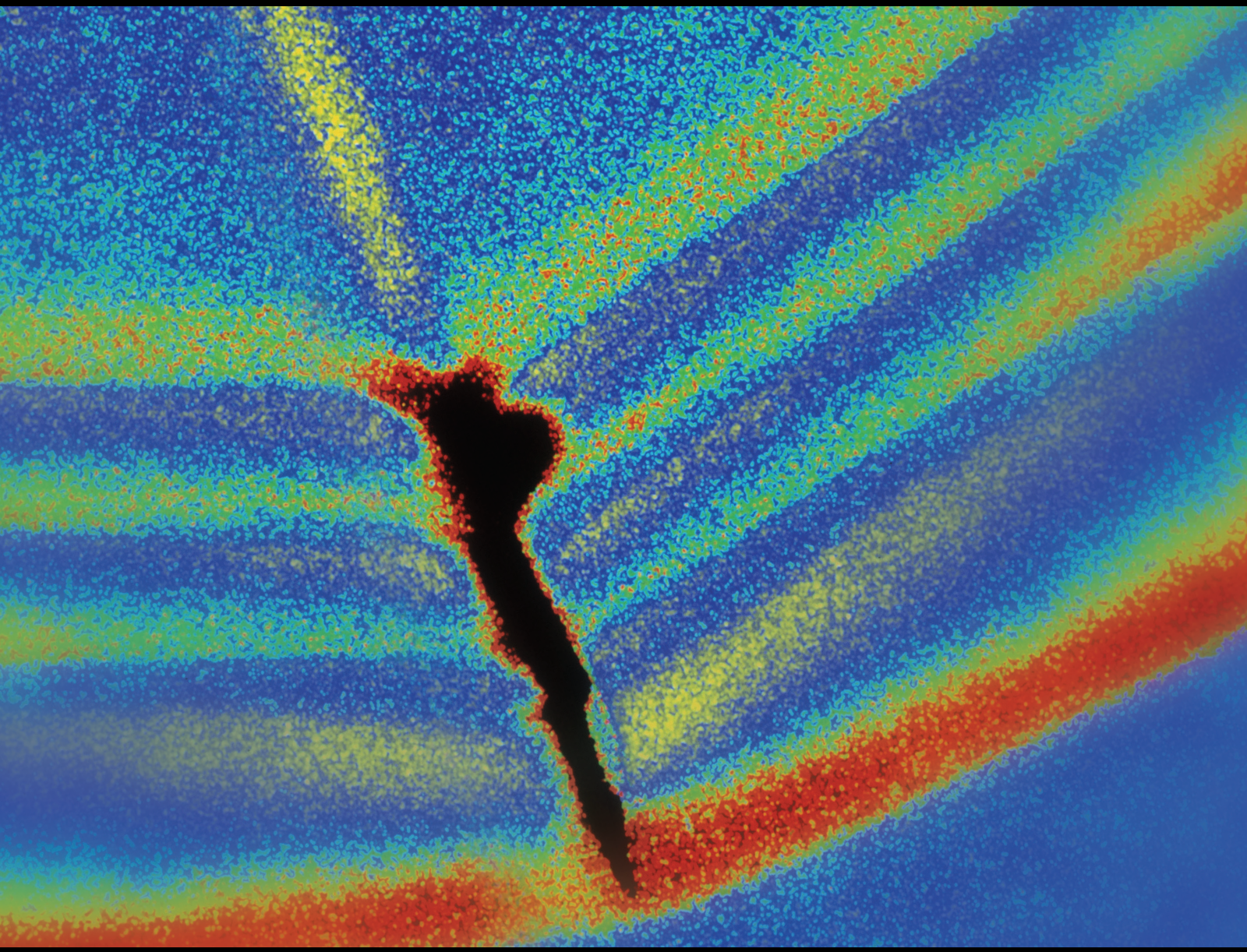

Condition Monitoring and Fault Diagnosis of Electrical Drive Systems

Shock and Vibration

Condition Monitoring and Fault Diagnosis of Electrical Drive Systems

Lead Guest Editor: Muhammad Irfan
Guest Editors: Dong Zhen, Nordin Bin Saad, and Nursyarizal Bin Mohd. Nor

Chief Editor

Associate Editors

Academic Editors

Contents

Hindawi
Shock and Vibration
Volume 2020, Article ID 8832467, 10 pages
https://doi.org/10.1155/2020/8832467

Research Article

Error Signal Differential Term Feedback Enhanced Variable Step Size FxLMS Algorithm for Piezoelectric Active Vibration Control

Weiguang Li, Wei Wang, Bin Li, and Zhichun Yang

School of Aeronautics, Northwestern Polytechnical University, Xi'an 710072, China

Correspondence should be addressed to Wei Wang; wwang@nwpu.edu.cn

Received 30 July 2020; Revised 12 September 2020; Accepted 19 October 2020; Published 6 November 2020

Academic Editor: Muhammad Irfan

FxLMS (Filtered-x Least Mean Square) algorithm is widely used in the field of AVC (active vibration control) for its good convergence and strong adaptability. However, the convergence rate and steady-state error are mutually restricted for the fixed step FxLMS algorithm. Increasing step size μ to accelerate the convergence rate will result in larger steady-state error and even cause control divergence. In this paper, a new DVSFxLMS (error signal Differential term feedback Variable Step size FxLMS) algorithm is proposed by establishing nonlinear function between μ and error signal, while using differential term of the error signal as the feedback control function. Subsequently, a DVSFxLMS controller is designed to carry out the AVC simulation and experiments on cantilever beam with PSA (piezoelectric stack actuator). Simulation and experimental results show that the proposed DVSFxLMS algorithm has faster convergence rate and smaller steady-state error than the traditional FxLMS algorithm, which also has strong antinoise ability and adaptive control ability to quickly track the variable external disturbance.

1. Introduction

Adaptive filter technology has wide range applications in the field of digital signal processing. Compared with a conventional filter, an adaptive filter can adjust characteristics of the filter online according to adaptive filter technology, and obtain the best performance filter by finding the appropriate weight coefficients [1]. The adaptive filter is often divided into two separate parts: one part is a digital filter and the other part is an adaptive algorithm. The digital filter adjusts weight coefficients through the adaptive algorithm to improve its signal processing performance. The schematic diagram of adaptive filtering is shown in Figure 1.

When applying adaptive filtering technology to the field of AVC, a FIR (finite impulse response) filter is usually used as a feedforward controller, called the adaptive controller. The weight coefficients of the adaptive controller are adjusted according to the adaptive algorithm that usually is LMS algorithm, so that the mean square value of the vibration response measured by sensor converges to the minimum direction. The developed FxLMS vibration control algorithm has advantages of good convergence and strong adaptability, and does not depend on the accurate model of controlled structure, which has become one of the hotspots of AVC algorithm research [2–5]. However, in the FxLMS control algorithm, the convergence rate and steady-state error of LMS algorithm are greatly affected by the step size μ. Generally, the larger the step size, the faster the convergence rate, but the steady-state error will also increase; reducing step size can reduce the steady-state error, thereby improving the convergence accuracy, but a smaller step size will significantly reduce the convergence and tracking rate of LMS algorithm [6]. Therefore, the traditional fixed step LMS algorithm contradicts the adjustment of step size in terms of convergence rate, tracking rate, and convergence accuracy. In order to solve this contradiction, it is necessary to adjust the step size μ of LMS algorithm in real time during control process, which is called the variable step size LMS algorithm [7–9]. Gitlin et al. [10] proposed to reduce step size with the increase in number of the algorithm iterations, so as to achieve the purpose of variable step size, but this adjustment rule is only applicable to the time-invariant systems. Qin and Ouyang [11] proposed a variable step size SVSLMS (Sigmoid function Variable Step size LMS)

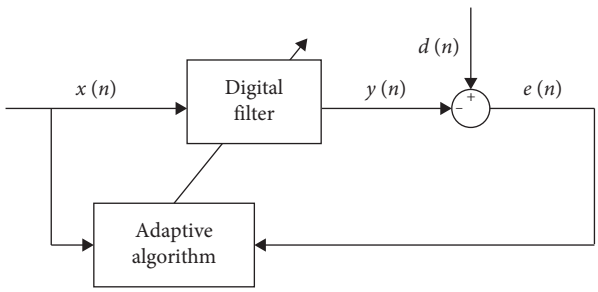

Figure 1: The schematic diagram of adaptive filtering where $x(n)$ is the input signal of adaptive filter; $y(n)$ and $d(n)$ are the output signal and the desired signal of the filter; $e(n)$ is the error signal.

algorithm based on the sigmoid function. By establishing the nonlinear relationship between the step size and error signal, which effectively compensated for the shortcomings in [10]. However, with continuous convergence of the SVSLMS algorithm, the step size changes more and more drastically, which greatly affects the steady-state performance of the SVSLMS algorithm. Gao and Xie [12] proposed a simpler variable step size algorithm $\mu(n) = \beta(1 - \exp(-\alpha|e(n)^2|))$, which overcomes the shortcomings of the sigmoid function in steady-state step adjustment process and also achieves faster convergence rate and smaller steady-state error. However, the current step size of this algorithm is only related to the current error signal, ignoring the effect of previous iteration error signal on the current step size, so it has a certain negative impact on the steady-state error and the convergence rate [13–15]. At the same time, under low SNR (signal noise ratio) environment, the convergence effect of this algorithm is not very ideal, which greatly restricts its application range [16]. In addition, most of the existing variable step size LMS algorithms are mainly used in the fields of system identification [17, 18] and active noise control [19, 20], which are different from their application in the active control of structural vibration [21, 22]. In the field of AVC, the system may be interfered by strong external noise, which makes the algorithm generate larger step size and output too large control signals, causing system instability or even damage. Therefore, when the variable step size FxLMS algorithm is applied to the active control of structural vibration, the robustness to noise interference needs to be considered [23].

In this study, a new variable step size FxLMS algorithm is developed which is called DVSFxLMS algorithm, by establishing nonlinear function between the step size μ and the error signal, while the differential term of the error signal $|e(n) - e(n-1)|$ is adopted as feedback control function in original algorithm, so that the current step size of the proposed algorithm is related to error signal rate. At the same time, the correlation value of the error signal $|e(n)e(n-1)|$ is used instead of the square of the error signal $|e(n)|^2$ to adjust step size. Subsequently, the DVSFxLMS controller is designed to actively control the vibration response of cantilever beam with PSA. The AVC simulation and experiments of piezoelectric cantilever beam under harmonic excitation and harmonic excitation with superimposed noise are carried out, and the adaptability of the DVSFxLMS algorithm is also studied. Simulation and experimental results show that compared with the traditional fixed step FxLMS algorithm, the proposed DVSFxLMS algorithm has faster convergence rate, smaller steady-state error, which also has strong antinoise ability and adaptive control ability to quickly track the variable external disturbances. The block diagram of the proposed research is shown in Figure 2.

2. Design of DVSFxLMS Controller

The LMS algorithm proposed by Widrow and Hoff [24] in 1960 is widely used in the fields of system identification [25], signal processing [26], and adaptive control [27] because of its advantages such as small calculation, easy implementation, and great stability. The LMS algorithm based on the steepest descent method can be summarized as the following iterative process:

$$\begin{cases} e(n) = \mathrm{d}(n) - \widehat{\mathbf{X}}^{\mathrm{T}}(\mathbf{n})\mathbf{W}(\mathbf{n}), \\ \mathbf{W}(\mathbf{n}+\mathbf{1}) = \mathbf{W}(\mathbf{n}) + 2\mu(n)e(n)\widehat{\mathbf{X}}(\mathbf{n}), \end{cases} \tag{1}$$

where $\widehat{\mathbf{X}}(\mathbf{n})$ is the filter input signal vector of length L; $\mathbf{W}(\mathbf{n})$ is the N weight coefficients of the filter at time n; μ is the step size, which determines the steady-state performance and convergence rate of the LMS algorithm. The convergence condition of the LMS algorithm is

$$0 < \mu < \frac{1}{\lambda_{\max}}, \tag{2}$$

where $\lambda_{\max}$ is the maximum eigenvalue of the autocorrelation matrix of $\widehat{\mathbf{X}}(\mathbf{n})$.

The variable step size algorithm can solve the contradiction between step size, convergence rate, and convergence accuracy in the traditional fixed step LMS algorithm. The principle of the variable step size LMS algorithm is to use a larger step size to obtain a faster convergence rate at the initial stage of the convergence or the system changes suddenly; when the algorithm converges to steady state, a smaller step size is used to reduce the steady-state error. At the same time, the calculation amount of the algorithm should be as small as possible, and the parameters that need to be adjusted should be as few as possible to enhance the practicality of the algorithm. Therefore, based on the algorithm in [13], and combining the advantages of the algorithm in [16], while a feedback control function inversely proportional to the differential term of error signal $\Delta e(n) = |e(n) - e(n-1)|$ is introduced, a new variable step size LMS algorithm is proposed in this paper:

$$\begin{cases} \Delta e(n) &= |e(n) - e(n-1)|, \\ \alpha(n) &= p\left(\dfrac{e(n)}{e(n-1)}\right)^2, \\ \mu(n) &= \beta\left(1 - \exp\left(-\alpha(n)\left|\dfrac{e(n)e(n-1)|}{\Delta e}\right|\right)\right). \end{cases} \tag{3}$$

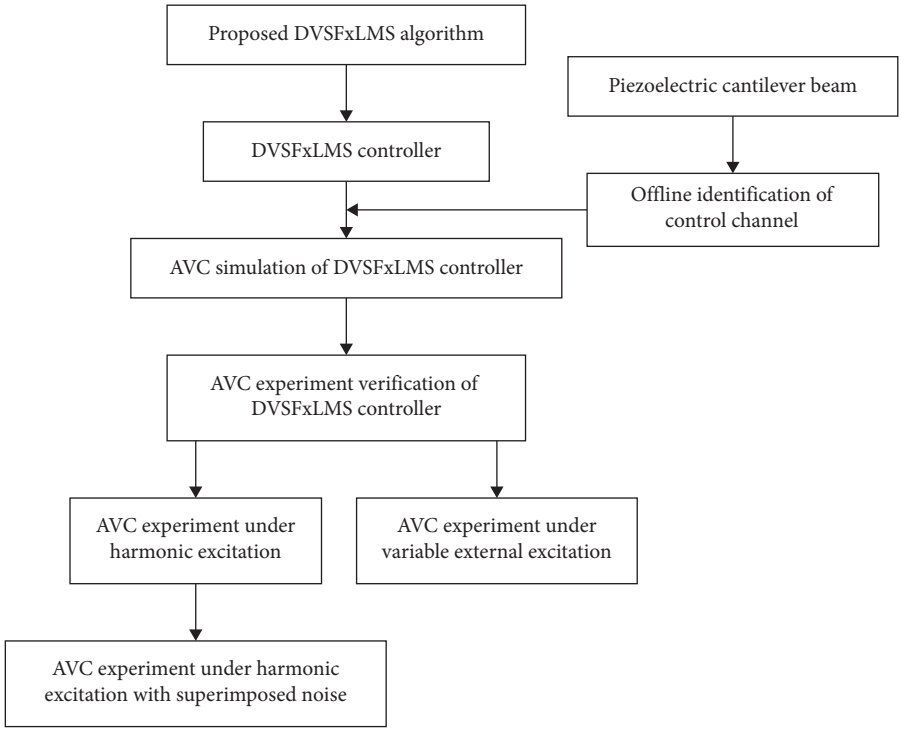

Figure 2: The block diagram of the proposed research.

The proposed algorithm contains two parameters p and β. Among them, the parameter $p > 0$, which controls the shape of the variable step size function; the parameter $\beta > 0$, which controls the value range of the variable step size function. From equation (2), $0 < \mu(n) < 1/\lambda_{\max}$; therefore, $\beta < 1/\lambda_{\max}$. Compared with the original algorithm, equation (3) considers the difference term of the error signal, which reflects the correlation between the step size and the error signal rate. At the same time, the correlation value of the error signal $|e(n)e(n-1)|$ is used instead of the square of the error signal $|e(n)|^2$ to adjust step size, which can further improve the antinoise ability of the variable step size algorithm [16].

The DVSFxLMS vibration control algorithm thus constructed takes the vibration response of the controlled structure caused by external disturbance as starting point, and requires the control signal to drive the actuator to generate control force or moment on the controlled structure, so that the control response will cancel out the response caused by external disturbances at observation points, so as to achieve the purpose of eliminating or reducing the vibration level of the controlled structure. Figure 3 shows the structural diagram of the DVSFxLMS controller.

In Figure 3, $d(n)$ is the structural vibration response at time n when no control signal is applied. The channel $H(z)$ from actuator to sensor is called the control channel, and $\widehat{H}(z)$ is the model obtained from the offline identification of the control channel. $\widehat{y}(n)$ is the structural vibration response caused by the control signal $y(n)$ through the control channel model $\widehat{H}(z)$. $e(n)$ is the structural vibration response error signal.

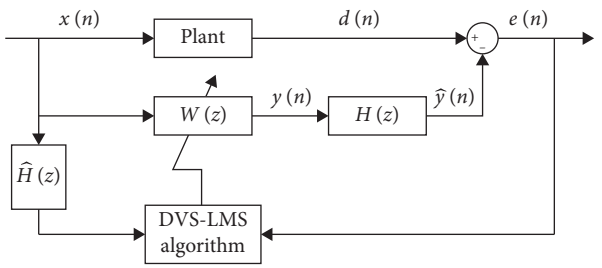

Figure 3: The structural diagram of the DVSFxLMS controller.

In summary, the iterative process of the DVSFxLMS vibration control algorithm is obtained as follows:

$$\begin{cases} y(n) = \widehat{\mathbf{X}}^{\mathbf{T}}(\mathbf{n})\mathbf{W}(\mathbf{n}), \\ e(n) = d(n) - \widehat{y}(n), \\ \Delta e(n) = |e(n) - e(n-1)|, \\ \alpha(n) = p\left(\dfrac{e(n)}{e(n-1)}\right)^2, \\ \mu(n) = \beta\left(1 - \exp\left(-\alpha(n)\left|\dfrac{e(n)e(n-1)}{\Delta e}\right|\right)\right), \\ \mathbf{W}(\mathbf{n}+\mathbf{1}) = \mathbf{W}(\mathbf{n}) + 2\mu(n)e(n)\widehat{\mathbf{X}}(\mathbf{n}). \end{cases} \tag{4}$$

3. AVC Simulation of DVSFxLMS Algorithm

3.1. Piezoelectric Cantilever Beam. In the current simulation, an aluminum alloy cantilever beam is controlled structure, and its dimension is 900 mm × 20 mm × 5 mm. As shown in Figure 4, based on the maximum modal strain energy criterion, the PSA is installed at the root of the cantilever beam to establish vibration control simulation system, in which the observation point A is at the tip of the cantilever beam.

The dimension of PSA is 170 mm × 20 mm × 37 mm, and its total weight is 190 g. The piezoelectric stack used therein is PI™ PICMA® P-840.60, and the parameters of this piezoelectric stack are shown in Table 1 [28]. The PSA is glued to controlled structure through epoxy resin to realize the axial actuation of the piezoelectric stack into a pair of actuating bending moments on the controlled structure.

3.2. Offline Identification of Control Channel. Figure 5 shows the schematic diagram of the control channel offline identification. Applying the excitation signal $x(n)$ to the unknown control channel, then generating an output response $d(n)$, and applying the same excitation signal to the adaptive filter, the filter output is $y(n)$. Then $d(n)$ and $y(n)$ are subtracted to get the identification error signal $e(n)$. The LMS algorithm adjusts the weight coefficients of the filter according to the error signal, and finally makes the output $y(n)$ of the filter close to the output response $d(n)$ of the control channel. At this time, the characteristic of the adaptive filter can be used as an estimate of the control channel.

After the input and output data are obtained, the least square method is used to identify the FIR model for control channel. Whether the results of the model identification meet the needs can be qualitatively evaluated from following two requirements: firstly, comparing the frequency response function of the experimental model and the identification model, which requires the amplitude and phase as consistent as possible; secondly, the iterative curves of weight coefficient are required to smoothly converge during the identification process, and the identification error gradually decreases. If the above requirements are not met, it is necessary to readjust the step size or the order of the FIR model in LMS identification algorithm.

In the control channel offline identification experiment, 28–32 Hz narrow-band random signal is input to the control channel, the output signal of control channel is measured by the acceleration sensor A, and the step size is set to $5E-9$; then, a 1500 order FIR filter model is obtained by the LMS algorithm identification. The identification results are shown in Figure 6. It can be seen from the figure that the frequency response function of the control channel model obtained by offline identification is in good agreement with the experimental curve, and the weight coefficients of the adaptive filter converge smoothly, while the MSE (mean square error) of the identification model gradually approaches zero, which indicates that the FIR filter model identified in the control frequency band can truly reflect the dynamic characteristics of the control channel.

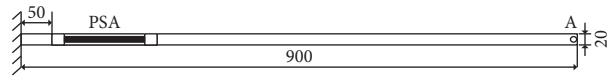

Figure 4: The dimension of the piezoelectric cantilever beam (unit: mm).

Table 1: Parameters of piezoelectric stack.

Parameter	Value
Length × width × height	12 mm × 12 mm × 122 mm
Maximum dynamic displacement	90 μm
Maximum output force	1000 N
Maximum operation voltage	100 V
Elastic compliance coefficient	16.1×10^{-12} m^2/N
Piezoelectric charge coefficient	4×10^{-10} C/N

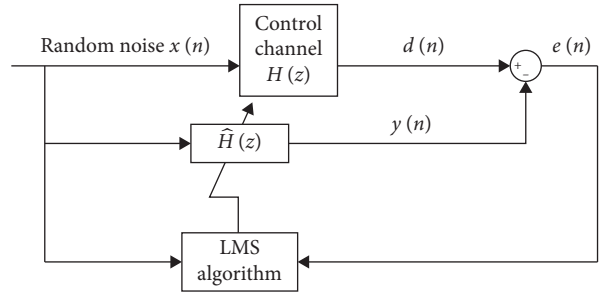

Figure 5: Schematic diagram of the control channel offline identification.

3.3. Simulation of DVSFxLMS Control Algorithm. In order to verify the effectiveness of the proposed DVSFxLMS control algorithm (DVSFxLMS in legends), the traditional fixed step FxLMS control algorithm (fixed FxLMS in legends) is used as a comparison group to compare and study its vibration suppression effect in the active control of piezoelectric cantilever beam harmonic vibration. The control channel model is obtained by offline identification process in Section 3.2. The simulation results are shown in Figure 7. It can be seen from Figure 7 that the DVSFxLMS control algorithm has better vibration suppression performance, compared with the FxLMS control algorithm, it has faster convergence rate and smaller steady-state error.

4. AVC Experiment Verification of DVSFxLMS Algorithm

The AVC experimental diagram of the piezoelectric cantilever beam is shown in Figure 8. The external excitation signal is generated by the Quanser real-time system, and the external excitation signal passes through the output board and amplified by the power amplifier (MB YE5872A), and then input into the electromagnetic exciter (MB Dynamics) to excite the cantilever beam. Structural vibration response is collected by the acceleration sensor (PCB 333B30, sensitivity: 100 mV/g), enters the DVSFxLMS controller through the acceleration signal conditioner (PCB 482C) and Quanser input board, then the control voltage calculated by the DVSFxLMS controller passes through Quanser output

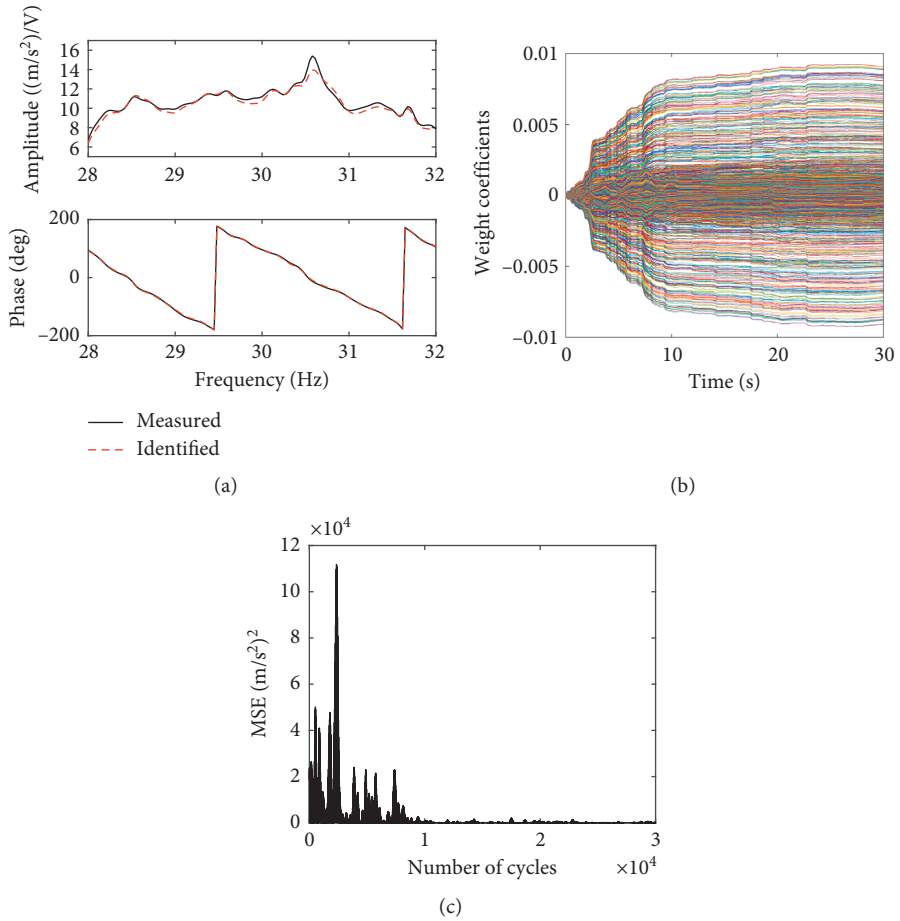

Figure 6: Offline identification results of control channel: (a) comparison of frequency response functions; (b) adaptive filter weight coefficient iteration curves; (c) MSE of the identification model.

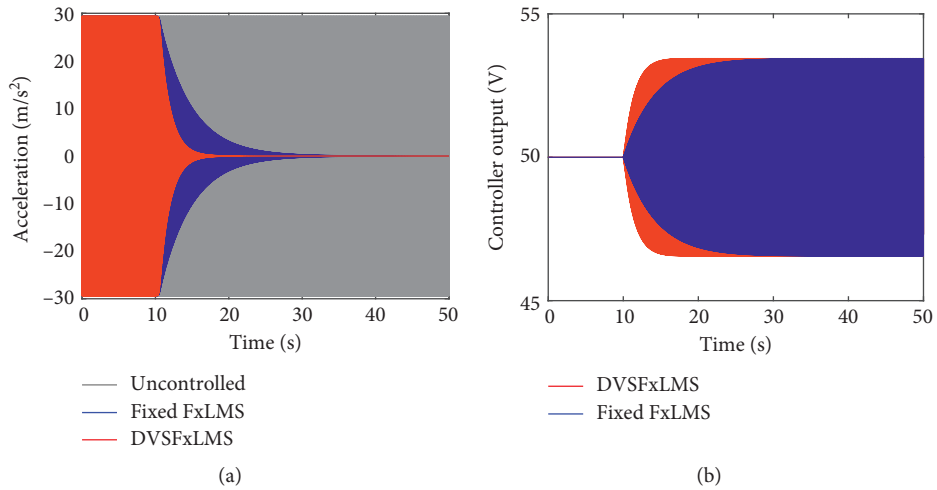

Figure 7: Comparison of simulation results of the DVSFxLMS controller: (a) acceleration response at point A; (b) output voltage.

board, which is amplified by the power amplifier (PA-V-M4) and drive the PSA to control the cantilever beam, thereby achieving active control of the cantilever beam vibration response. The setup of AVC experiment using PSA is shown in Figure 9.

4.1. AVC Experiment under Harmonic Excitation. The external excitation is selected near the natural frequency of the second-order bending mode of the cantilever beam, which is 30 Hz, and the control channel model is obtained by offline identification process described in Section 3.2. After the

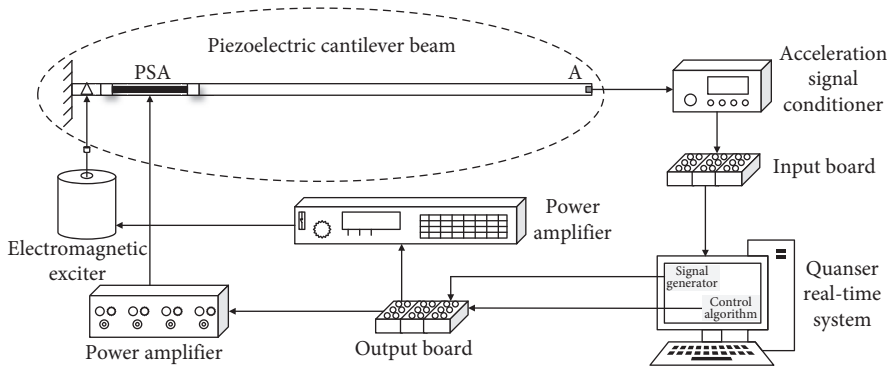

Figure 8: AVC experimental diagram of the piezoelectric cantilever beam.

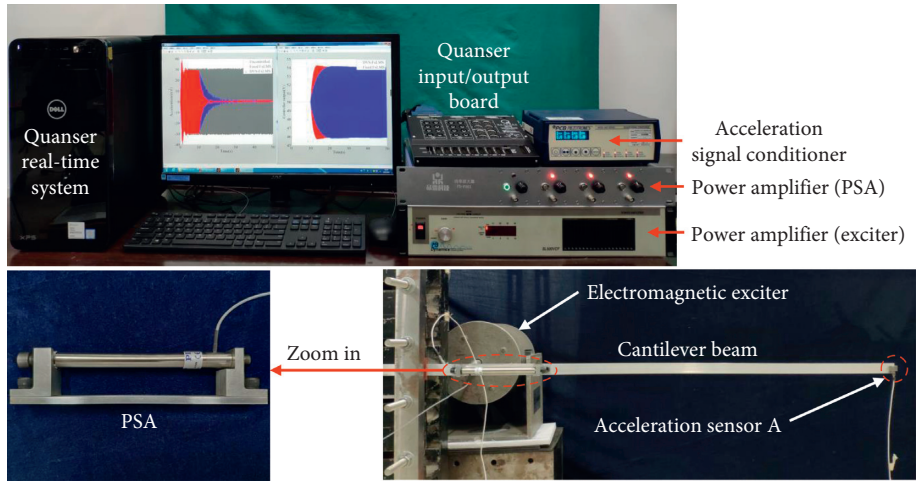

Figure 9: The setup of AVC experiment using PSA.

vibration response of the cantilever beam reaches steady state, the controller is turned on at 10 s, and the experiment lasts for 50 s. Among them, the adaptive filter order of the traditional fixed step FxLMS controller is set to 32, and the step size in the adaptive algorithm is adjusted to $2E-6$. Meanwhile, the adaptive filter order of the DVSFxLMS controller is set to 32, and the step size parameters are adjusted to $\beta = 5E-6$ and $p = 100$. The superiority of the DVSFxLMS control algorithm proposed over the traditional fixed step FxLMS control algorithm is compared and studied.

The experimental results are shown in Figure 10. From Figures 10(a) and 10(c), it can be seen that the convergence time of the fixed step FxLMS controller is 19.5 s. After the structural vibration reaches steady state, the peak acceleration at the tip of the cantilever beam is decreased by 93.7%. At the same time, the convergence time of the DVSFxLMS controller designed is 8.1 s, and the control effect reaches 95.1%, which is better than fixed step FxLMS controller. As shown in Figure 10(b), at the initial period, the output voltage of the DVSFxLMS controller is higher than that of the fixed step FxLMS controller, and then quickly reaches the optimal value to ensure high level of the vibration suppression performance. Figure 10(d) shows the iterative curves of the adaptive filter weight coefficients of the DVSFxLMS controller, and the filter weight coefficients converge quickly and smoothly. In summary, compared with the fixed step FxLMS control algorithm, the DVSFxLMS control algorithm proposed has the characteristics of fast convergence rate and good steady-state vibration suppression performance, which effectively solve the constraints of the convergence rate, steady-state error and step size of the fixed step FxLMS control algorithm.

4.2. AVC Experiment under Harmonic Excitation with Superimposed Noise. In order to verify the ability of the DVSFxLMS control algorithm proposed to resist noise interference, this section conducts experimental research on AVC under the harmonic excitation with superimposed noise.

Excitation signal consists of 30 Hz sine signal superimposed 28–32 Hz zero-mean Gaussian white noise, and the variance of the superimposed noise σ^2 is set to 1, 0.25, and 0.01, respectively. The controller parameter settings are the same as described in Section 4.1. Turn on the controller at 10 s, and the experiment lasts for 50 s. The experimental results of AVC under the harmonic excitation with superimposed noise are shown in Figures 11 and 12.

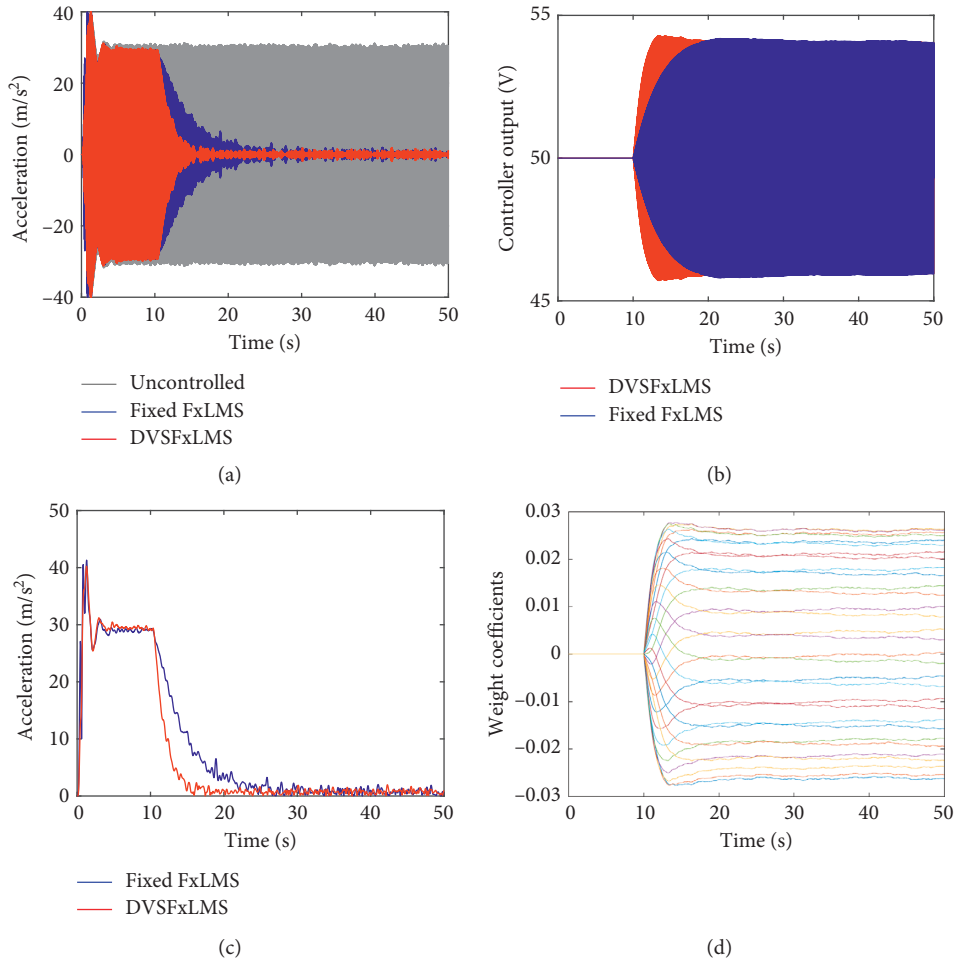

Figure 10: Comparison of experimental results of the DVSFxLMS controller: (a) acceleration response at point A; (b) output voltage; (c) peak acceleration response at point A; (d) adaptive filter weight coefficient iteration curves of the DVSFxLMS controller.

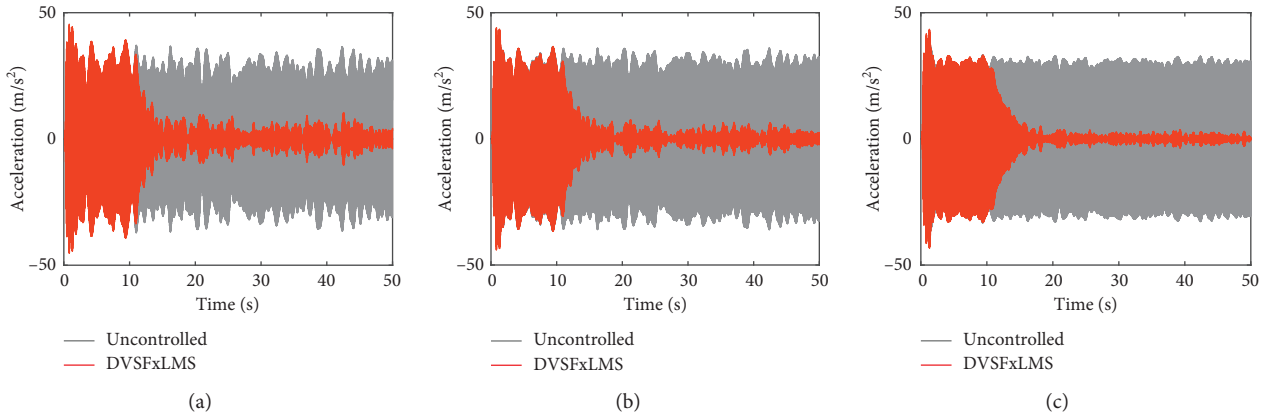

Figure 11: Experimental results of the DVSFxLMS controller under harmonic excitation with superimposed noise: acceleration response at point A. (a) $\sigma^2 = 1$, (b) $\sigma^2 = 0.25$, and (c) $\sigma^2 = 0.01$.

It can be seen from Figure 11 that under the harmonic excitation with superimposed noise, the DVSFxLMS controller can all converge to steady state in about 8 s. During the steady state, the DVSFxLMS controller can also adaptively adjust the filter parameters according to the changes of the error signal to suppress vibration response of the controlled structure, which shows the ability to resist noise interference.

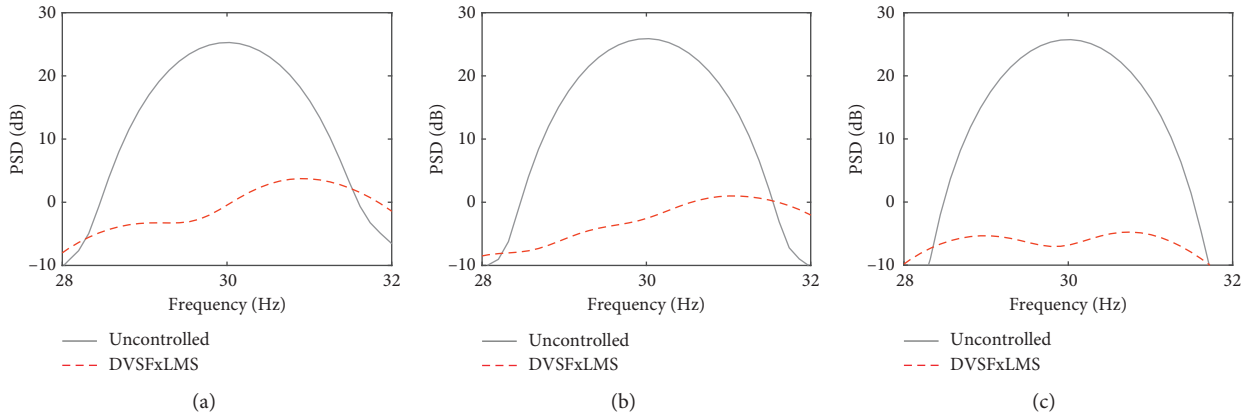

Figure 12: Acceleration response PSD contrast at point A (open/closed loop). (a) $\sigma^2 = 1$, (b) $\sigma^2 = 0.25$, and (c) $\sigma^2 = 0.01$.

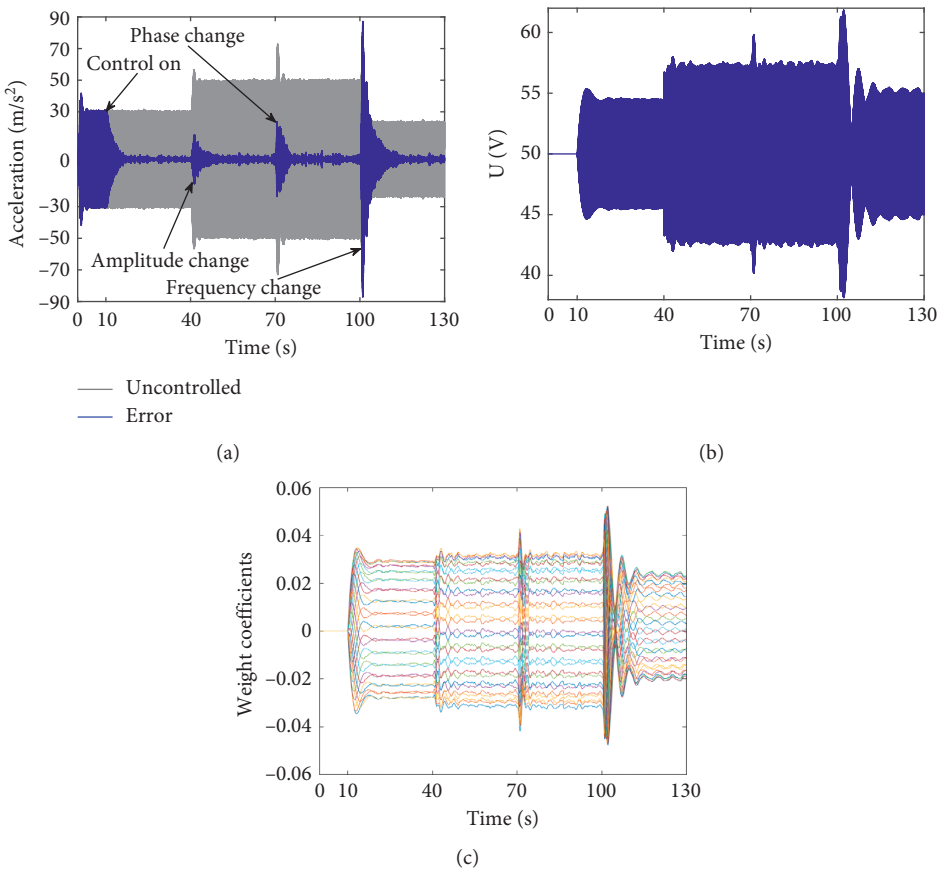

Figure 13: Adaptive control experimental results of the DVSFxLMS controller: (a) acceleration response at point A; (b) output voltage; (c) adaptive filter weight coefficient iteration curves.

The acceleration response PSD (power spectral density) contrast at point A in the open/closed loop state of the control system is shown in Figure 12. Under the harmonic excitation of superimposed noise signals with variances of 1, 0.25, and 0.01, the DVSFxLMS controller can effectively reduce vibration level of the controlled structure. The lower the variance of the superimposed noise, the better effect of the active structural vibration control. Finally, the peak value of the PSD spectrum is decreased by 21.5 dB, 24.9 dB, and 30.5 dB, and the RMS (root mean square) of the acceleration response is decreased by 89.5%, 92.2%, and 95.5%, respectively, which verifies that the proposed DVSFxLMS control algorithm has strong antinoise ability.

4.3. AVC Experiment under Variable External Excitation. In order to investigate the adaptability of the DVSFxLMS control algorithm to variable external disturbance, this

section conducts an adaptive control experiment on the changes of the excitation signal amplitude, phase, and frequency. The control system starts to use 30 Hz sine signal as the excitation, and the controller is turned on at 10 s. After vibration response of the structure is attenuated and stabilized, the excitation signal amplitude increases to 1.5 times of the original amplitude at 40 s, the phase of excitation signal changes $\pi/4$ at 70 s, and the frequency of excitation signal increases by 5% at 100 s; that is, it becomes 31.5 Hz. The experiment time lasts for 150 s, and the controller parameters are consistent with Section 4.1.

Figure 13(a) shows the acceleration response at point A, and Figure 13(b) shows the output voltage of the DVSFxLMS controller. It can be seen that after the controller is turned on, the structural vibration response quickly decays to steady state. When the excitation signal amplitude, phase, or frequency changes, the structural vibration response rapidly increases. Then, the DVSFxLMS controller adjusts the output voltage according to the changes of the structural vibration response, and drives the PSA to generate actuating bending moment, so that the structural vibration response quickly decays to steady state again. The adjustment process takes 9.3 s, 5.1 s, and 13.4 s, respectively, which realizes the adaptive control of the structural vibration response when the external excitation changes. It can be seen from Figure 13(c) that when the excitation signal parameters change, the DVSFxLMS controller can quickly adjusts the weight coefficients of the adaptive filter according to the DVSFxLMS algorithm to reach steady state, which ensures good vibration suppression performance. The experimental results of adaptive vibration control show that the DVSFxLMS control algorithm proposed has fast tracking rate and strong adaptive control ability to variable external disturbance.

5. Conclusion

In the present study, a new variable step size FxLMS algorithm (DVSFxLMS algorithm) is proposed by establishing nonlinear function between the step size μ and the error signal, while using the difference term of error signal $\Delta e(n) = |e(n) - e(n-1)|$ into the original algorithm as a feedback control function. At the same time, the correlation value of the error signal $|e(n)e(n-1)|$ is used instead of the square of the error signal $|e(n)|^2$ to adjust step size. Subsequently, DVSFxLMS controller is designed, and PSA is used to conduct AVC simulation and experiments on a cantilever beam. Results show that the proposed DVSFxLMS control algorithm can effectively suppress the vibration response of the cantilever beam. The control effect of single frequency harmonic excitation is 95.1%, and the convergence time is 8.1 s, while that of the fixed step FxLMS controller is 19.5 s. Compared with the traditional fixed step FxLMS control algorithm, the convergence rate is faster, and the steady-state vibration suppression performance is better. The DVSFxLMS controller can still achieve good control effects under the harmonic excitation with superimposed noise. The vibration response of the cantilever beam converges to steady state in about 8 s. Under the harmonic excitation of superimposed noise signals with variances of 1, 0.25, and 0.01, the peak value of the PSD spectrum of the acceleration response at observation point is decreased by 21.5 dB, 24.9 dB, and 30.5 dB, and the RMS is reduced by 89.5%, 92.2%, and 95.5%, respectively, which shows that the DVSFxLMS control algorithm has strong antinoise ability. When the amplitude, phase, or frequency of the excitation signal changes, the DVSFxLMS controller can adjust the control voltage accordingly, quickly suppress the structural vibration response in about 8 s, and achieve good control effect, which indicates that the proposed DVSFxLMS control algorithm has strong adaptive control ability to quickly track the variable external disturbance.

A new DVSFxLMS control algorithm is proposed in this paper, and the DVSFxLMS controller is designed to effectively suppress the vibration response of the piezoelectric cantilever beam. Considering that the physical characteristics and system characteristics of the controlled structure used in this paper are relatively stable, and therefore, a reliable identification result is obtained by using the offline identification strategy of control channel based on the LMS algorithm. In order to further improve the practicability and applicability of the algorithm proposed, and make it also suitable for time-varying structures, an adaptive controller with online identification function of control channel can be studied based on the variable step size LMS algorithm [3, 29]. In addition, when faced with large and complex controlled structures, the single-channel controller has certain limitations. The multichannel FxLMS controller can be designed based on the variable step size LMS algorithm [30, 31], while considering the control channel coupling phenomenon to further optimize the structure of variable step size FxLMS controller to be applied to actual engineering structures.

Data Availability

The MATLAB .mat data used to support the findings of this study are available from the corresponding author upon request.

Conflicts of Interest

The authors declare that they have no conflicts of interest.

Acknowledgments

This work was supported by the National Natural Science Foundation of China (grant no. 11502208).

References

[1] P. S. R. Diniz, "Fundamentals of adaptive filtering," *Springer International*, vol. 694, pp. 13–78, 2013.

[2] S. Elliott, I. Stothers, and P. Nelson, "A multiple error LMS algorithm and its application to the active control of sound and vibration," *Institute of Electrical and Electronics Engineers Transactions on Acoustics, Speech, and Signal Processing*, vol. 35, no. 10, pp. 1423–1434, 1987.

[3] W. Niu, C. Zou, B. Li, and W. Wang, "Adaptive vibration suppression of time-varying structures with enhanced FxLMS

algorithm," *Mechanical Systems and Signal Processing*, vol. 118, pp. 93–107, 2019.

[4] L. H. Yang, S. Y. Liu, H. P. Zhang et al., "Hybrid filtered-x adaptive vibration control with internal feedback and online identification," *Shock and Vibration*, vol. 2018, Article ID 9010567, 15 pages, 2018.

[5] J. C. O. Marra, E. M. O. Lopes, J. J. d. Espíndola, and W. A. Gontijo, "Hybrid vibration control under broadband excitation and variable temperature using viscoelastic neutralizer and adaptive feedforward approach," *Shock and Vibration*, vol. 2016, Article ID 5375309, 12 pages, 2016.

[6] T. Aboulnasr and K. Mayyas, "A robust variable step-size LMS-type algorithm: analysis and simulations," *Institute of Electrical and Electronics Engineers Transactions on Signal Processing*, vol. 45, no. 3, pp. 631–639, 1997.

[7] B. Huang, Y. Xiao, J. Sun, and G. Wei, "A variable step-size FXLMS algorithm for narrowband active noise control," *Institute of Electrical and Electronics Engineers Transactions on Audio, Speech, and Language Processing*, vol. 21, no. 2, pp. 301–312, 2013.

[8] D. Bismor, K. Czyz, and Z. Ogonowski, "Review and comparison of variable step-size LMS algorithms," *The International Journal of Acoustics and Vibration*, vol. 21, pp. 24–39, 2016.

[9] B. Jalal, X. Yang, Q. Liu, T. Long, and T. K. Sarkar, "Fast and robust variable-step-size LMS algorithm for adaptive beamforming," *Institute of Electrical and Electronics Engineers Antennas and Wireless Propagation Letters*, vol. 19, no. 7, pp. 1206–1210, 2020.

[10] R.D Gitlin and S.D Weinstein, "On the design of gradient algorithms for digitally implemented adaptive filters," *Institute of Electrical and Electronics Engineers Transactions on Circuit Theory*, vol. 20, no. 2, pp. 125–136, 1973.

[11] J. Qin and J. Ouyang, "A new variable step size LMS adaptive filtering algorithm," *Journal of Data Acquisition and Processing*, vol. 12, no. 3, pp. 171–194, 1997.

[12] Y. Gao and S. Xie, "A variable step size LMS adaptive filtering algorithm and its analysis," *Journal of Electronics*, vol. 28, no. 8, pp. 1094–1097, 2001.

[13] G. Han, F. Wang, H. Zhao et al., "A variable step size LMS adaptive filtering algorithm and its application," *Journal of North University of China*, vol. 38, p. 2, 2017.

[14] W. Ao, W. Q. Xiang, Y. P. Zhang et al., "A new variable step size LMS adaptive filtering algorithm," in *Proceedings of the International Conference on Computer Science and Electronics Engineering*, pp. 265–268, Institute of Electrical and Electronics Engineers, Kuala Lumpur, Malaysia, April 2012.

[15] Y. Li and X. N. Wang, "A modified VSLMS algorithm," in *Proceedings of the International Conference on Advance Communication Technology*, pp. 615–618, Institute of Electrical and Electronics Engineers, Bangalour, India, January 2011.

[16] K. Xu, J. Hong, and G. Yue, "A modified LMS algorithm for variable step size adaptive filters," *Journal of Circuits and Systems*, vol. 9, no. 4, pp. 115–117, 2004.

[17] G. Wang, H. Zhao, and P. Song, "Robust variable step-size reweighted zero-attracting least mean m-estimate algorithm for sparse system identification," *Institute of Electrical and Electronics Engineers Transactions on Circuits and Systems II: Express Briefs*, vol. 67, no. 6, pp. 1149–1153, 2019.

[18] J. Mohammad, S. Mohammad, H. Aykut, and O. Kukrer, "A zero-attracting variable step-size LMS algorithm for sparse system identification," *Signal, Image and Video Processing*, vol. 9, 2013.

[19] P. Song and H. Zhao, "Filtered-x least mean square/fourth (FXLMS/F) algorithm for active noise control," *Mechanical Systems and Signal Processing*, vol. 120, pp. 69–82, 2019.

[20] H. Guo, Y. S. Wang, N. N. Liu, R. P. Yu, H. Chen, and X. T. Liu, "Active interior noise control for rail vehicle using a variable step-size median-LMS algorithm," *Mechanical Systems and Signal Processing*, vol. 109, pp. 15–26, 2018.

[21] Y. Fang, X. Zhu, Z. Gao, J. Hu, and J. Wu, "New feedforward filtered-x least mean square algorithm with variable step size for active vibration control," *Journal of Low Frequency Noise, Vibration and Active Control*, vol. 38, no. 1, pp. 187–198, 2019.

[22] X. Zhu, Y. Fang, J. Hu, Z. Gao, and Z. Miao, "Analysis and validation of the active vibration control of flexible piezoelectric beam with fx-VSSLMS algorithms," *Journal of Vibration, Measurement and Diagnosis*, vol. 40, no. 2, pp. 215–221, 2020.

[23] Y. Fang, X. Zhu, J. Hu, Z. Gao, and Z. Miao, "A VSSFxLMS algorithm and its application in multiple DOF micro-vibration control," *Journal of Vibration Engineering*, vol. 33, no. 3, 2020.

[24] B. Widrow and M. E. Hoff, "Adaptive switching circuits," *IRE Wescon Convention Record*, vol. 4, pp. 96–104, 1960.

[25] J. Nagumo and A. Noda, "A learning method for system identification," *IEEE Transactions on Automatic Control*, vol. 12, no. 3, pp. 282–287, 1967.

[26] J. Yi and S. Huaizong, "A new variable step size LMS adaptive filtering algorithm and its simulation," *Signal Processing*, vol. 26, no. 9, pp. 1385–1388, 2010.

[27] D. Meng, P. Xia, and L. Song, "MIMOMH feed-forward adaptive vibration control of helicopter fuselage by using piezoelectric stack actuators," *Journal of Vibration and Control*, vol. 24, no. 23, pp. 5534–5545, 2018.

[28] P-840 Preloaded Piezo Actuators, https://www.physikinstrumente.com/en/products/linear-actuators/nanopositioning-piezo-actuators/p-840-preloaded-piezo-actuators-101000/#specification.

[29] Q. Huang, Z. Gao, S. Gao, Y. Shao, and X. Zhu, "Research of active vibration control algorithm based on online control channel identification," in *Proceedings of the Third International Conference on Measuring Technology and Mechatronics Automation*, Shanghai, China, January 2011.

[30] Y. Shao, Z. Gao, S. Gao, J. Yi, and X. Zhu, "FXLMS algorithm based multi channel active vibration control of piezoelectric flexible beam," in *Proceedings of the 8th World Congress on Intelligent Control And Automation*, Jinan, China, July 2010.

[31] J.-H. Shin, W.-J. Jung, S.-R. Bae, S.-K. Lee, and M. K. Kwak, "Multi-input multi-output fxLMS algorithm for active vibration control of structures subjected to non-resonant excitation," *Transactions of the Korean Society for Noise and Vibration Engineering*, vol. 28, no. 3, pp. 330–338, 2018.

Hindawi
Shock and Vibration
Volume 2020, Article ID 8843759, 20 pages
https://doi.org/10.1155/2020/8843759

Review Article

A Review of Artificial Intelligence Methods for Condition Monitoring and Fault Diagnosis of Rolling Element Bearings for Induction Motor

Omar AlShorman,[1] **Muhammad Irfan**,[2] **Nordin Saad**,[3] **D. Zhen**,[4] **Noman Haider**,[5] **Adam Glowacz**,[6] **and Ahmad AlShorman**[7]

[1]*Faculty of Engineering and AlShrouk Trading Company, Najran University, Najran, Saudi Arabia*
[2]*College of Engineering, Electrical Engineering Department, Najran University, Najran, Saudi Arabia*
[3]*Department of Electrical and Electronics Engineering, Universiti Teknologi PETRONAS, 32610 Seri Iskandar, Perak, Malaysia*
[4]*Hebei University of Technology, Tianjin, China*
[5]*College of Engineering and Science, Victoria University, Sydney, Australia*
[6]*Department of Automatic Control and Robotics, AGH University of Science and Technology, 30-059 Kraków, Poland*
[7]*Mechanical Engineering Department, Jordan University of Science and Technology, Irbid, Jordan*

Correspondence should be addressed to Omar AlShorman; omar2007_ahu@yahoo.com

Received 27 July 2020; Revised 13 October 2020; Accepted 22 October 2020; Published 4 November 2020

Academic Editor: Yongfang Zhang

The fault detection and diagnosis (FDD) along with condition monitoring (CM) and of rotating machinery (RM) have critical importance for early diagnosis to prevent severe damage of infrastructure in industrial environments. Importantly, valuable industrial equipment needs continuous monitoring to enhance the safety, reliability, and availability and to decrease the cost of maintenance of modern industrial systems and applications. However, induction motor (IM) has been extensively used in several industrial processes because it is cheap, reliable, and robust. Rolling bearings are considered to be the main component of IM. Undoubtedly, any failure of this basic component can lead to a serious breakdown of IM and for whole industrial system. Thus, many current methods based on different techniques are employed as a fault prognosis and diagnosis of rolling elements bearing of IM. Moreover, these techniques include signal/image processing, intelligent diagnostics, data fusion, data mining, and expert systems for time and frequency as well as time-frequency domains. Artificial intelligence (AI) techniques have proven their significance in every field of digital technology. Industrial machines, automation, and processes are the net frontiers of AI adaptation. There are quite developed literatures that have been approaching the issues using signals and data processing techniques. However, the key contribution of this work is to present an extensive review of CM and FDD of the IM, especially for rolling elements bearings, based on artificial intelligent (AI) methods. This study highlights the advantages and performance limitations of each method. Finally, challenges and future trends are also highlighted.

1. Introduction

Many industries have adopted several measures in their drive to optimize the reliability, availability, and safety to reduce the maintenance cost of modern industrial systems and applications, which are vital to process [1, 2]. Thus, condition-based maintenance (CBM) has gained a significant role in an industrial world [3, 4]. However, CBM is applied in order to achieve early maintenance decisions through CM collected data [5]. Moreover, condition monitoring (CM) and fault detection and diagnosis (FDD) of rotating machinery (RM) [6, 7] have recently gained huge attention [8, 9]. Therefore, CM and FDD become the most important and critical aspects of industrial life (i.e., system design and maintenance) [10]. The main aim of CM and FDD is to follow up the machinery health and the remaining

useful life (RUL) in modern industrial machinery [11, 12]. However, predictive health monitoring (PHM) methods are important to guarantee the required health state of the machinery [13, 14]. Thus, CM and FDD help to ensure the health state of the machinery [15, 16]. Figure 1 shows the main components of a typical CBM [17]. CM methods are categorized into two groups, invasive and noninvasive methods. On the one hand, invasive CM is considered to be simple and basic technique. On the other hand, it is hard to implement. To overcome this challenge, noninvasive CM methods are highly used nowadays [18].

As key components of industrial systems and applications [19–21], rotating machinery, such as motor, gearbox, wind turbines, generator, and engine, is vital equipment in modern industrial applications [22]. These important machines have to run efficiently, accurately, and safely [23]. Due to the criticality and importance of this issue, several analysis and studies were published during the past years where many different approaches have been investigated to improve the CM and FDD for rotating machinery [24, 25]. Conventionally, the traditional CM and FDD methods (such as model and signal as well as data-based methods) [26–29] need to extract the diagnosable information manually from the raw data [30]. Following that, pattern recognition models were developed using the features vector in the classification process [31]. This scenario requires much experience knowledge and complex feature extraction methods [32, 33]. To address this issue, artificial intelligent (AI) methods and techniques for CM and FDD of RM [34–39] are widely employed and applied nowadays [40, 41].

Induction motor (IM) [42–49] is vital in industrial processes and applications [50, 51]. Moreover, IM is extensively used, for example, in mining machines, automotive applications, pumps, blowers, fans, chemical machines, lifts, compressors, vacuums, conveyors cranes, and engines [52–59]. Figure 2 summarizes applications of the IM.

All parts of IM (stator, bearing, bar, and rotor) are affected by stress, aging, vibration, long operating time, continuously monitoring, and electrodynamic forces [60–62]. Thus, any failure of any part of IM may cause a serious breakdown of the machine, which increases the maintenance cost and leads to heavy losses [63, 64]. Figure 3 shows IM faults and their percentage.

Rolling bearings [66] were considered to be the main component of rotating machinery [67]. However, bearings are used in several mechanical and electrical applications, including IM, turbines, medical devices, cars and trucks, engines, automobile industry, and aerospace [68]. Importantly, any failure of this basic component can lead to a serious breakdown of rotating machines [69]. Rolling bearing faults could be categorized by two main factors, location of the fault and nature of the fault. For location category, five main faults occurred including, imbalance shaft faults, ball faults, inner race faults, outer race faults, and cage faults. For nature category, two main faults are considered, including cyclic faults and noncyclic faults [70, 71].

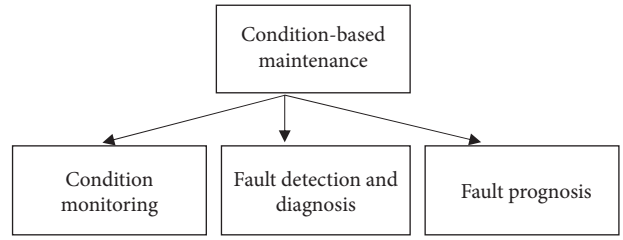

Figure 1: The main components of CBM.

CM and FDD of bearing element bearings of RM are widely used to follow up the operation condition of the machine [72–74]. However, the main task of CM and FDD is to diagnose faults and failures [75, 76]. As a result, any failure may cause a serious breakdown, which increases the maintenance cost and leads to heavy losses [77]. Recently, various methodologies of CM and FDD of IM have been discussed. Moreover, several data and model-based techniques have been introduced including signal processing-based techniques [78, 79], image processing based techniques [80–83], intelligent techniques [84, 85], data fusion techniques [86–90], data mining techniques [91–96], and expert system techniques [97–99]. All those techniques have used specific analyses to develop the FDD methodology to arrive at efficient and accurate results [100, 101]. As shown in Figure 4, the analyses used in those studies include chemical analysis, electrical analysis, and mechanical analysis, in more details, temperature analysis [102–107], vibration analysis [108–112], noise analysis [113, 114], radio-frequency (RF) analysis [115–118], infrared analysis [119–124], current and voltage analysis [125, 126], electromagnetic field analysis [127–129], oil analysis [110, 130–132], pressure analysis [133–137], ultrasound analysis [138–140], and sound and acoustic emission analysis [141, 142]. Figure 5 shows a general block diagram of a noninvasive FDD for rotating machinery. As an example, preprocessing stage includes data denoising and filtering. However, most electrical and mechanical signals are nonlinear and nonstationary signals. Thus, denoising techniques have been extensively studied nowadays. However, wavelet transform (WT), continuous wavelet transform (CWT), discrete wavelet transform (DWT), Kalman filtering, Wiener filtering, Empirical mode decomposition (EMD), variational mode decomposition (VMD), and singular value decomposition (SVD) are some common denoising techniques [143]. Table 1 shows a comparison between various CM analysis techniques.

The main objective of this work is to review the CM and FDD of the IM, especially for rolling elements bearings, based on artificial intelligent (AI) methods. The study also points out the advantages and drawbacks of each method. Finally, research challenges and possible future trends directions in this field are also presented in this article.

The rest of the paper has been organized as follows. Firstly, background and general introduction are discussed in Section 2. Secondly, AI for CM and FDD for

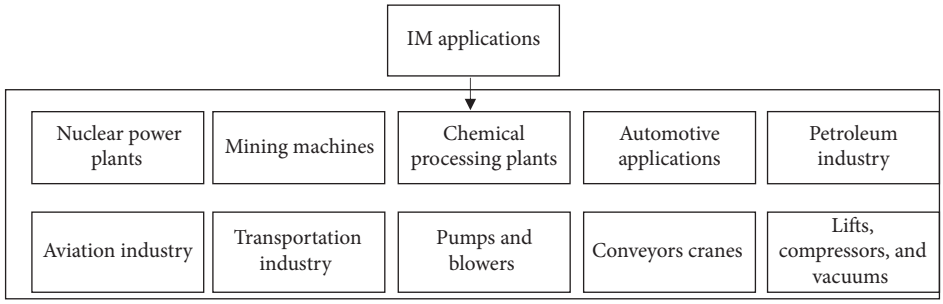

Figure 2: Applications of the IM.

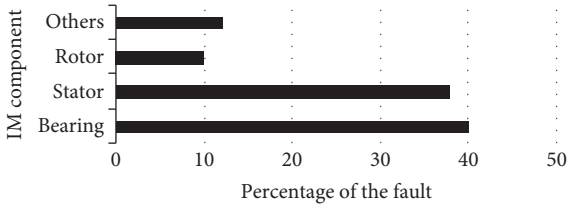

Figure 3: IM faults [65].

rolling bearings are presented in Section 3. Finally, challenges and future trends are discussed in Section 4.

2. Background and General Introduction

Nowadays, the need for earlier detection of faults for IM is crucial. However, in order to increase the reliability of IM, AI has been used to measure the accuracy at the incipient stage of CM and FDD for IM [144]. Figure 6 shows all most AI methods used in CM and FDD. A variety of AI studies of CM and FDD for IM have been recently reported. In [145], an intelligent FDD of RM (i.e., automotive engine) framework is introduced. Therefore, in the feature extraction stage, ensemble empirical mode decomposition (EEMD) is implemented followed by intrinsic mode functions (IMF) decomposition. The correlation coefficient (CC) along with singular value decomposition (SVD) is employed to eliminate the redundant IMF and to obtain fault features. To add a new layer of improvement, five single classifiers based on the probabilistic committee machine (PCM) and Bayesian learning machine are trained and used in the classification stage.

Furthermore, (1) the single probabilistic classifiers, (2) the single probabilistic and Bayesian machines, (3) pairwise-coupled, and (4) two classifiers without pairwise-coupling strategy are used for further comparison of classification. As a result, the proposed probabilistic committee machine method showed the superiority of diagnosing faults. In [146], an online feature condition monitoring approach based on unsupervised feature learning (dictionary learning) under different operational conditions using vibration and acoustic emission signals is introduced. This work also presents dictionary distance and signal fidelity driven methods and techniques for anomaly detection are also described. Moreover, time-propagated characteristics are used along with sparse approximation of signals received from vibration and acoustic emissions. Importantly, the results of three case studies, i.e., the approximation accuracy, overall computational overhead, and the adaptation rate, are presented. As a result, under normal variation condition, the learned features change slowly in comparison with high-speed variation when a fault appears. In [147], an FDD system of IM designed on multiscale entropy and support vector machine (SVM) in combination with mutual information algorithm is proposed. The aim is to retrieve the required entropy feature; techniques like vibration signals, sample entropy, and multiscale entropy are applied. Importantly, a support vector machine classifier is used for the entropy feature vector. Furthermore, classification results showed that these SVM based entropy techniques could effectively diagnose various motor faults (i.e., bearing faults, stator faults, and rotor faults). In [148], a multiclass FDD approach of IM using wavelet and Hilbert transforms is introduced. Moreover, for a feature extraction stage, Hilbert transform (HT) and continuous wavelet transform (CWT) are applied as advance signal processing techniques to retrieve features and characteristics from radial vibration signals and to detect rotor, bearing, and stator faults. Importantly, three classifiers are employed in this research: the neural network (multilayer perceptron), neural network (radial basis function), and support vector machines. As a result, in this study, the performance of SVM is found to be the best compared with NN classifiers, i.e., MLP and RBF classifiers. In [149], a compound FDD approach for IM at variable operating conditions using the SVM classifier is introduced. Moreover, radial vibration and stator currents are used. Four motor conditions are extracted and classified, including healthy induction motor, misalignment, unbalanced rotor, and bearing fault. Kernel-nonlinear SVM along with Gaussian radial basis function is employed. As a result, SVM bootstrap based technique with features data fusion has an ability of classifying multiple and single faults for different operating conditions of the IM with good accuracy (84.8–100%). In [150], vibration and current monitoring based approach for both electrical and mechanical faults' prediction under various operating conditions for IM is proposed. Moreover, nine mechanical and electrical faults are detected and classified using a multiclass SVM algorithm. In the feature extraction stage, time domain of vibration and current signals is used to seek statistical features. Importantly, MSVM is trained using the radial basis function (RBF) kernel. As a result, for the vibration signal and

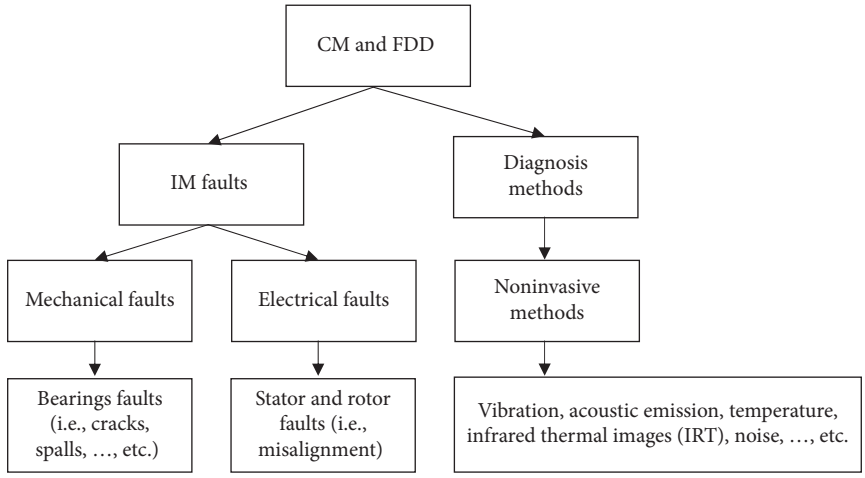

Figure 4: CM and FDD techniques of IM.

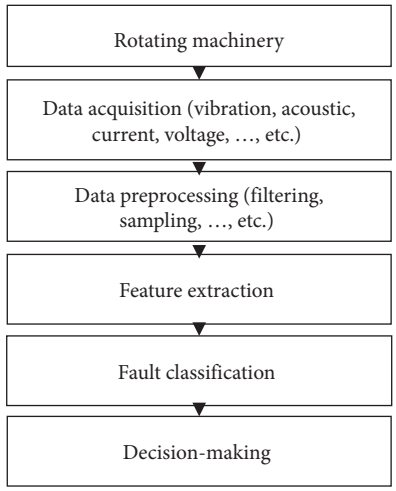

Figure 5: General block diagram of FDD using machine learning.

mechanical faults, the MSVM showed an ability of predicting all faults, but it could not predict current signals based on electrical faults. However, the SVM is better than MSVM for electrical faults diagnosis.

Recently, deep learning [151–153] is extensively used in CM and FDD for IM. In [154], an automatic FDD approach of IM uses deep learning techniques to combine the feature extraction process with the classification process. Moreover, deep belief networks (DBN) are modelled for vibration signals to retrieve key features. Moreover, the restricted Boltzmann machine (RBM) is used to build and train the DBN using a layer-by-layer pretraining algorithm. Importantly, the proposed approach could detect the fault directly from frequency distribution without needing traditional feature extraction methods. Furthermore, to elevate the classification accuracy and reduce training error, the proposed approach could learn multiple layers of representation and model high-dimensional data. In [155], an unsupervised feature learning sparse autoencoder-based deep neural network approach for induction motor faults classification is proposed. Moreover, the proposed approach detected and classified multiple faults, three-rotor faults (bowed, unbalanced, and rotor bars), defective bearing, and stator winding fault. Features obtained from a sparse autoencoder are used to train a neural network classifier. Importantly, the method called "dropout" is used to prevent the training process from overfitting. As a result, SAE-based DNN approach showed good results in terms of feature learning capability and classification accuracy of FDD for IM. To avoid complex sensor data problems, deep learning technique is recently used. In [156], deep learning for infrared thermal (IRT) images is introduced to detect various machine conditions. Moreover, convolutional neural networks (NNs) are employed. The accuracy of this method is at least 6.67% better compared with normal approaches. Importantly, it can be used for online FDD and CM when the access is very difficult such as in offshore wind turbines. Table 2 summarizes AI studies of CM and FDD for IM.

The bearing is a critical component in IM. Thus, robust and intelligent CM and FDD methods are highly needed to enhance detection, diagnosis, monitoring, and prognosis capabilities.

3. AI in CM and FDD of Rolling Element Bearings for IM

Bearing faults are considered to be a majority of faults in IM [164–166]. In [167], four classification methods for intelligent CM and FDD of rolling bearings are proposed. Moreover, accuracy, time consumption, intelligibility, and maintaining ability of intelligent methods like SVM based particle swarm optimization (PSO-SVM), *K*-Nearest Neighbor algorithm (KNN), a rule-based method (RBM) based on the MLEM2 algorithm and probabilistic neural network (PNN) are discussed. As a result, PSO-SVM ranked the first in terms of accuracy followed by the RBM, but PSO-SVM and RBM required more programming efforts. Furthermore, the RBM showed the best in terms of interpretation and reduction. In [168], an adaptive method for the health monitoring of rotating bearings using the vibration signal is introduced. The proposed

Table 1: Comparison between various CM analysis techniques for bearings of IM.

The technique	Advantages	Drawbacks	Fault
Temperature and infrared analysis	(i) Basic method (ii) Noninvasive	(i) Expensive sensor is required (ii) It cannot be used as early FDD	(i) Mechanical and electrical faults
Vibration and noise analysis	(i) Reliable and standard method (ii) It can be used as early FDD	(i) Sensitive to the noise (ii) Expensive sensor is required (iii) Intrusive	(i) Mechanical faults
Chemical and oil analysis	(i) Fault estimation and location capabilities (ii) High performance for bearing FDD	(i) Expensive (ii) Applicable for big size machines	(i) Mechanical faults
Sound and acoustic emission analysis	(i) It could be used as reliable and remote CM (ii) It is easily implemented (iii) Fault estimation and location capabilities (iv) Signal to noise ratio is high (v) It deals with high frequency range	(i) Sensitive to the noise (ii) Expensive sensor is required (iii) Intrusive	(i) Mechanical faults
Current, voltage, and electromagnetic field analysis	(i) Inexpensive (ii) Nonintrusive	(i) Sensitive to the noise (ii) It cannot be used as early FDD	(i) Mechanical and electrical faults
Ultrasound analysis	(i) Effective in low speed bearings (ii) It deals with low and middle frequency ranges (iii) High signal to noise ratio	(i) Expensive sensor is required (ii) Intrusive	(i) Mechanical and electrical faults

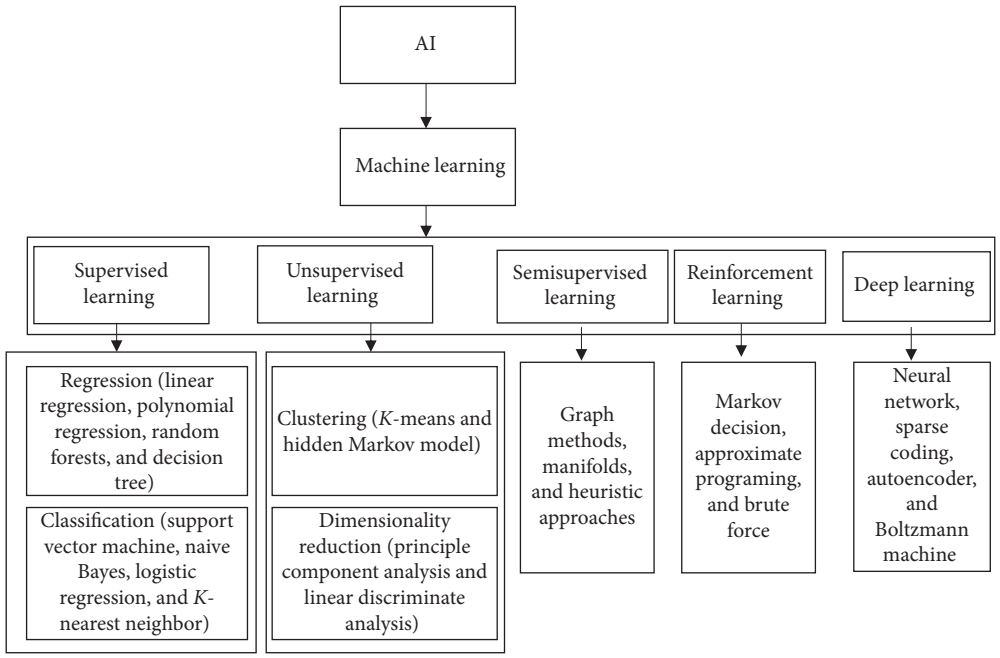

Figure 6: AI methods used in CM and FDD for rotating machinery.

method applies the empirical mode decomposition–self-organizing map (EMD–SOM) to find a confidence value (CV) and to find the degradation of the fault. As a result, SOM based technique showed a high ability for online condition monitoring, especially for limited computing resources cases.

3.1. Bayesian Network. Bayesian network [169, 170] is a probabilistic statistical model, which uses a directed acyclic graph (DAG) to seek conditional dependencies. This model shows a direct representation of causal relations between variables. Currently, the Bayesian network is extensively used [171] in several applications, such as feature extraction

Table 2: AI studies of CM and FDD for IM.

Reference	Analysis type	Feature extraction	Classification	Highlights
[145]	Vibration	Ensemble empirical mode decomposition (EEMD) and correlation coefficient (CC) along with singular value decomposition (SVD)	(1) The single probabilistic classifiers (2) The single probabilistic and Bayesian machines (3) Pairwise-coupled (4) Two classifiers without pairwise-coupling	(i) It diagnoses multiple and single faults (ii) There is simultaneous fault diagnosis (iii) The accuracy for a single fault is 92.62% and for simultaneous faults is 85.73%
[146]	Vibration and acoustic emission	Unsupervised feature	Dictionary learning	(i) There is online monitoring (ii) There are different operational conditions (iii) There are good computational costs
[147]	Vibration	Multiscale entropy	SVM	(i) It diagnoses multiple faults (ii) The average accuracy is 96.25%
[148]	Vibration	Hilbert transform (HT) and continuous wavelet transform (CWT)	Neural network (multilayer perceptron), neural network (radial basis function), and support vector machines	(i) There is multiclass FDD (ii) SVM is found to be the best (with SVM 99.71%) compared to NN classifiers
[149]	Vibration and current	SVM bootstrap based technique with features data fusion	Kernel-nonlinear SVM along with Gaussian radial basis function	(i) SVM multiclassification scheme is presented (ii) It diagnoses multiple faults (iii) There are different operational conditions (iv) The average accuracy is 99.4%
[150]	Vibration and current	Statistical features analysis	SVM and multiclass SVM	(i) It diagnoses multiple faults (ii) There is electrical and mechanical faults' prediction (iii) There are different operational conditions (iv) MSVM showed an ability of predicting all mechanical faults (v) SVM is better than MSVM for electrical faults diagnosis (vi) The average accuracy is 93.28%
[154]	Vibration	Deep learning	Deep belief networks (DBN)	(i) There is automatic FDD (ii) The proposed approach could detect the fault directly from frequency distribution without needing traditional feature extraction methods (iii) It learns multiple layers of representation and models high-dimensional data (iii) The average accuracy is 99.00%
[155]	Vibration	Deep learning	Sparse autoencoder	(i) It diagnoses multiple faults (ii) It prevents training process overfitting (iii) The average accuracy is 97.61%
[156]	Infrared thermal (IRT) images	Deep learning	Convolutional neural networks	(i) There is online monitoring (ii) There are different operational conditions (iii) The average accuracy is 95%
[157]	Stator current	Deep learning	Deep neural network	(i) IM bearings monitoring tool based on deep learning is proposed (ii) Different load conditions 25%, 50%, 75%, and 100% are tested (iii) Deep neural network showed better classification accuracy than shallow neural network (SNN) and principle component analysis (PCA)

Table 2: Continued.

Reference	Analysis type	Feature extraction	Classification	Highlights
[158]	Vibration	Kurtogram and deep learning	Recurrent NN, long-/short-term memory, and gated recurrent unit	(i) FDD method based on kurtogram and deep learning is proposed (ii) Computational time, computing resources and number of layers, is small (iii) Misclassification occurred (iv) The average accuracy is 98%
[159]	Vibration	Neural networks	Transfer learning	(i) Bearing FDD approach based on transfer learning with neural networks is proposed (ii) Different working conditions are analysed (iii) Training time comparing with NN is reduced (iii) It deals with massive data (iv) Transfer learning improved the classification accuracies (v) The total classification accuracy is improved by 10.4 %
[160]	Acoustic emission	Transfer learning-based convolutional neural network	Transfer learning	(i) Bearing FDD acoustic spectral imaging and transfer learning under variable speed conditions and different rotational speeds is proposed (ii) Two-dimensional acoustic frequency spectral imaging with a transfer learning is discussed (iii) The proposed method achieved an average accuracy of 94.67%
[161]	Vibration	Long-/short-term memory recurrent neural network and feature-transfer learning (joint distribution adaptation)	Grey wolf optimization algorithm	(i) Bearing FDD based on adaptive deep transfer learning is proposed (ii) Massive labeled fault data is collected and analysed (iii) The proposed method achieved an average accuracy of 99.4 %
[162]	Vibration	Multiscale deep intraclass adaptation network	Multiple scale feature learner	(i) Bearing FDD is based on multiscale deep intraclass transfer learning (ii) Different working conditions are analysed (iii) The proposed method achieved an average accuracy of 99 %
[163]	Vibration	Hybrid deep signal processing approach	Autoencoder	(i) Deep learning with time synchronous resampling mechanism is proposed (ii) The proposed method dealt with shift variant properties, periodic inputs, and misclassification challenges (iii) The proposed method achieved an average accuracy of 99 %

and classification machine learning algorithms, data mining and data processing, speech processing, bioinformatics, error-control codes, medical applications, industrial diagnosis, and wireless sensor networks [172–174]. As a ML algorithm for FDD of IM fault, the Bayesian network is applied. In [175], different operating conditions of bearing FDD approach based on acoustic signal are proposed. Decision tree (dimensionality reduction) is applied to extract descriptive statistical features vector in the feature extraction stage. Next, Bayes classifier is used in the classification stage. In [170], the diagnosis approach of bearing faults in rotary machinery based on the nonnative Bayesian approach using vibration signals is introduced. In detail, EMD is utilized to split up vibration signals into IMFs, and then the correlation coefficient is used to pick the appropriate IMFs. Shannon energy entropy of IMFs is used to seek useful statistical properties and features. Finally, a nonnative Bayesian classifier (NNBC) is employed to find independence among features. Furthermore, in order to compare classification results, backpropagation neural networks, normal naive

Bayesian classifiers, and kernel naive Bayesian classifiers are employed. Importantly, in this research study, the NNB classifier showed superiority compared with the other classifiers, including neural network and normal NB.

3.2. Support Vector Machine. The support vector machine (SVM) [176, 177] uses supervised machine learning models along with statistical and predictive methods for classification and regression analysis. SVM is being used to solve big data and multidomain classification problems in the modern industrial environment [178]. SVM is also used as CM and FDD method for IM. Subsequently, in [179], a bearing fault detection scheme using vibration signals of IM is proposed. SVM and continuous wavelet transform (CWT) are used together. As a result, for using SVM with CWT, the proposed scheme is simple to implement, very fast, and high accurate. Using another ANN based techniques requires the cumbersome process of trial and error to obtain an optimal solution. Nevertheless, using a hybrid CWT-SVM technique gives promising results (fast and efficient). In [180], an FDD approach for bearings of IM based on Stockwell transform and SVM is introduced. Moreover, in the feature extraction stage, Stockwell transform technique is used for stator current signals to retrieve features in time and frequency domains. Then, Fisher score ranking is employed to select high-ranking features. Importantly, in the classification and location of faults stages, SVM is used. Following this, comparing the results with another classifier is also applied. Notably, the efficiency achieved using ANN equalled 77.78% whereas the efficiency achieved using SVM classifier equalled 91.667%. In [181], a multi-FDD method for rolling element bearing employing orthogonal supervised linear local tangent space alignment (OSLLTSA) and least square SVM (LS-SVM) is proposed. Furthermore, vibration signals are analysed and crumbled using EMD. In addition, autoregressive (AR) coefficients and instantaneous amplitude Shannon entropy are applied to seek the statistical features for intrinsic mode functions (IMFs). After that, the OSLLTSA technique is applied for dimension minimization to obtain a low-dimensional fault features vector. Importantly, LS-SVM is employed using features vector as an input. Moreover, the LS-SVM components are selected based on enhanced particle swarm optimization (EPSO). As a result, in this study, LS-SVM based OSLLTSA technique gave good results for small sample size problem. In [182], prediction method for machine condition based on wavelet and SVM using vibration signals is proposed. In order to enhance the modeling process, wavelet transform along with SVM is applied. Moreover, SVM-WT degradation-prediction model is employed to reduce irregular characteristics and the complexity of the vibration signal. Importantly, to compare the results, the neural network (NN) approach is also employed. As a result of this research study, WT-SVM model showed the best results compared with the NN and single SVM models. In [183], an FDD approach for rolling element bearings involving the use of enhanced multiscale fuzzy entropy (IMFE), local mean decomposition (LMD), Laplacian score (LS), and improved SVM based binary tree (ISVM-BT) is proposed. Moreover, the local mean decomposition is applied to decompose the complicated vibration signal into a series of product functions (PFs). Particularly, the improved multiscale fuzzy entropy is used to assess the complexity and similarity of the signal. Importantly, the obtained feature is fed to the ISVM-BT classifier. Interestingly, IMFE-ISVM method showed a stable and high performance for analysis of samples of discrete and small time units in series. In [184], a hierarchical fuzzy entropy and binary tree SVM technique for FDD of rolling bearing are introduced. For instance, a hierarchical fuzzy entropy method is applied as a feature retrieval process. To get the fault feature vector by ordering the scale factors, the Laplacian score (LS) method can also be used. Importantly, the obtained feature vector is fed to an improved SVM based binary tree (ISVM-BT) classifier. The proposed ISVM-BT based on hierarchical fuzzy entropy approach showed a good performance for diagnosis of diverse conditions and severities of rolling element bearings.

3.3. Artificial Neural Network (ANN). Recently, artificial neural networks (ANN) [185, 186] have gained great attention in industrial applications [187, 188]. Moreover, NN is used as data processing and classification. Correspondingly, AI self-adaptive FDD system inspired from genetic algorithm (GA) and nearest neighbor (NN) is presented in [189]. Infrared thermography (IRT) is used to diagnose various conditions of roller element bearings. In feature extraction stage to find approximation coefficients, a 2-dimensional discrete wavelet transform (2D-DWT) along with Shannon entropy is used. Moreover, GA and nearest neighbor are applied to find the histograms of chosen coefficients to be fed as an input to the feature space selection method. Cost-effectiveness, noncontact, and nonintrusiveness are the main advantages of applying this method. Multilayer perceptron (MLP) [190] is a multiple layer fee-forward neural network which uses supervised learning. Authors in [125] present an FDD bearing fault identification approach based on ANN for IM. Moreover, in the proposed pattern identification approach, two current sensors are used. Thus, a multilayer perceptron (MLP) with one and two hidden layers is employed. As a result, two hidden layers of MLP are not suitable for bearing fault identification. Two hidden layers MLP showed comparatively low accuracy and indicate higher computational costs compared with one hidden layer MLP.

In [191], an intelligent online approach employing empirical mode decomposition and ANN based technique for automatic FDD of rolling bearings using vibration signals are proposed. Moreover, the feature retrieval method is based on EMD energy entropy. The most significant intrinsic mode functions (IMFs) are selected by applying a mathematical analysis. Then, the picked features are given an input to the ANN to classify bearings defects. Importantly, the proposed EMD-ANN approach could effectively detect the intensity of the bearing defect and assess the bearing performance degradation. Because of this, the proposed approach could be considered as an expert diagnosis and

prognosis system. In [192], a fault discovery for roller bearings and gearboxes neural networks using multiple sensors and convolutional is introduced. The key contribution of this work is to achieve robust diagnosis accuracy by applying data fusion and CNN techniques. Moreover, features are extracted automatically without applying any manual feature extraction/selection processes. As a result, the CNN-data fusion technique showed posing superior diagnosis performance as compared with manual feature extraction techniques.

3.4. Combined ANN and SVM. In order to achieve high diagnostic performance, combined ANN and SVM CM and FDD techniques have been proposed [193]. In more details, according to [194], an FDD approach of rolling element bearings employing statistical feature extraction method using vibration signals is proposed. Here, statistical features are obtained using advanced signal processing tools and central limit theory. Importantly, the output feature vector (statistical feature vector) is fed as an input vector to a classifier which categorizes different types of faults by using ANN and SVM. As a result, in this study, the authors argued that ANN and SVM could not offer an analytical guarantee for the accuracy of FDD classifier. Furthermore, in [195], an FDD method of ball bearings using both ANN and SVM is introduced. Moreover, features of vibration signals are retrieved in time domain using statistical techniques. Following this, ANN and SVM are applied in the classification stage. The key findings of this work are that the accuracy of FDD classifiers based on SVM is comparatively higher than the ANN based classifiers in context of detection and prediction of faults in combined bearing components. In [196], an FDD of ball bearings using the vibration signal is proposed. Correspondingly, multiscale permutation entropy and wavelet based on ANN approach are introduced. Moreover, a multiscale permutation entropy method is applied to seek the best wavelet for a feature selection process. For the classification stage in this approach, two artificial intelligence techniques, ANN and SVM, are employed. As a result of this research study, both ANN and SVM, along with permutation entropy, give identical classification results.

3.5. Neuro-Fuzzy. Neuro-fuzzy is also used as an FDD technique [197]. Yet, in [198], an enhanced real-time FDD scheme for bearing CM based on a neuro-fuzzy (NF) classifier using vibration signals is proposed. Firstly, two signal processing techniques are implemented for the signals from both time and frequency domains, and the time domain includes wavelet-spectrum reference functions and kurtosis ratio reference functions. Secondly, an adaptive NF classifier is developed. Importantly, by considering the future states, the integrated NF based model showed the ability of enhancing diagnostic reliability.

3.6. Deep Neural Network. Recently, deep neural networks [199–203] are highly used in CM and FDD of rotating machinery. Consequently, in [204], a hierarchical diagnosis network (HDN) approach which uses deep learning (DL) technique for FDD of rolling element bearings and uses vibration signals is proposed. Furthermore, HDN is used to obtain deep belief networks (DBN) for the hierarchical layer discovery of the proposed method. Importantly, a two-layer HDN is employed as a two-level diagnosis using the wavelet packet energy feature. The faults are diagnosed at the first layer, while the intensity or severity of the faults is measured at the second layer of HDN. As a comparison process, backpropagation neuron networks (BPNNs) and SVM are both applied to validate the effectiveness of applying HDN-based technique. As a result, HDN shows a very promising result for fault location classification and fault severity identification. In [205], an improved deep fusion method is developed for FDD of IM using vibration data. Moreover, in order to improve and enhance the training of machine learning, a deep autoencoder is built with both contractive autoencoder (CAE) and denoising autoencoder (DAE). Then, locality-preserving projection (LPP) is employed to obtain the deep features vector and to enhance learning capabilities by adding a new layer of learning enhancements. Furthermore, for the training of smart fault detection and diagnosis, the deep fusion features are fed to the neural network-based classifier (softmax). Importantly, as a result of this approach, the proposed method showed more effectiveness and robustness compared with standard CNN. In [206], an innovative DL approach based on deep autoencoder feature learning is introduced as an FDD of rotating machinery using vibration signals. In this study, feature learning is enhanced using the loss function of deep autoencoder based on the maximum correntropy. After that, the artificial fish swarm algorithm is utilized to get the best optimization values of the deep autoencoder signal features. As a result, the authors summarized their conclusions by stating that the proposed method shows effectiveness and robustness compared with other learning methods. In [207], an FDD health state identification approach of rotating machinery components by means of a stacked denoising autoencoder (SDA) using vibration signals is proposed. Furthermore, SDA model is made of training and testing groups. Next, the transmitting rule of greedy training is used to build a deep hierarchical structure via layer-by-layer scenario. In order to obtain a better robustness and high-order characteristics, sparsity representation along with data destruction is employed. As a result, the SDA-based health state identification approach showed promising results, especially for signals with ambient noise and working condition fluctuations. Authors in [208] proposed a deep learning FDD approach using acoustic emission for rolling element bearing which is introduced. Moreover, a short-time Fourier transform (STFT) is used as a preprocessing stage. Then, a simple spectrum matrix is used for optimizing DL networks, large memory storage retrieval (LAMSTAR) neural network specifically. Key advantages of this approach are that it deals with different working conditions, solving the big data and manual feature extraction problems. In [209], a hierarchical adaptive deep convolution neural network approach evolving from an enhanced algorithm for

bearing FDD and severity determination using vibration signals is proposed. Moreover, hierarchical learning rate-adaptive deep CNN (ADCNN) is applied to deal with big data and to use as a feature extraction method for diagnosable information from several mass samples. In addition, a two-layer ADCNN is developed; fault patterns are diagnosed from first layer, while second layer evaluates the fault size. The proposed automatic feature extraction model showed very accurate results compared with the benchmark methods used for fault diagnosis, such as traditional DCNNs. In [210], a deep-learning-based hybrid feature model for bearing FDD approach using vibration signals is proposed. Moreover, the proposed approach can deal with several working conditions, multiple faults, and fault severity. In order to achieve an effective and accurate diagnosis, multiple severities faults, a hybrid technique includes sparse stacked autoencoder (SAE) and deep neural networks (DNNs) are applied. The main advantage of applying this hybrid technique is the ability of extracting more diagnosable vibration information with multiple crack sizes. As a result, the proposed approach showed that it can produce better results in diagnosing bearing multiple severities defects than SVM and backpropagation neural networks (BPNNs). In [211], an FDD approach for gearbox and bearing systems based on deep statistical feature learning using vibration signal analysis is introduced. Furthermore, time domain analysis and frequency domain analysis as well as time-frequency domain analysis are applied to obtain features vector from vibration signals. As a deep statistical feature learning tool, Gaussian-Bernoulli and Boltzmann machines (GRBMs) methods are used to build a Gaussian-Bernoulli deep Boltzmann machine (GDBM). The proposed approach showed good classification performances (95.17% for the gearbox and 91.75% for the bearing system). Importantly, compared with SVM classifier, GRBM based on deep learning model showed ability of posing the best fault classification rate. In [212], an intelligent FDD of bearings and gearboxes based on deep neural networks tool with massive vibration data is introduced. Moreover, the proposed method is applied in different health conditions among different operating conditions. To overcome the deficiencies of the traditional shallow smart FDD methods (i.e., ANN), deep neural networks (DNNs) are employed to seek the useful diagnostic data from the vibration signals and to approximate complex nonlinear functions. Importantly, this work also highlights the superiority diagnosis accuracy method and comparative analysis with the traditional approaches. In [213], an FDD for rolling bearings approach based on improved convolutional deep belief network using a vibration signal is proposed. Moreover, to enhance the feature learning ability, convolutional deep belief network (CDBN) model is employed along with Gaussian visible units. Consequently, exponential moving average (EMA) technique is used to further elevate the performance of overall system. Importantly, the proposed CDBN based method is more robust and effective than the normal shallow methods.

In [214], a multimodal deep SVM classification (MDSVC) approach with homologous features FDD using vibration signals is introduced. In this approach, time and frequency, as well as wavelet modalities, are separated first. For each modality, to learn the patterns and different representations for different features, Gaussian-Bernoulli deep Boltzmann machine (GDBM) is used. Finally, an SVM classifier is also employed to combine GDBMs with different sensory system to obtain the improved version of MDSVC method. Importantly, compared with representative deep and traditional shallow learning methods, the suggested data aggregation with a DL-based method achieved the best classification rate. In [215], a feature learning model for CM and FDD of the bearing based on convolutional neural networks using vibration signals is proposed. Moreover, the end-to-end machine learning system is developed. Importantly, compared with a classical approach (i.e., random forest classifier), the overall accuracy is six times better than the classical approaches. In [216], a deep neural network FDD approach which uses vibration signals for analysis is presented for rolling bearing. Moreover, time domain, frequency domain, and time-frequency domain techniques are applied to obtain the feature vector. In this research study, three deep neural network models are employed as a fault condition monitoring of rolling bearing, including deep Boltzmann machines, deep belief networks, and stacked autoencoders. Importantly, the classification accuracy for those techniques is highly reliable (achieved more than 99%). In [217], deep learning enabled FDD approach using time-frequency image analysis of rolling element bearings is proposed. Moreover, deep neural network, image representation, and time-frequency (TF) analysis techniques are used together. The vibration data is mapped into time-frequency domain in order to draw relevant image representations. Short-time Fourier transform, wavelet transform, and Hilbert-Huang transforms are used as feature extraction methods. Importantly, a deep convolutional neural network (CNN) is applied in the classification stage. Furthermore, the proposed CNN architecture based approach showed high fault detection ability for noisy environments and with less learnable parameters. In [218], a new deep residual learning-based fault diagnosis method for the rolling bearing in rotating machinery using vibration signals is proposed. The main contribution of this research study is to improve the information flow throughout the deep neural network. Moreover, CNN is adopted in feature extraction and 1D convolutional layers are employed to obtain the feature vector. In addition, basic neural network, deep neural networks, stacked autoencoders, convolutional neural network, and deep convolutional neural networks are also employed for comparisons. As a result, the proposed approach could be effectively trained with a high classification accuracy. In [219], a new CNN based on the LeNet-5 FDD method is proposed for bearings using vibration signals. In this method, the vibration signal is decomposed into two-dimensional images; thus, the features are extracted from the converted image. As a result, the proposed method showed potentiality in the data-driven fault diagnosis field. However, the prediction accuracy was about 99 %.

Table 3 summarizes AI algorithms used in FDD of IM [193, 220–227].

Table 3: AI algorithms used in CM and FDD of IM.

The method	Highlights
Random forest	(i) The small number of training samples is required (ii) There is low computational cost (iii) There is good performance for high-dimensional data
Bayesian network	(i) There is high classification speed (ii) It is useful if the prior knowledge is reliable (iii) There is low storage need (iv) It is computationally expensive (v) There is prior beliefs' problem
KNN	(i) There is low classification speed (ii) It is simple and easy to apply (iii) There is poor performance for high-dimensional data (iii) It is memory-intensive (iv) It is noise sensitive (v) It is computationally expensive
SVM	(i) There is good performance for high-dimensional data (ii) There are low storage needs (iii) There is high classification speed (iv) It is not efficient for big data (v) It is noise sensitive (vi) It has good accuracy
ANN	(i) There is fault tolerance (ii) There is high classification speed (iii) There is parallelism (iv) There is hidden training problem (v) It is efficient for big data (vi) It is computationally expensive (vii) There is black box behavior problem
Neuro-fuzzy	(i) There is good performance for high-dimensional data (ii) It has good diagnosis accuracy (iii) There is robustness (iv) There is parallelism (v) It is efficient for big data (vi) There is black box behavior problem (vii) It has self-learning capability
DNN	(i) There is good classification speed (ii) There are automatic fault diagnosis and detection (iii) There is good accuracy (iv) There is parallelism (v) It has complex and deep architecture (vi) It is feature extraction free (vii) It is computationally expensive (viii) There are massive parallel computations (ix) It is efficient for big data (x) There is long time training problem (xi) A large number of training samples are required

As a result of this study, it can be showed that both DL and ML algorithms can be used as an intelligent diagnostic method of bearings for IM. Conventional ML algorithms manually extract the features, where DL algorithms learn the feature directly from input data. So, human expertise and prior knowledge are not required [228]. Table 4 shows a comparison between DL and ML algorithms for bearings CM and FDD. Importantly, for small datasets, conventional ML algorithms show better accuracy results than DL algorithms, whereas, for big datasets, DL algorithms show better accuracy results than conventional ML algorithms. According to [144], as a classification accuracy between SVM, KNN, and CNN, the classification accuracy was 81.96, 86.25, and 82.70, respectively, for small dataset, and 83.04, 87.85, and 89.26, respectively, for big dataset.

4. Challenges and Future Trends

Intelligent CM and FDD method is considered to be as a key factor of fault diagnosis development [43, 229]. However, this field still faces many challenges [35, 230, 231]. This section summarizes the challenges and the future trends of AI methods in CM and FDD of rolling element bearings for IM [232–235]:

(i) Dealing with all operating conditions, sensitivity to the noise, and working environment (indoor/outdoor) should be taken in a high consideration when CM and FDD method is built and developed.

(ii) Benefit from all strength points for each AI algorithm is crucial for building a hybrid intelligent, online, low cost, nonintrusive, and large scale CM and FDD for industrial machinery.

(iii) Developing highly accurate sensors with cost-effective, fast, wireless, and energy-efficient characteristics is highly required.

(iv) In order to increase diagnostic performance, knowledge-based intelligent systems should be further investigated.

(v) Automatic, online, continuous, and wireless diagnosis approach with better detection capabilities based on IoT, expert systems, and AI may be employed.

(vi) Compound faults and fault severity detection and diagnosis approaches should be explored.

(vii) CM and FDD of multimotor systems have to be proposed.

(viii) Integrated and comprehensive CM and FDD system to deal with all faults of IM and to determine the damage level and severity should be proposed.

(ix) Industrial Internet of things (IIoT) technologies a long with AI should be used to develop high performance CM and FDD methods.

(x) Big data problem is how to pick useful diagnostic information from big data obtained by different sensors quickly.

(xi) Data from different sensors should be used to develop an effective heterogeneous methodology.

(xii) In order to achieve high availability of IM and to reduce maintenance cost, fault-tolerant FDD and

Table 4: DL vs. ML for bearing CM and FDD.

The point	DL algorithms	Conventional ML algorithms
Feature extraction	Automated	Manual
Classification	Simultaneous feature learning and classification	Feature extraction and classification are separated
Human expertise	Not required	Required
Prior knowledge	Not required	Required
External noise	Better	Sensitive
Frequent change	Better	Sensitive
Diagnostic accuracy	High accuracy	Lesser accuracy
Dataset	Efficient for big data	Efficient for small datasets
Computational training cost	Expensive	Lesser computational training cost is required
Hardware requirements	GPU is required	CPU is efficient

prognostic techniques have to be further investigated.

5. Conclusions

Importantly, enhancing the reliability, availability, and safety to reduce maintenance cost of modern industrial systems and applications is crucial. Thus, following up the health of the machinery such as induction motor (IM) is vital. The bearing is a critical component in IM. Therefore, robust and intelligent condition monitoring (CM) and fault detection and diagnosis (FDD) methods are highly needed to enhance detection, diagnosis, monitoring, and prognosis capabilities. In this paper, a general descriptive review of intelligent diagnostics methods of rolling element bearings for IM is presented. The advantages and limitations of each method are highlighted. Finally, challenges and future trends are also discussed.

Data Availability

The data used to support the findings of this study are included within the article.

Conflicts of Interest

The authors declare that there are no conflicts of interest regarding the publication of this paper.

References

[1] A. González-Muñiz, I. Díaz, and A. A. Cuadrado, "DCNN for condition monitoring and fault detection in rotating machines and its contribution to the understanding of machine nature," *Heliyon*, vol. 6, no. 2, Article ID e03395, 2020.

[2] A. Choudhary, S. Jamwal, D. Goyal, R. K. Dang, and S. Sehgal, "Condition monitoring of induction motor using internet of things (IoT)," in *Recent Advances in Mechanical Engineering*, pp. 353–365, Springer, Berlin, Germany, 2020.

[3] G. Yu, T. Lin, Z. Wang, and Y. Li, "Time-reassigned multisynchrosqueezing transform for bearing fault diagnosis of rotating machinery," *IEEE Transactions on Industrial Electronics*, p. 1, 2020.

[4] Y. Chen, G. Peng, Z. Zhu, and S. Li, "A novel deep learning method based on attention mechanism for bearing remaining useful life prediction," *Applied Soft Computing*, vol. 86, Article ID 105919, 2020.

[5] X. Chen, S. Wang, B. Qiao, and Q. Chen, "Basic research on machinery fault diagnostics: Past, present, and future trends," *Frontiers of Mechanical Engineering*, vol. 13, no. 2, pp. 264–291, 2018.

[6] M. S. Kan, A. C. C. Tan, and J. Mathew, "A review on prognostic techniques for non-stationary and non-linear rotating systems," *Mechanical Systems and Signal Processing*, vol. 62-63, pp. 1–20, 2015.

[7] L. Song, H. Wang, and P. Chen, "Intelligent diagnosis method for machinery by sequential auto-reorganization of histogram," *ISA Transactions*, vol. 87, pp. 154–162, 2019.

[8] C. Lu, Y. Wang, M. Ragulskis, and Y. Cheng, "Fault diagnosis for rotating machinery: a method based on image processing," *PLoS One*, vol. 11, no. 10, Article ID e0164111, 2016.

[9] C. Peeters, J. Antoni, and J. Helsen, "Blind filters based on envelope spectrum sparsity indicators for bearing and gear vibration-based condition monitoring," *Mechanical Systems and Signal Processing*, vol. 138, Article ID 106556, 2020.

[10] W. Qian, S. Li, P. Yi, and K. Zhang, "A novel transfer learning method for robust fault diagnosis of rotating machines under variable working conditions," *Measurement*, vol. 138, pp. 514–525, 2019.

[11] B. Wang, Y. Lei, T. Yan, N. Li, and L. Guo, "Recurrent convolutional neural network: a new framework for remaining useful life prediction of machinery," *Neurocomputing*, vol. 379, pp. 117–129, 2020.

[12] D. Verstraete, E. Droguett, and M. Modarres, "A deep adversarial approach based on multi-sensor fusion for semi-supervised remaining useful life prognostics," *Sensors*, vol. 20, no. 1, p. 176, 2020.

[13] E. Lughofer and M. Sayed-Mouchaweh, "Prologue: Predictive maintenance in dynamic systems," in *Predictive Maintenance in Dynamic Systems*, pp. 1–23, Springer, Berlin, Germany, 2019.

[14] Y. Zheng, "Predicting remaining useful life based on Hilbert–Huang entropy with degradation model," *Journal of Electrical and Computer Engineering*, vol. 2019, pp. 1–11, Article ID 3203959, 2019.

[15] X. Yan, Y. Liu, and M. Jia, "Multiscale cascading deep belief network for fault identification of rotating machinery under various working conditions," *Knowledge-Based Systems*, vol. 193, Article ID 105484, 2020.

[16] J. Liu, Z. Xu, L. Zhou, W. Yu, and Y. Shao, "A statistical feature investigation of the spalling propagation assessment for a ball bearing," *Mechanism and Machine Theory*, vol. 131, pp. 336–350, 2019.

[17] V. T. Tran and B.-S. Yang, "An intelligent condition-based maintenance platform for rotating machinery," *Expert Systems with Applications*, vol. 39, no. 3, pp. 2977–2988, 2012.

[18] M. Irfan, R. I. Nordin Saad, V. S. Asirvadam, A. Alwadie, and M. Aman, "An assessment on the non-invasive methods for condition monitoring of induction motors," *Fault Diagnosis and Detection*, p. 87, 2017.

[19] C. Huang, L. D. Xu, H. Cai, G. Li, J. Du, and L. Jiang, "A context-based service matching approach towards functional reliability for industrial systems," *Enterprise Information Systems*, vol. 13, no. 2, pp. 196–218, 2019.

[20] I. Mistry, S. Tanwar, S. Tyagi, and N. Kumar, "Blockchain for 5G-enabled IoT for industrial automation: A systematic review, solutions, and challenges," *Mechanical Systems and Signal Processing*, vol. 135, Article ID 106382, 2020.

[21] C. P. Gatica and M. Platzner, "Adaptable realization of industrial analytics functions on edge-devices using reconfigurable architectures," in *Machine Learning for Cyber Physical Systems*, pp. 73–80, Springer, Berlin, Germany, 2020.

[22] J. L. Contreras-Hernandez, D. L. Almanza-Ojeda, S. Ledesma et al., "Quaternion signal analysis algorithm for induction motor fault detection," *IEEE Transactions on Industrial Electronics*, vol. 66, no. 11, pp. 8843–8850, 2019.

[23] G. Lian, J. Zhang, B. Chen, F. Ban, Z. Hou, and H. Li, "Design and experimental study of the wireless online monitoring system of a high-temperature superconducting machine," *IEEE Transactions on Applied Superconductivity*, vol. 29, no. 2, pp. 1–5, 2019.

[24] S. Muthanandan and K. A. B. Nor, "Condition monitoring and assessment for rotating machinery," in *Rotating Machineries*, pp. 1–22, Springer, Berlin, Germany, 2019.

[25] A. Glowacz, "Fault diagnosis of single-phase induction motor based on acoustic signals," *Mechanical Systems and Signal Processing*, vol. 117, pp. 65–80, 2019.

[26] M. González, O. Salgado, X. Hernandez, J. Croes, B. Pluymers, and W. Desmet, "Model-based condition monitoring of guiding rails in electro-mechanical systems," *Mechanical Systems and Signal Processing*, vol. 120, pp. 630–641, 2019.

[27] M. Khazaee, A. Rezaniakolaie, A. Moosavian, and L. Rosendahl, "A novel method for autonomous remote condition monitoring of rotating machines using piezoelectric energy harvesting approach," *Sensors and Actuators A: Physical*, vol. 295, pp. 37–50, 2019.

[28] D. Crivelli, S. Hutt, A. Clarke, P. Borghesani, Z. Peng, and R. Randall, "Condition monitoring of rotating machinery with acoustic emission: A British–Australian collaboration," in *Asset Intelligence through Integration and Interoperability and Contemporary Vibration Engineering Technologies*, pp. 119–128, Springer, Berlin, Germany, 2019.

[29] T. Wang, G. Lu, and P. Yan, "Multi-sensors based condition monitoring of rotary machines: An approach of multidimensional time-series analysis," *Measurement*, vol. 134, pp. 326–335, 2019.

[30] V. Atamuradov, K. Medjaher, F. Camci, N. Zerhouni, P. Dersin, and B. Lamoureux, "Machine health indicator construction framework for failure diagnostics and prognostics," *Journal of Signal Processing Systems*, vol. 92, no. 6, pp. 591–609, 2020.

[31] Y. Wang, Z. Wei, and J. Yang, "Feature trend extraction and adaptive density peaks search for intelligent fault diagnosis of machines," *IEEE Transactions on Industrial Informatics*, vol. 15, no. 1, pp. 105–115, 2019.

[32] B. Luo, H. Wang, H. Liu, B. Li, and F. Peng, "Early fault detection of machine tools based on deep learning and dynamic identification," *IEEE Transactions on Industrial Electronics*, vol. 66, no. 1, pp. 509–518, 2019.

[33] G. Jiang, H. He, J. Yan, and P. Xie, "Multiscale convolutional neural networks for fault diagnosis of wind turbine gearbox," *IEEE Transactions on Industrial Electronics*, vol. 66, no. 4, pp. 3196–3207, 2019.

[34] H. Wang and P. Chen, "Intelligent diagnosis method for rolling element bearing faults using possibility theory and neural network," *Computers & Industrial Engineering*, vol. 60, no. 4, pp. 511–518, 2011.

[35] Y. Liu and A. M. Bazzi, "A review and comparison of fault detection and diagnosis methods for squirrel-cage induction motors: State of the art," *ISA Transactions*, vol. 70, pp. 400–409, 2017.

[36] G.-Q. Jiang, P. Xie, X. Wang, M. Chen, and Q. He, "Intelligent fault diagnosis of rotary machinery based on unsupervised multiscale representation learning," *Chinese Journal of Mechanical Engineering*, vol. 30, no. 6, pp. 1314–1324, 2017.

[37] Z. Gao, C. Cecati, and S. X. Ding, "A survey of fault diagnosis and fault-tolerant techniques-Part I: fault Diagnosis with model-based and signal-based approaches," *IEEE Transactions on Industrial Electronics*, vol. 62, no. 6, pp. 3757–3767, 2015.

[38] Z. Feng, M. Liang, and F. Chu, "Recent advances in time-frequency analysis methods for machinery fault diagnosis: A review with application examples," *Mechanical Systems and Signal Processing*, vol. 38, no. 1, pp. 165–205, 2013.

[39] A. Taheri-Garavand, H. Ahmadi, M. Omid et al., "An intelligent approach for cooling radiator fault diagnosis based on infrared thermal image processing technique," *Applied Thermal Engineering*, vol. 87, pp. 434–443, 2015.

[40] B. Peng, H. Xia, X. Ma, S. Zhu, Z. Wang, and J. Zhang, "A mixed intelligent condition monitoring method for nuclear power plant," *Annals of Nuclear Energy*, vol. 140, Article ID 107307, 2020.

[41] C. Wu, P. Jiang, C. Ding, F. Feng, and T. Chen, "Intelligent fault diagnosis of rotating machinery based on one-dimensional convolutional neural network," *Computers in Industry*, vol. 108, pp. 53–61, 2019.

[42] Y. Merizalde, L. Hernández-Callejo, and O. Duque-Perez, "State of the art and trends in the monitoring, detection and diagnosis of failures in electric induction motors," *Energies*, vol. 10, no. 7, p. 1056, 2017.

[43] A. Choudhary, D. Goyal, S. L. Shimi, and A. Akula, "Condition monitoring and fault diagnosis of induction motors: A review," *Archives of Computational Methods in Engineering*, vol. 26, no. 4, pp. 1221–1238, 2018.

[44] S. Nandi, H. A. Toliyat, and X. Li, "Condition monitoring and fault diagnosis of electrical motors-A review," *IEEE Transactions on Energy Conversion*, vol. 20, no. 4, pp. 719–729, 2005.

[45] Y. Trachi, E. Elbouchikhi, V. Choqueuse, and M. E. H. Benbouzid, "Induction machines fault detection based on subspace spectral estimation," *IEEE Transactions on Industrial Electronics*, vol. 63, no. 9, pp. 5641–5651, 2016.

[46] M. Seera, C. P. Lim, D. Ishak, and H. Singh, "Application of the fuzzy min-max neural network to fault detection and diagnosis of induction motors," *Neural Computing and Applications*, vol. 23, no. S1, pp. 191–200, 2012.

[47] A. Widodo, B.-S. Yang, D.-S. Gu, and B.-K. Choi, "Intelligent fault diagnosis system of induction motor based on transient

current signal," *Mechatronics*, vol. 19, no. 5, pp. 680–689, 2009.

[48] B. V. Gopal and E. Shivakumar, "Design and simulation of neuro-fuzzy controller for indirect vector-controlled induction motor drive," in *Data Analytics and Learning*, pp. 155–167, Springer, Berlin, Germany, 2019.

[49] N. Rajeswaran, M. Lakshmi Swarupa, T. Sanjeeva Rao, and K. Chetaswi, "Hybrid artificial intelligence based fault diagnosis of svpwm voltage source inverters for induction motor," *Materials Today: Proceedings*, vol. 5, no. 1, pp. 565–571, 2018.

[50] P. Majumdar, P. Mishra, S. Sarkar, and S. Das, "State-space model based induction motor stator winding inter-turn fault detection technique," in *Advances in Computer, Communication and Control*, pp. 225–236, Springer, Berlin, Germany, 2019.

[51] P. Donolo, C. Pezzani, G. Bossio, C. De Angelo, and M. Donolo, "Derating of induction motors due to power quality issues considering the motor efficiency class," *IEEE Transactions on Industry Applications*, vol. 56, 2020.

[52] A. Glowacz and Z. Glowacz, "Diagnosis of the three-phase induction motor using thermal imaging," *Infrared Physics & Technology*, vol. 81, pp. 7–16, 2017.

[53] A. A. Z. Diab, A.-H. M. Al-Sayed, H. H. A. Mohammed, and Y. S. Mohammed, "Literature review of induction motor drives," in *Development of Adaptive Speed Observers for Induction Machine System Stabilization*, pp. 7–18, Springer, Berlin, Germany, 2020.

[54] M. M. Stopa, M. R. Resende, A.-S. A. Luiz, J. C. G. Justino, G. G. Rodrigues, and B. J. Cardoso Filho, "A simple torque estimator for in-service efficiency determination of inverter fed induction motors," *IEEE Transactions on Industry Applications*, vol. 56, 2020.

[55] G. Cirrincione, V. Randazzo, R. R. Kumar, M. Cirrincione, and E. Pasero, "Growing Curvilinear Component Analysis (GCCA) for stator fault detection in induction machines," in *Neural Approaches to Dynamics of Signal Exchanges*, pp. 235–244, Springer, Berlin, Germany, 2020.

[56] M. J. Akhtar and R. K. Behera, "Space vector modulation for distributed inverter fed induction motor drive for electric vehicle application," *IEEE Journal of Emerging and Selected Topics in Power Electronics*, p. 1, 2020.

[57] M. Stopa, C. Lima, B. Cardoso, L. de Miranda, A.-S. Luiz, and C. Martinez, "Detection of gaseous nuclei in centrifugal motor pumps by analysis of their estimated torque," *IEEE Transactions on Industry Applications*, 2020.

[58] S. K. Gundewar and P. V. Kane, "Fuzzy FMEA analysis of induction motor and overview of diagnostic techniques to reduce risk of failure," in *Reliability, Safety and Hazard Assessment for Risk-Based Technologies*, pp. 927–939, Springer, Berlin, Germany, 2020.

[59] S. Perumandla, P. Upadhyay, A. Jayalaxmi, and J. P. Nasam, "Modulated frequency triangular carrier based space vector PWM technique for spreading induction motor acoustic noise spectrum," in *Proceedings of the Advances in Decision Sciences, Image Processing, Security and Computer Vision*, pp. 470–480, Allahbabad, Uttar Pradesh, August 2020.

[60] J. K. Jain, S. Ghosh, and S. Maity, "Concurrent PI controller design for indirect vector controlled induction motor," *Asian Journal of Control*, vol. 22, no. 1, pp. 130–142, 2020.

[61] W. F. Godoy, I. N. da Silva, T. D. Lopes, A. Goedtel, and R. H. C. Palácios, "Application of intelligent tools to detect and classify broken rotor bars in three-phase induction motors fed by an inverter," *IET Electric Power Applications*, vol. 10, no. 5, pp. 430–439, 2016.

[62] A. Glowacz, W. Glowacz, J. Kozik et al., "Detection of deterioration of three-phase induction motor using vibration signals," *Measurement Science Review*, vol. 19, no. 6, pp. 241–249, 2019.

[63] S. B. Jiang, P. K. Wong, R. Guan, Y. Liang, and J. Li, "An efficient fault diagnostic method for three-phase induction motors based on incremental broad learning and non-negative matrix factorization," *IEEE Access*, vol. 7, pp. 17780–17790, 2019.

[64] M. Al-Badri, P. Pillay, and P. Angers, "A novel in situ efficiency estimation algorithm for three-phase induction motors operating with distorted unbalanced voltages," *IEEE Transactions on Industry Applications*, vol. 53, no. 6, pp. 5338–5347, 2017.

[65] K. S. Gaeid and H. W. Ping, "Wavelet fault diagnosis and tolerant of induction motor: A review," *International Journal of the Physical Sciences*, vol. 6, no. 3, pp. 358–376, 2011.

[66] J. Liu, "A dynamic modelling method of a rotor-roller bearing-housing system with a localized fault including the additional excitation zone," *Journal of Sound and Vibration*, vol. 469, Article ID 115144, 2020.

[67] J. Ma, J. Wu, Y. Fan, and X. Wang, "The rolling bearing fault feature extraction based on the LMD and envelope demodulation," *Mathematical Problems in Engineering*, vol. 2015, pp. 1–13, Article ID 429185, 2015.

[68] F. Xu, Z. Huang, F. Yang, D. Wang, and K. L. Tsui, "Constructing a health indicator for roller bearings by using a stacked auto-encoder with an exponential function to eliminate concussion," *Applied Soft Computing*, vol. 89, Article ID 106119, 2020.

[69] Y. Ying, J. Li, Z. Chen, and J. Guo, "Study on rolling bearing on-line reliability analysis based on vibration information processing," *Computers & Electrical Engineering*, vol. 69, pp. 842–851, 2018.

[70] L. Frosini and E. Bassi, "Stator current and motor efficiency as indicators for different types of bearing faults in induction motors," *IEEE Transactions on Industrial Electronics*, vol. 57, no. 1, pp. 244–251, 2009.

[71] L. Ciabattoni, F. Ferracuti, A. Freddi, and A. Monteriu, "Statistical spectral analysis for fault diagnosis of rotating machines," *IEEE Transactions on Industrial Electronics*, vol. 65, no. 5, pp. 4301–4310, 2017.

[72] A. Sharma, M. Amarnath, and P. Kankar, "Feature extraction and fault severity classification in ball bearings," *Journal of Vibration and Control*, vol. 22, no. 1, pp. 176–192, 2016.

[73] A. K. Choudhary and D. A. Khan, "Introduction to conditioning monitoring of mechanical systems," in *Soft Computing in Condition Monitoring and Diagnostics of Electrical and Mechanical Systems*, pp. 205–230, Springer, Berlin, Germany, 2020.

[74] M. Cerrada, R.-V. Sánchez, C. Li et al., "A review on data-driven fault severity assessment in rolling bearings," *Mechanical Systems and Signal Processing*, vol. 99, pp. 169–196, 2018.

[75] Y. Zhang, X. Li, L. Gao, W. Chen, and P. Li, "Intelligent fault diagnosis of rotating machinery using a new ensemble deep auto-encoder method," *Measurement*, vol. 151, Article ID 107232, 2020.

[76] X. Zhao, M. Jia, and M. Lin, "Deep Laplacian Auto-encoder and its application into imbalanced fault diagnosis of rotating machinery," *Measurement*, vol. 152, Article ID 107320, 2020.

[77] P. J. Tavner, "Review of condition monitoring of rotating electrical machines," *IET Electric Power Applications*, vol. 2, no. 4, pp. 215–247, 2008.

[78] S. A. McInerny and Y. Dai, "Basic vibration signal processing for bearing fault detection," *IEEE Transactions on Education*, vol. 46, no. 1, pp. 149–156, 2003.

[79] M. E. H. Benbouzid, H. Nejjari, R. Beguenane, and M. Vieira, "Induction motor asymmetrical faults detection using advanced signal processing techniques," *IEEE Transactions on Energy Conversion*, vol. 14, no. 2, pp. 147–152, 1999.

[80] S. Dutta, S. K. Pal, S. Mukhopadhyay, and R. Sen, "Application of digital image processing in tool condition monitoring: A review," *CIRP Journal of Manufacturing Science and Technology*, vol. 6, no. 3, pp. 212–232, 2013.

[81] Y. S. Wong, A. Y. C. Nee, X. Q. Li, and C. Reisdorf, "Tool condition monitoring using laser scatter pattern," *Journal of Materials Processing Technology*, vol. 63, no. 1–3, pp. 205–210, 1997.

[82] M. Castejon, E. Alegre, J. Barreiro, and L. K. Hernández, "On-line tool wear monitoring using geometric descriptors from digital images," *International Journal of Machine Tools and Manufacture*, vol. 47, no. 12-13, pp. 1847–1853, 2007.

[83] A. K. Al-Musawi, F. Anayi, and M. Packianather, "Three-phase induction motor fault detection based on thermal image segmentation," *Infrared Physics & Technology*, vol. 104, Article ID 103140, 2020.

[84] B.-S. Yang, T. Han, and W.-W. Hwang, "Fault diagnosis of rotating machinery based on multi-class support vector machines," *Journal of Mechanical Science and Technology*, vol. 19, no. 3, pp. 846–859, 2005.

[85] Y. D. Nyanteh, S. K. Srivastava, C. S. Edrington, and D. A. Cartes, "Application of artificial intelligence to stator winding fault diagnosis in permanent magnet synchronous machines," *Electric Power Systems Research*, vol. 103, pp. 201–213, 2013.

[86] L.-l. Jiang, H.-k. Yin, X.-j. Li, and S.-w. Tang, "Fault diagnosis of rotating machinery based on multisensor information fusion using SVM and time-domain features," *Shock and Vibration*, vol. 2014, pp. 1–8, Article ID 418178, 2014.

[87] E. Ayaz, A. Öztürk, S. Şeker, and B. R. Upadhyaya, "Fault detection based on continuous wavelet transform and sensor fusion in electric motors," *COMPEL - The International Journal for Computation and Mathematics in Electrical and Electronic Engineering*, vol. 28, no. 2, pp. 454–470, 2009.

[88] X. Liu, L. Ma, and J. Mathew, "Machinery fault diagnosis based on fuzzy measure and fuzzy integral data fusion techniques," *Mechanical Systems and Signal Processing*, vol. 23, no. 3, pp. 690–700, 2009.

[89] G. Niu, T. Han, B.-S. Yang, and A. C. C. Tan, "Multi-agent decision fusion for motor fault diagnosis," *Mechanical Systems and Signal Processing*, vol. 21, no. 3, pp. 1285–1299, 2007.

[90] C. Li, R.-V. Sanchez, G. Zurita, M. Cerrada, D. Cabrera, and R. E. Vásquez, "Gearbox fault diagnosis based on deep random forest fusion of acoustic and vibratory signals," *Mechanical Systems and Signal Processing*, vol. 76-77, pp. 283–293, 2016.

[91] B. Bagheri, H. Ahmadi, and R. Labbafi, "Application of data mining and feature extraction on intelligent fault diagnosis by artificial neural network and *k*-nearest neighbor," in *Proceedings of the Electrical Machines (ICEM), 2010 XIX International Conference*, pp. 1–7, Rome, Italy, September 2010.

[92] A. Purarjomandlangrudi, A. H. Ghapanchi, and M. Esmalifalak, "A data mining approach for fault diagnosis: an application of anomaly detection algorithm," *Measurement*, vol. 55, pp. 343–352, 2014.

[93] J. Blair and A. Shirkhodaie, "Diagnosis and prognosis of bearings using data mining and numerical visualization techniques in system theory," in *Proceedings of the 33rd Southeastern Symposium*, pp. 395–399, Ohio University, Athens, OH, USA, 2001.

[94] D. He, R. Ruoyu Li, J. Junda Zhu, and M. Zade, "Data mining based full ceramic bearing fault diagnostic system using AE sensors," *IEEE Transactions on Neural Networks*, vol. 22, no. 12, pp. 2022–2031, 2011.

[95] D. He, R. Li, and J. Zhu, "Plastic bearing fault diagnosis based on a two-step data mining approach," *IEEE Transactions on Industrial Electronics*, vol. 60, no. 8, pp. 3429–3440, 2013.

[96] A. Verma, Z. Zhang, and A. Kusiak, "Modeling and prediction of gearbox faults with data-mining algorithms," *Journal of Solar Energy Engineering*, vol. 135, no. 3, Article ID 031007, 2013.

[97] B. Yang, D. Lim, and A. Tan, "VIBEX: An expert system for vibration fault diagnosis of rotating machinery using decision tree and decision table," *Expert Systems with Applications*, vol. 28, no. 4, pp. 735–742, 2005.

[98] J.-D. Wu, M. R. Bai, F.-C. Su, and C.-W. Huang, "An expert system for the diagnosis of faults in rotating machinery using adaptive order-tracking algorithm," *Expert Systems with Applications*, vol. 36, no. 3, pp. 5424–5431, 2009.

[99] T. Berredjem and M. Benidir, "Bearing faults diagnosis using fuzzy expert system relying on an Improved Range Overlaps and Similarity method," *Expert Systems with Applications*, vol. 108, pp. 134–142, 2018.

[100] J. Liu and Y. Shao, "Overview of dynamic modelling and analysis of rolling element bearings with localized and distributed faults," *Nonlinear Dynamics*, vol. 93, no. 4, pp. 1765–1798, 2018.

[101] J. Liu and Y. Shao, "Dynamic modeling for rigid rotor bearing systems with a localized defect considering additional deformations at the sharp edges," *Journal of Sound and Vibration*, vol. 398, pp. 84–102, 2017.

[102] D. D. Reigosa, J. M. Guerrero, A. B. Diez, and F. Briz, "Rotor temperature estimation in doubly-fed induction machines using rotating high-frequency signal injection," *IEEE Transactions on Industry Applications*, vol. 53, no. 4, pp. 3652–3662, 2017.

[103] A. Mohammed and S. Djurovic, "Stator winding internal thermal monitoring and analysis using in situ FBG sensing technology," *IEEE Transactions on Energy Conversion*, vol. 33, no. 3, pp. 1508–1518, 2018.

[104] Z. Zhao, F. Ji, Y. Guan, J. Xu, and X. Yuan, "Method and experiment of temperature collaborative monitoring based on characteristic points for tilting pad bearings," *Tribology International*, vol. 114, pp. 77–83, 2017.

[105] L. B. Visnadi and H. F. de Castro, "Influence of bearing clearance and oil temperature uncertainties on the stability threshold of cylindrical journal bearings," *Mechanism and Machine Theory*, vol. 134, pp. 57–73, 2019.

[106] S. Bagavathiappan, B. B. Lahiri, T. Saravanan, J. Philip, and T. Jayakumar, "Infrared thermography for condition monitoring - A review," *Infrared Physics & Technology*, vol. 60, pp. 35–55, 2013.

[107] J. Liu, Y. Shao, and T. C. Lim, "Vibration analysis of ball bearings with a localized defect applying piecewise response

function," *Mechanism and Machine Theory*, vol. 56, pp. 156–169, 2012.

[108] T. Y. Wu and Y. L. Chung, "Misalignment diagnosis of rotating machinery through vibration analysis via the hybrid EEMD and EMD approach," *Smart Materials and Structures*, vol. 18, no. 9, Article ID 095004, 2009.

[109] H. Y. Jiang and P. Chen, "Analysis and sensitivity evaluation of AE signals and vibration signals for fault diagnosis of low-speed rotating machinery," *Applied Mechanics and Materials*, vol. 128-129, pp. 79–84, 2011.

[110] T. H. Loutas, D. Roulias, E. Pauly, and V. Kostopoulos, "The combined use of vibration, acoustic emission and oil debris on-line monitoring towards a more effective condition monitoring of rotating machinery," *Mechanical Systems and Signal Processing*, vol. 25, no. 4, pp. 1339–1352, 2011.

[111] A. Medoued, M. Mordjaoui, Y. Soufi, and D. Sayad, "Induction machine bearing fault diagnosis based on the axial vibration analytic signal," *International Journal of Hydrogen Energy*, vol. 41, no. 29, pp. 12688–12695, 2016.

[112] J. K. Sinha and K. Elbhbah, "A future possibility of vibration based condition monitoring of rotating machines," *Mechanical Systems and Signal Processing*, vol. 34, no. 1-2, pp. 231–240, 2013.

[113] G. K. Chaturved and D. W. Thomas, "Adaptive noise cancelling and condition monitoring," *Journal of Sound and Vibration*, vol. 76, no. 3, pp. 391–405, 1981.

[114] T. Wang, M. Liang, J. Li, W. Cheng, and C. Li, "Bearing fault diagnosis under unknown variable speed via gear noise cancellation and rotational order sideband identification," *Mechanical Systems and Signal Processing*, vol. 62-63, pp. 30–53, 2015.

[115] B. Lu and V. C. Gungor, "Online and remote motor energy monitoring and fault diagnostics using wireless sensor networks," *IEEE Transactions on Industrial Electronics*, vol. 56, no. 11, pp. 4651–4659, 2009.

[116] S. Cheng, K. Tom, L. Thomas, and M. Pecht, "A wireless sensor system for prognostics and health management," *IEEE Sensors Journal*, vol. 10, no. 4, pp. 856–862, 2010.

[117] J. Timperley, "Incipient fault identification through neutral RF monitoring of large rotating machines," *IEEE Transactions on Power Apparatus and Systems*, vol. 102, no. 3, pp. 693–698, 1983.

[118] J. Henson and C. Restrepo, "Devices, systems, and methods for adaptive RF sensing in arc fault detection," Google Patents, 2008.

[119] A. Agoston, C. Schneidhofer, N. Dörr, and B. Jakoby, "A concept of an infrared sensor system for oil condition monitoring," *e & i Elektrotechnik und informationstechnik*, vol. 125, no. 3, pp. 71–75, 2008.

[120] A. R. Caneca, M. F. Pimentel, R. K. H. Galvão et al., "Assessment of infrared spectroscopy and multivariate techniques for monitoring the service condition of diesel-engine lubricating oils," *Talanta*, vol. 70, no. 2, pp. 344–352, 2006.

[121] M. S. Jadin and S. Taib, "Recent progress in diagnosing the reliability of electrical equipment by using infrared thermography," *Infrared Physics & Technology*, vol. 55, no. 4, pp. 236–245, 2012.

[122] S. Bagavathiappan, T. Saravanan, N. P. George, J. Philip, T. Jayakumar, and B. Raj, "Condition monitoring of exhaust system blowers using infrared thermography," *Insight - Non-destructive Testing and Condition Monitoring*, vol. 50, no. 9, pp. 512–515, 2008.

[123] N. Utami, Y. Tamsir, A. Pharmatrisanti, H. Gumilang, B. Cahyono, and R. Siregar, "Evaluation condition of transformer based on infrared thermography results," in *Proceedings of the IEEE 9th International Conference*, pp. 1055–1058, China, 2009.

[124] A. S. N. Huda and S. Taib, "Suitable features selection for monitoring thermal condition of electrical equipment using infrared thermography," *Infrared Physics & Technology*, vol. 61, pp. 184–191, 2013.

[125] T. D. Lopes, A. Goedtel, R. H. C. Palácios, W. F. Godoy, and R. M. de Souza, "Bearing fault identification of three-phase induction motors bases on two current sensor strategy," *Soft Computing*, vol. 21, no. 22, pp. 6673–6685, 2016.

[126] D. Diallo, M. E. H. Benbouzid, D. Hamad, and X. Pierre, "fault detection and diagnosis in an induction machine drive: a pattern recognition approach based on concordia stator mean current vector," *IEEE Transactions on Energy Conversion*, vol. 20, no. 3, pp. 512–519, 2005.

[127] N. M. Roscoe and M. D. Judd, "Harvesting energy from magnetic fields to power condition monitoring sensors," *IEEE Sensors Journal*, vol. 13, no. 6, pp. 2263–2270, 2013.

[128] S. Pöyhönen, M. Negrea, P. Jover, A. Arkkio, and H. Hyötyniemi, "Numerical magnetic field analysis and signal processing for fault diagnostics of electrical machines," *COMPEL - The International Journal for Computation and Mathematics in Electrical and Electronic Engineering*, vol. 22, no. 4, pp. 969–981, 2003.

[129] J. A. Farooq, A. Djerdir, and A. Miraoui, "Analytical modeling approach to detect magnet defects in permanent-magnet brushless motors," *IEEE Transactions on Magnetics*, vol. 44, no. 12, pp. 4599–4604, 2008.

[130] S. Feng, B. Fan, J. Mao, and Y. Xie, "Prediction on wear of a spur gearbox by on-line wear debris concentration monitoring," *Wear*, vol. 336-337, pp. 1–8, 2015.

[131] A. Agoston, C. Ötsch, and B. Jakoby, "Viscosity sensors for engine oil condition monitoring-Application and interpretation of results," *Sensors and Actuators A: Physical*, vol. 121, no. 2, pp. 327–332, 2005.

[132] S. Kumar, P. S. Mukherjee, and N. M. Mishra, "Online condition monitoring of engine oil," *Industrial Lubrication and Tribology*, vol. 57, no. 6, pp. 260–267, 2005.

[133] S. M. Schultheis, C. A. Lickteig, and R. Parchewsky, "Reciprocating compressor condition monitoring," in *Proceedings of the 36th Turbomachinery Symposium*, San Antonio, TX, USA, June 2007.

[134] M. Elhaj, M. Almrabet, M. Rgeai, and I. Ehtiwesh, "A combined practical approach to condition monitoring of reciprocating compressors using IAS and dynamic pressure," *World Academy of Science, Engineering and Technology*, vol. 63, no. 39, pp. 186–192, 2010.

[135] Y. Gao, Q. Zhang, and X. Kong, "Wavelet–based pressure analysis for hydraulic pump health diagnosis," *Transactions of the ASAE*, vol. 46, no. 4, p. 969, 2003.

[136] H. Sun, R. Xiao, W. Liu, and F. Wang, "Analysis of S characteristics and pressure pulsations in a pump-turbine with misaligned guide vanes," *Journal of Fluids Engineering*, vol. 135, no. 5, Article ID 051101, 2013.

[137] E. Mucchi, G. Dalpiaz, and A. Fernàndez del Rincòn, "Elastodynamic analysis of a gear pump. part I: pressure distribution and gear eccentricity," *Mechanical Systems and Signal Processing*, vol. 24, no. 7, pp. 2160–2179, 2010.

[138] E. Y. Kim, A. C. C. Tan, J. Mathew, and B. S. Yang, "Condition monitoring of low speed bearings: a comparative study of the ultrasound technique versus vibration measurements," *Australian Journal of Mechanical Engineering*, vol. 5, no. 2, pp. 177–189, 2008.

[139] J. Zhang, B. W. Drinkwater, and R. S. Dwyer-Joyce, "Monitoring of lubricant film failure in a ball bearing using ultrasound," *Journal of Tribology*, vol. 128, no. 3, pp. 612–618, 2006.

[140] N. H. Abu-Zahra and G. Yu, "Gradual wear monitoring of turning inserts using wavelet analysis of ultrasound waves," *International Journal of Machine Tools and Manufacture*, vol. 43, no. 4, pp. 337–343, 2003.

[141] P. A. Delgado-Arredondo, D. Morinigo-Sotelo, R. A. Osornio-Rios, J. G. Avina-Cervantes, H. Rostro-Gonzalez, and R. d. J. Romero-Troncoso, "Methodology for fault detection in induction motors via sound and vibration signals," *Mechanical Systems and Signal Processing*, vol. 83, pp. 568–589, 2017.

[142] B. Van Hecke, J. Yoon, and D. He, "Low speed bearing fault diagnosis using acoustic emission sensors," *Applied Acoustics*, vol. 105, pp. 35–44, 2016.

[143] X. Dong, G. Li, Y. Jia, B. Li, and K. He, "Non-iterative denoising algorithm for mechanical vibration signal using spectral graph wavelet transform and detrended fluctuation analysis," *Mechanical Systems and Signal Processing*, vol. 149, Article ID 107202.

[144] S. E. Pandarakone, Y. Mizuno, and H. Nakamura, "A comparative study between machine learning algorithm and artificial intelligence neural network in detecting minor bearing fault of induction motors," *Energies*, vol. 12, no. 11, p. 2105, 2019.

[145] J.-H. Zhong, P. K. Wong, and Z.-X. Yang, "Fault diagnosis of rotating machinery based on multiple probabilistic classifiers," *Mechanical Systems and Signal Processing*, vol. 108, pp. 99–114, 2018.

[146] S. Martin-del-Campo and F. Sandin, "Online feature learning for condition monitoring of rotating machinery," *Engineering Applications of Artificial Intelligence*, vol. 64, pp. 187–196, 2017.

[147] S. Pan, T. Han, A. C. C. Tan, and T. R. Lin, "fault diagnosis system of induction motors based on multiscale entropy and support vector machine with mutual information algorithm," *Shock and Vibration*, vol. 2016, pp. 1–12, 2016.

[148] P. Konar and P. Chattopadhyay, "Multi-class fault diagnosis of induction motor using Hilbert and Wavelet Transform," *Applied Soft Computing*, vol. 30, pp. 341–352, 2015.

[149] J. D. Martínez-Morales, E. R. Palacios-Hernández, and D. U. Campos-Delgado, "Multiple-fault diagnosis in induction motors through support vector machine classification at variable operating conditions," *Electrical Engineering*, vol. 100, no. 1, pp. 59–73, 2016.

[150] P. Gangsar and R. Tiwari, "Comparative investigation of vibration and current monitoring for prediction of mechanical and electrical faults in induction motor based on multiclass-support vector machine algorithms," *Mechanical Systems and Signal Processing*, vol. 94, pp. 464–481, 2017.

[151] P. Tamilselvan and P. Wang, "Failure diagnosis using deep belief learning based health state classification," *Reliability Engineering & System Safety*, vol. 115, pp. 124–135, 2013.

[152] G. Helbing and M. Ritter, "Deep Learning for fault detection in wind turbines," *Renewable and Sustainable Energy Reviews*, vol. 98, pp. 189–198, 2018.

[153] P. Cao, S. Zhang, and J. Tang, "Preprocessing-free gear fault diagnosis using small datasets with deep convolutional neural network-based transfer learning," *IEEE Access*, vol. 6, pp. 26241–26253, 2018.

[154] S.-Y. Shao, W.-J. Sun, R.-Q. Yan, P. Wang, and R. X. Gao, "A deep learning approach for fault diagnosis of induction motors in manufacturing," *Chinese Journal of Mechanical Engineering*, vol. 30, no. 6, pp. 1347–1356, 2017.

[155] W. Sun, S. Shao, R. Zhao, R. Yan, X. Zhang, and X. Chen, "A sparse auto-encoder-based deep neural network approach for induction motor faults classification," *Measurement*, vol. 89, pp. 171–178, 2016.

[156] O. Janssens, R. Van de Walle, M. Loccufier, and S. Van Hoecke, "Deep learning for infrared thermal image based machine health monitoring," *IEEE/ASME Transactions on Mechatronics*, vol. 23, no. 1, pp. 151–159, 2018.

[157] F. Cipollini, L. Oneto, A. Coraddu, and S. Savio, "Unsupervised deep learning for induction motor bearings monitoring," *Data-Enabled Discovery and Applications*, vol. 3, no. 1, p. 1, 2019.

[158] S. S. Udmale, S. K. Singh, and S. G. Bhirud, "A bearing data analysis based on kurtogram and deep learning sequence models," *Measurement*, vol. 145, pp. 665–677, 2019.

[159] R. Zhang, H. Tao, L. Wu, and Y. Guan, "Transfer learning with neural networks for bearing fault diagnosis in changing working conditions," *IEEE Access*, vol. 5, pp. 14347–14357, 2017.

[160] M. J. Hasan, M. M. M. Islam, and J.-M. Kim, "Acoustic spectral imaging and transfer learning for reliable bearing fault diagnosis under variable speed conditions," *Measurement*, vol. 138, pp. 620–631, 2019.

[161] Z. Wu, H. Jiang, K. Zhao, and X. Li, "An adaptive deep transfer learning method for bearing fault diagnosis," *Measurement*, vol. 151, p. 107227, 2020.

[162] X. Wang, C. Shen, M. Xia, D. Wang, J. Zhu, and Z. Zhu, "Multi-scale deep intra-class transfer learning for bearing fault diagnosis," *Reliability Engineering & System Safety Reliability Engineering & System Safety*, vol. 202, Article ID 107050, 2020.

[163] M. He and D. He, "A new hybrid deep signal processing approach for bearing fault diagnosis using vibration signals," *Neurocomputing*, vol. 396, pp. 542–555, 2020.

[164] A. Cubillo, S. Perinpanayagam, and M. Esperon-Miguez, "A review of physics-based models in prognostics: application to gears and bearings of rotating machinery," *Advances in Mechanical Engineering*, vol. 8, no. 8, Article ID 168781401666466, 2016.

[165] R. B. Randall and J. Antoni, "Rolling element bearing diagnostics-A tutorial," *Mechanical Systems and Signal Processing*, vol. 25, no. 2, pp. 485–520, 2011.

[166] D. Abboud, J. Antoni, S. Sieg-Zieba, and M. Eltabach, "Envelope analysis of rotating machine vibrations in variable speed conditions: A comprehensive treatment," *Mechanical Systems and Signal Processing*, vol. 84, pp. 200–226, 2017.

[167] D. Dou and S. Zhou, "Comparison of four direct classification methods for intelligent fault diagnosis of rotating machinery," *Applied Soft Computing*, vol. 46, pp. 459–468, 2016.

[168] S. Hong, Z. Zhou, E. Zio, and W. Wang, "An adaptive method for health trend prediction of rotating bearings," *Digital Signal Processing*, vol. 35, pp. 117–123, 2014.

[169] M. G. Don and F. Khan, "Dynamic process fault detection and diagnosis based on a combined approach of hidden Markov and Bayesian network model," *Chemical Engineering Science*, vol. 201, pp. 82–96, 2019.

[170] M. Y. Asr, M. M. Ettefagh, R. Hassannejad, and S. N. Razavi, "Diagnosis of combined faults in rotary machinery by non-naive bayesian approach," *Mechanical Systems and Signal Processing*, vol. 85, pp. 56–70, 2017.

[171] I. Ben-Gal, "Bayesian networks," *Encyclopedia of Statistics in Quality and Reliability*, vol. 1, 2008.

[172] S. Nie, M. Zheng, and Q. Ji, "The deep regression Bayesian network and its applications: probabilistic deep learning for computer vision," *IEEE Signal Processing Magazine*, vol. 35, no. 1, pp. 101–111, 2018.

[173] R. Agrahari, "Applications of Bayesian network models in predicting types of hematological malignancies," *Scientific Reports*, vol. 8, no. 1, p. 6951, 2018.

[174] Z. Wang, Z. Wang, X. Gu, S. He, and Z. Yan, "Feature selection based on Bayesian network for chiller fault diagnosis from the perspective of field applications," *Applied Thermal Engineering*, vol. 129, pp. 674–683, 2018.

[175] H. Kumar, V. Sugumaran, and M. Amarnath, "Fault diagnosis of bearings through sound signal using statistical features and Bayes classifier," *Journal of Vibration Engineering & Technologies*, vol. 4, no. 2, pp. 87–96, 2016.

[176] X. Zhang, Y. Liang, J. Zhou, and Y. zang, "A novel bearing fault diagnosis model integrated permutation entropy, ensemble empirical mode decomposition and optimized SVM," *Measurement*, vol. 69, pp. 164–179, 2015.

[177] F. Chen, B. Tang, T. Song, and L. Li, "Multi-fault diagnosis study on roller bearing based on multi-kernel support vector machine with chaotic particle swarm optimization," *Measurement*, vol. 47, pp. 576–590, 2014.

[178] S. Suthaharan, "Support vector machine," in *Machine Learning Models and Algorithms for Big Data Classification*, pp. 207–235, Springer, Berlin, Germany, 2016.

[179] P. Konar and P. Chattopadhyay, "Bearing fault detection of induction motor using wavelet and Support Vector Machines (SVMs)," *Applied Soft Computing*, vol. 11, no. 6, pp. 4203–4211, 2011.

[180] M. Singh and A. G. Shaik, "Faulty bearing detection, classification and location in a three-phase induction motor based on Stockwell transform and support vector machine," *Measurement*, vol. 131, pp. 524–533, 2019.

[181] Z. Su, B. Tang, Z. Liu, and Y. Qin, "Multi-fault diagnosis for rotating machinery based on orthogonal supervised linear local tangent space alignment and least square support vector machine," *Neurocomputing*, vol. 157, pp. 208–222, 2015.

[182] S. Liu, Y. Hu, C. Li, H. Lu, and H. Zhang, "Machinery condition prediction based on wavelet and support vector machine," *Journal of Intelligent Manufacturing*, vol. 28, no. 4, pp. 1045–1055, 2015.

[183] Y. Li, M. Xu, R. Wang, and W. Huang, "A fault diagnosis scheme for rolling bearing based on local mean decomposition and improved multiscale fuzzy entropy," *Journal of Sound and Vibration*, vol. 360, pp. 277–299, 2016.

[184] Y. Li, M. Xu, H. Zhao, and W. Huang, "Hierarchical fuzzy entropy and improved support vector machine based binary tree approach for rolling bearing fault diagnosis," *Mechanism and Machine Theory*, vol. 98, pp. 114–132, 2016.

[185] P. A. Schmid, A. Steinecker, J. Sun, and H. F. Knapp, "Neural networks and advanced algorithms for intelligent monitoring in industry," in *Electronic Components and Systems for Automotive Applications*, pp. 173–183, Springer, Berlin, Germany, 2019.

[186] Z. Zhang, Y. Wang, and K. Wang, "Fault diagnosis and prognosis using wavelet packet decomposition, Fourier transform and artificial neural network," *Journal of Intelligent Manufacturing*, vol. 24, no. 6, pp. 1213–1227, 2013.

[187] Z. Geng, Y. Zhang, C. Li, Y. Han, Y. Cui, and B. Yu, "Energy optimization and prediction modeling of petrochemical industries: An improved convolutional neural network based on cross-feature," *Energy*, vol. 194, p. 116851, 2020.

[188] D.-K. Bui, T. N. Nguyen, T. D. Ngo, and H. Nguyen-Xuan, "An artificial neural network (ANN) expert system enhanced with the electromagnetism-based firefly algorithm (EFA) for predicting the energy consumption in buildings," *Energy*, vol. 190, Article ID 116370, 2020.

[189] Z. Huo, Y. Zhang, R. Sath, and L. Shu, "Self-adaptive fault diagnosis of roller bearings using infrared thermal images," in *Proceeedings of the 43rd Annual Conference of the IEEE Industrial Electronics Society (IECON)*, Beijing, China, 2017.

[190] A. V. Joshi, "Perceptron and neural networks," in *Machine Learning and Artificial Intelligence*, pp. 43–51, Springer, Berlin, Germany, 2020.

[191] J. Ben Ali, N. Fnaiech, L. Saidi, B. Chebel-Morello, and F. Fnaiech, "Application of empirical mode decomposition and artificial neural network for automatic bearing fault diagnosis based on vibration signals," *Applied Acoustics*, vol. 89, pp. 16–27, 2015.

[192] M. Xia, T. Li, L. Xu, L. Liu, and C. W. de Silva, "fault diagnosis for rotating machinery using multiple sensors and convolutional neural networks," *IEEE/ASME Transactions on Mechatronics*, vol. 23, no. 1, pp. 101–110, 2018.

[193] P. Agrawal and P. Jayaswal, "Diagnosis and classifications of bearing faults using artificial neural network and support vector machine," *Journal of The Institution of Engineers (India): Series C*, vol. 101, no. 1, pp. 61–72, 2020.

[194] W. Li, Z. Zhu, F. Jiang, G. Zhou, and G. Chen, "Fault diagnosis of rotating machinery with a novel statistical feature extraction and evaluation method," *Mechanical Systems and Signal Processing*, vol. 50-51, pp. 414–426, 2015.

[195] P. K. Kankar, S. C. Sharma, and S. P. Harsha, "Fault diagnosis of ball bearings using machine learning methods," *Expert Systems with Applications*, vol. 38, no. 3, pp. 1876–1886, 2011.

[196] V. Vakharia, V. Gupta, and P. Kankar, "A multiscale permutation entropy based approach to select wavelet for fault diagnosis of ball bearings," *Journal of Vibration and Control*, vol. 21, no. 16, pp. 3123–3131, 2015.

[197] K. Gowthami and L. Kalaivani, "Fault classification of induction motor bearing using adaptive neuro fuzzy inference system," in *Proceedings of the Fifth International Conference on Electrical Energy Systems (ICEES)*, pp. 1–6, Beijing, China, 2019.

[198] L. Jie, W. Wang, and F. Golnaraghi, "An enhanced diagnostic scheme for bearing condition monitoring," *IEEE Transactions on Instrumentation and Measurement*, vol. 59, no. 2, pp. 309–321, 2010.

[199] S. Khan and T. Yairi, "A review on the application of deep learning in system health management," *Mechanical Systems and Signal Processing*, vol. 107, pp. 241–265, 2018.

[200] R. Zhao, R. Yan, Z. Chen, K. Mao, P. Wang, and R. X. Gao, "Deep learning and its applications to machine health monitoring," *Mechanical Systems and Signal Processing*, vol. 115, pp. 213–237, 2019.

[201] M. Bach-Andersen, B. Rømer-Odgaard, and O. Winther, "Deep learning for automated drivetrain fault detection," *Wind Energy*, vol. 21, no. 1, pp. 29–41, 2018.

[202] D.-T. Hoang and H.-J. Kang, "A survey on Deep Learning based bearing fault diagnosis," *Neurocomputing*, vol. 335, pp. 327–335, 2019.

[203] W. Dai, Z. Mo, C. Luo, J. Jiang, H. Zhang, and Q. Miao, "Fault diagnosis of rotating machinery based on deep reinforcement learning and reciprocal of smoothness index," *IEEE Sensors Journal*, vol. 20, no. 15, pp. 8307–8315, 2020.

[204] M. Gan, C. Wang, and C. Zhu, "Construction of hierarchical diagnosis network based on deep learning and its application in the fault pattern recognition of rolling element bearings," *Mechanical Systems and Signal Processing*, vol. 72-73, pp. 92–104, 2016.

[205] H. Shao, H. Jiang, F. Wang, and H. Zhao, "An enhancement deep feature fusion method for rotating machinery fault diagnosis," *Knowledge-Based Systems*, vol. 119, pp. 200–220, 2017.

[206] H. Shao, H. Jiang, H. Zhao, and F. Wang, "A novel deep autoencoder feature learning method for rotating machinery fault diagnosis," *Mechanical Systems and Signal Processing*, vol. 95, pp. 187–204, 2017.

[207] C. Lu, Z.-Y. Wang, W.-L. Qin, and J. Ma, "Fault diagnosis of rotary machinery components using a stacked denoising autoencoder-based health state identification," *Signal Processing*, vol. 130, pp. 377–388, 2017.

[208] M. He and D. He, "Deep learning based approach for bearing fault diagnosis," *IEEE Transactions on Industry Applications*, vol. 53, no. 3, pp. 3057–3065, 2017.

[209] X. Guo, L. Chen, and C. Shen, "Hierarchical adaptive deep convolution neural network and its application to bearing fault diagnosis," *Measurement*, vol. 93, pp. 490–502, 2016.

[210] M. Sohaib, C.-H. Kim, and J.-M. Kim, "A hybrid feature model and deep-learning-based bearing fault diagnosis," *Sensors*, vol. 17, no. 12, p. 2876, 2017.

[211] C. Li, R.-V. Sánchez, G. Zurita, M. Cerrada, and D. Cabrera, "fault diagnosis for rotating machinery using vibration measurement deep statistical feature learning," *Sensors*, vol. 16, no. 6, p. 895, 2016.

[212] F. Jia, Y. Lei, J. Lin, X. Zhou, and N. Lu, "Deep neural networks: a promising tool for fault characteristic mining and intelligent diagnosis of rotating machinery with massive data," *Mechanical Systems and Signal Processing*, vol. 72-73, pp. 303–315, 2016.

[213] H. Shao, H. Jiang, H. Zhang, W. Duan, T. Liang, and S. Wu, "Rolling bearing fault feature learning using improved convolutional deep belief network with compressed sensing," *Mechanical Systems and Signal Processing*, vol. 100, pp. 743–765, 2018.

[214] C. Li, R.-V. Sanchez, G. Zurita, M. Cerrada, D. Cabrera, and R. E. Vásquez, "Multimodal deep support vector classification with homologous features and its application to gearbox fault diagnosis," *Neurocomputing*, vol. 168, pp. 119–127, 2015.

[215] O. Janssens, V. Slavkovikj, B. Vervisch et al., "Convolutional neural network based fault detection for rotating machinery," *Journal of Sound and Vibration*, vol. 377, pp. 331–345, 2016.

[216] Z. Chen, S. Deng, X. Chen, C. Li, R.-V. Sanchez, and H. Qin, "Deep neural networks-based rolling bearing fault diagnosis," *Microelectronics Reliability*, vol. 75, pp. 327–333, 2017.

[217] D. Verstraete, A. Ferrada, E. L. Droguett, V. Meruane, and M. Modarres, "Deep learning enabled fault diagnosis using time-frequency image analysis of rolling element bearings," *Shock and Vibration*, vol. 2017, pp. 1–17, Article ID 5067651, 2017.

[218] W. Zhang, X. Li, and Q. Ding, "Deep residual learning-based fault diagnosis method for rotating machinery," *ISA Transactions*, vol. 95, p. 295, 2019.

[219] L. Wen, X. Li, L. Gao, and Y. Zhang, "A new convolutional neural network-based data-driven fault diagnosis method," *IEEE Transactions on Industrial Electronics*, vol. 65, no. 7, pp. 5990–5998, 2018.

[220] J. Zheng, J. Zhu, G. Chen, Z. Song, and Z. Ge, "Dynamic Bayesian network for robust latent variable modeling and fault classification," *Engineering Applications of Artificial Intelligence*, vol. 89, p. 103475, 2020.

[221] C. Duan, V. Makis, and C. Deng, "A two-level Bayesian early fault detection for mechanical equipment subject to dependent failure modes," *Reliability Engineering & System Safety*, vol. 193, p. 106676, 2020.

[222] B. Song, S. Tan, H. Shi, and B. Zhao, "Fault detection and diagnosis via standardized k nearest neighbor for multimode process," *Journal of the Taiwan Institute of Chemical Engineers*, vol. 106, pp. 1–8, 2020.

[223] S. Jalali, H. Ghandi, and M. Motamedi, "Intelligent condition monitoring of ball bearings faults by combination of genetic algorithm and support vector machines," *Journal of Nondestructive Evaluation*, vol. 39, no. 1, pp. 1–12, 2020.

[224] A. Ghosh, G.-N. Wang, and J. Lee, "A novel automata and neural network based fault diagnosis system for PLC controlled manufacturing systems," *Computers & Industrial Engineering*, vol. 139, Article ID 106188, 2020.

[225] A. S. Ahuja, D. S. Ramteke, and A. Parey, "Vibration-based fault diagnosis of a bevel and spur gearbox using continuous wavelet transform and adaptive neuro-fuzzy inference system," in *Soft Computing in Condition Monitoring and Diagnostics of Electrical and Mechanical Systems*, pp. 473–496, Springer, Berlin, Germany, 2020.

[226] H. A. Saeed, H. Wang, M. Peng, A. Hussain, and A. Nawaz, "Online fault monitoring based on deep neural network & sliding window technique," *Progress in Nuclear Energy*, vol. 121, Article ID 103236, 2020.

[227] L. Chen, Z. Zhang, J. Cao, and X. Wang, "A novel method of combining nonlinear frequency spectrum and deep learning for complex system fault diagnosis," *Measurement*, vol. 151, Article ID 107190, 2020.

[228] S. Zhang, S. Zhang, B. Wang, and T. G. Habetler, "Deep learning algorithms for bearing fault diagnostics-A comprehensive review," *IEEE Access*, vol. 8, pp. 29857–29881, 2020.

[229] R. Liu, B. Yang, E. Zio, and X. Chen, "Artificial intelligence for fault diagnosis of rotating machinery: A review," *Mechanical Systems and Signal Processing*, vol. 108, pp. 33–47, 2018.

[230] Y. Lei, N. Li, L. Guo, N. Li, T. Yan, and J. Lin, "Machinery health prognostics: a systematic review from data acquisition to RUL prediction," *Mechanical Systems and Signal Processing*, vol. 104, pp. 799–834, 2018.

[231] H. Henao, G.-A. Capolino, M. Fernandez-Cabanas et al., "Trends in fault diagnosis for electrical machines: a review of diagnostic techniques," *IEEE Industrial Electronics Magazine*, vol. 8, no. 2, pp. 31–42, 2014.

[232] A. M. Alshorman, O. Alshorman, M. Irfan, A. Glowacz, F. Muhammad, and W. Caesarendra, "Fuzzy-based fault-Tolerant control for omnidirectional mobile robot," *Machines*, vol. 8, no. 3, p. 55, 2020.

[233] O. AlShorman, B. AlShorman, M. Alkhassaweneh, and F. Alkahtani, "A review of internet of medical things (IoMT) – based remote health monitoring through wearable sensors: A case study for diabetic patients," *Indonesian Journal of Electrical Engineering and Computer Science*, vol. 20, no. 1, 2020.

[234] O. AlShorman, B. Alshorman, and F. Alkahtani, "A review of wearable sensors based monitoring with daily physical activity to manage type 2 diabetes," *International Journal of*

Electrical and Computer Engineering (IJECE), vol. 11, no. 1, 2021.

[235] O. AlShorman, B. Alshorman, and M. Masadeh, "A review of physical human activity recognition chain using sensors," *Indonesian Journal of Electrical Engineering and Informatics (IJEEI)*, vol. 8, no. No 3, 2020.

Hindawi
Shock and Vibration
Volume 2020, Article ID 8886066, 17 pages
https://doi.org/10.1155/2020/8886066

Research Article

Vibration Response of the Planetary Gears with a Float Sun Gear and Influences of the Dynamic Parameters

Yinghui Liu,[1] Dong Zhen ,[1] Huibo Zhang,[1] Hao Zhang,[1] Zhanqun Shi,[1] and Fengshou Gu[2]

[1]*Tianjin Key Laboratory of Power Transmission and Safety Technology for New Energy Vehicles, School of Mechanical Engineering, Hebei University of Technology, Tianjin 300401, China*
[2]*Centre for Efficiency and Performance Engineering, University of Huddersfield, Huddersfield HD1 3DH, UK*

Correspondence should be addressed to Dong Zhen; d.zhen@hebut.edu.cn

Received 9 May 2020; Revised 15 June 2020; Accepted 1 July 2020; Published 4 August 2020

Academic Editor: Muhammad Irfan

Planetary gearboxes are widely used in mechanical transmission systems due to their large transmission ratio and high transmission efficiency. In a planetary gearbox, the sun gear is usually set to float to balance the sharing of loads among planet gears. However, this floating set will result in the variation of pressure angle, overlap ratio, and meshing phase in the meshing progress and when gear faults occur, the variation will be enlarged. In the previous studies, these parameters were reduced to constant. To study the influence of the dynamic parameters on the vibration response of planetary gearboxes under different operating conditions, a new lumped-parameter model containing the time-varying pressure angle (TVPA), time-varying overlap ratio (TVOR), and time-varying meshing phase (TVMP) is established. Based on this model, the vibration response mechanism of the sun gear is analyzed. Moreover, the comparison with the previous model is made and the rule of phase modulation caused by these dynamic parameters is revealed. By comparing the dynamic responses under different loads and rotation speeds, the phase modulation is studied in detail. Finally, the sun gear fault is introduced, and the phase modulation is analyzed in different fault degrees. This study can provide theoretical reference for the condition monitoring and fault diagnosis of planetary gearbox based on vibration analysis.

1. Introduction

Nowadays, planetary gearbox is widely used in various mechanical systems, such as automobiles, helicopters, wind turbines, and robots for its advantages of large transmission ratio, high transmission efficiency, and compact structure [1]. Compared with the fixed shaft gearbox, planetary gearbox has more complex mechanical structure and gear movement, especially the time-varying vibration transfer paths, which leads to unnecessary modulation and asymmetric frequency sidebands in addition to a lot of noise in its vibration response [2–5]. Hence, for planetary gearboxes, the vibration suppression, noise reduction, and fault diagnosis become extremely difficult [6]. To effectively solve these problems, it is necessary to build a planetary gearbox model and study the mechanism of vibration.

With the development of high-speed and heavy power rotating machinery, numerous researches on gear material selection [7], gear contact analysis [8], and gear models, including uncertain model [9–11] and deterministic model, have been conducted for the studies of vibration mechanism. In 1994, Kahraman [12] proposed a nonlinear dynamic model. Later, Inalpolat and Kahraman [13, 14] introduced manufacturing error and time-varying meshing stiffness into the model and studied the modulation sidebands of planetary gears. Zhai et al. [15] considered the installation error of the carrier and analyzed the dynamic characteristics in different error directions. Lin et al. [16] and Parker et al. [17] studied the natural frequencies and vibration modes and gave the mathematical expression for each mode. Combined with FEM, Concli et al. [18] proposed a lumped-parameter model with 18 degrees of freedom to study the frequency characteristics of the planetary gear system. Noticing that the multisource vibration components in the vibration signals were affected by the vibration transfer paths, a dynamic model containing time-varying vibration transfer paths was

developed [19–21]. But all of these models are single state. In light load transmission, teeth separation and back-side tooth contact may occur. Therefore, Yang et al. [22] and Shi et al. [23] proposed a two-state model by introducing gear backlash to research meshing state and vibration characteristics of the system. Zhang et al. [24] proposed a dynamic model with a multiclearance coupling to analyze the vibration characteristics. Zhao et al. [25] developed a nonlinear dynamic model containing time-varying meshing stiffness, damping, static transmission error, and backlash. In a planetary gearbox, the sun gear is usually set to float to balance the load sharing among the planetary gears. Singh [26] provided a physical explanation for the basic mechanism causing the unequal load sharing phenomenon in both floating and nonfloating systems. Kahraman [12] predicted the dynamic load sharing factor and analyzed the influence of manufacturing errors, assembly changes, and key design parameters on it. When gear failure occurs, the vibration response of the planetary gearbox will also change. Li et al. [27] analyzed the frequency components of planetary gearbox in the healthy and fault states and explained the asymmetry of frequency sidebands. Parra and Vicuña [28] studied the frequency contents of planetary gearbox vibration signal via comparing phenomenological model with lumped-parameter model under nonfault and different fault conditions. Feng and Zuo [29] added the gear fault into the model to analyze the amplitude modulation and frequency modulation spectrum characteristics of the vibration signal. For early fault detection, Liu et al. [30] proposed a resultant vibration signal model and analyzed the faulty features of a signal stage planetary gearbox under nonstationary load conditions. Chen and Shao [31] analyzed the influence of tooth root crack at different positions and inclination angles on the dynamic response of the planetary gear system. Parker et al. [32,33] pointed out that the meshing phase had an important influence on the static and dynamic response of planetary gearbox and gave the meshing phase relationship among planet gears, sun gear, and ring gear. Later, Peng et al. [34, 35] applied meshing phase information to diagnose fault of planetary gearbox.

However, due to the sun gear floating set, bearing elastic deformation, and gear faults, the pressure angle and overlap ratio of the meshing gears will continually change in the operating process, and these variations are rarely considered in the previous established model. To study the influence of time-varying pressure angle and overlap ratio on the vibration response, a dynamic model with a floating sun gear is established. In this model, the TVPA, TVOR, and TVMP were considered as well as the vibration transfer path and time-varying meshing stiffness. Based on this model, the vibration response mechanism of the sun gear is analyzed. And then by adding typical sun gear fault, the influences of the fault on TVPA, TVOR, TVMP, and dynamic response are investigated. By comparing with the previous model under different operating conditions, the phase modulation rule is also analyzed.

The rest of this paper is organized as follows. Section 2 establishes the dynamic model of the planetary gearbox. In Section 3, the variation rule and phase modulation rule of time-varying pressure angle and overlap ratio under different working conditions and different fault severity are analyzed based on the proposed dynamic model. And the conclusions are given in Section 4.

2. Dynamic Model of the Planetary Gearbox

2.1. Parameter Definition. The dynamic model of the gearbox in this study is a 2K-H planetary gear model which is displayed in Figure 1. This model contains a sun gear (s), n identical planet gears ($p_i, i = 1, 2, \ldots n$), a ring gear (r), and a carrier (c). The carrier serves as power input component and the sun gear is connected to the output shaft. All gear bodies are regarded as rigid and each element has one rotational and two translational degrees of freedom [12]. The coordinate systems used in this model are illustrated in Figure 2. The absolute coordinate system XOY is fixed on the ring gear, and the rotating frame of reference $\{u, v\}$ is attached to the carrier. The translational displacements of the sun gear, the carrier, and the ring gear are denoted as x_j, y_j, $j = s, c, r$, respectively. The translational displacements of planet gears are defined as τ_{p_i}, η_{p_i}, $i = 1, 2, \ldots n$, respectively. And all these translational displacements are measured with respect to the coordinate {u, v}. The basis coordinate $\{u, v\}$ rotates at the speed of Ω_c together with the carrier. And the rotational coordinate can be expressed as $u_j = r_j \times \theta_j$, $j = s, c, r, p_1, \ldots, p_n$, where r_j is the base circle radius of the sun gear, the ring gear, planet gears, and the radius of the circle passing through the planet centers for the carrier, and θ_j is the component rotation angle. In the model, circumferential planet locations are specified by the fixed angle φ_{p_i}, where φ_{p_i} is measured relative to rotating basis vector u so that $\varphi_{p_1} = 0$. The mass of elements is denoted as m_j, the inertia moment is I_j, and the number of teeth is z_j ($j = s, c, r, p_1, \ldots, p_n$). The supporting stiffness and damping of each element are denoted as k_j and c_j. The gears interact with each other through the mesh stiffness of k_{sp_i} and k_{rp_i} (k_{sp_i} for s-p_i mesh and k_{rp_i} for r-p_i mesh) and mesh damping of c_{sp_i} and c_{rp_i} (c_{sp_i} for s-p_i mesh and c_{rp_i} for r-p_i mesh) on the meshing action plane [12]. To simplify the model, the torsional stiffness of the shafts is neglected and the housing is regarded as rigid [25]. To reduce the asymmetry of load distribution on the planets, the sun gear is set to elastic float. The methodology followed in this study is displayed in the flow chart shown in Figure 3.

There will be contacting deflection on meshed teeth when the gearbox operates. The deflection of s-p mesh and r-p mesh can be expressed as [13]

$$\xi_{sp_i} = x_s \sin\psi_{sp_i} - y_s \cos\psi_{sp_i} - \tau_i \sin\alpha_{sp_i} - \eta_i \cos\alpha_{sp_i} + u_s + u_{p_i} - e_{sp_i}, \tag{1a}$$

$$\xi_{rp_i} = x_r \sin\psi_{rp_i} - y_r \cos\psi_{rp_i} + \tau_i \sin\alpha_{rp_i} - \eta_i \cos\alpha_{rp_i} + u_r - u_{p_i} - e_{rp_i}. \tag{1b}$$

The relative deflection along τ_i and η_i between the carrier and planet can be expressed as [13]

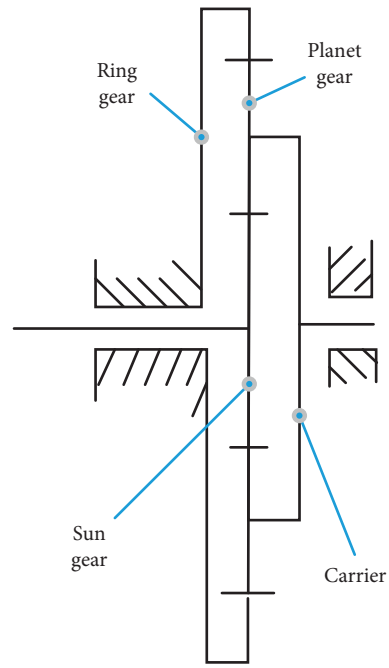

Figure 1: The structure diagram of a 2K-H planetary gear model.

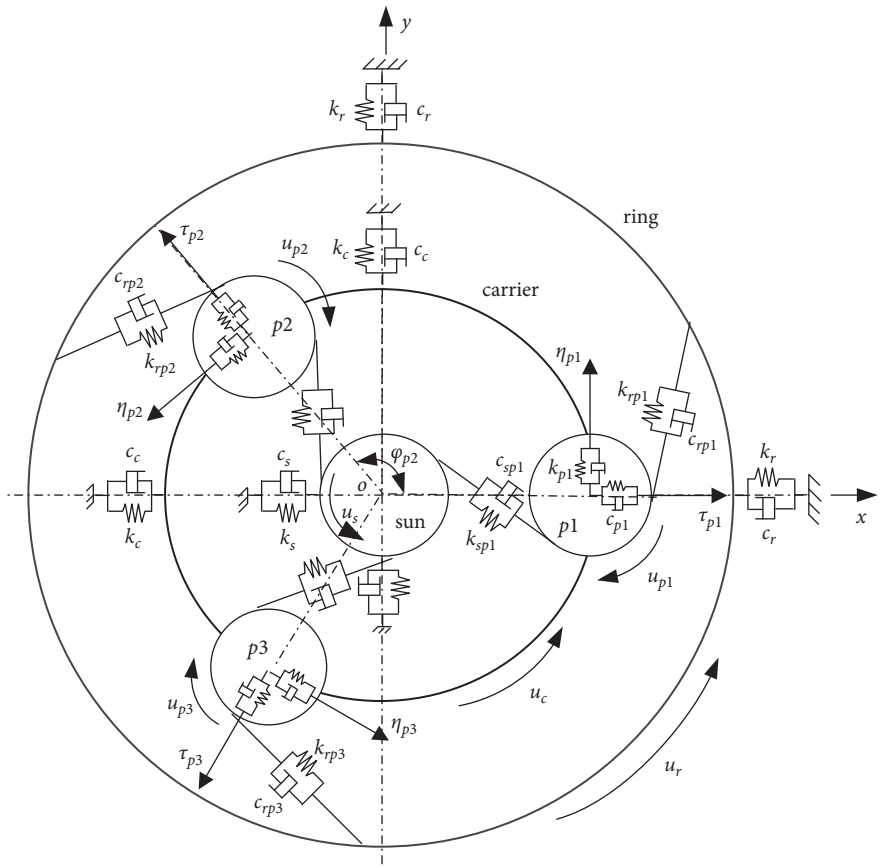

Figure 2: The dynamic model with three planet gears located at equal angle.

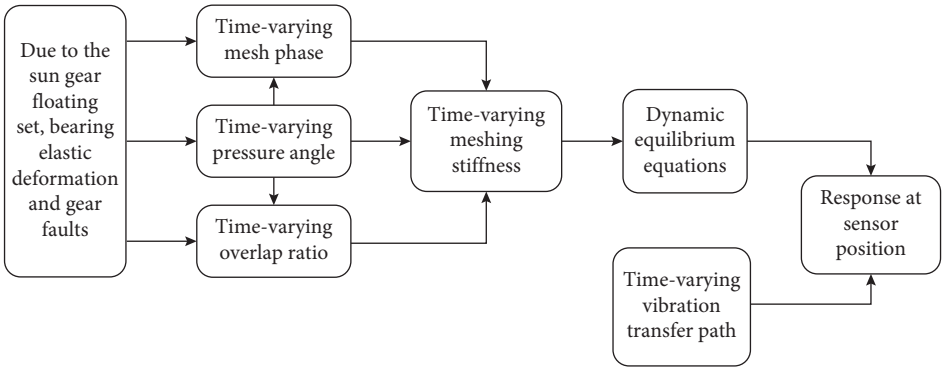

Figure 3: Flow chart of the methodology.

$$\xi_{cp_i x} = x_c \cos\varphi_{p_i} + y_c \sin\varphi_{p_i} - \tau_{p_i}, \tag{1c}$$

$$\xi_{cp_i y} = x_c \sin\varphi_{p_i} - y_c \cos\varphi_{p_i} - \eta_{p_i} + u_c. \tag{1d}$$

where e_{sp_i} and e_{rp_i} represent the transmission error of s-p_i and r-p_i, respectively. $\psi_{sp_i} = \alpha_{sp_i} + \varphi_{p_i}$ and $\psi_{rp_i} = \alpha_{rp_i} - \varphi_{p_i}$, with$\alpha_{sp_i}$ and α_{rp_i} denoting the pressure angle of s-p_i and r-p_i, respectively. Because of the vibration of the floating sun gear and planet gears during the rotation of the gearbox, the pressure angles α_{sp_i} and α_{rp_i} are time-varying. And the TVPA of s-p_i and r-p_i can be deduced from geometry as follows [36]:

$$\alpha_{sp_i} = \cos^{-1}\frac{r_s + r_{p_i}}{\sqrt{\left(x_s - x_{p_i}\right)^2 + \left(y_s - y_{p_i}\right)^2}}, \tag{2a}$$

$$\alpha_{rp_i} = \cos^{-1}\frac{r_r - r_{p_i}}{\sqrt{\left(x_r - x_{p_i}\right)^2 + \left(y_r - y_{p_i}\right)^2}}, \tag{2b}$$

where x_s and y_s represent the location of the sun gear center and x_r and y_r denote the location of the ring gear. All these coordinates are measured in the absolute coordinate.

$x_{p_i}$and $y_{p_i}$are the location of the planet gear center in the absolute coordinate which can be calculated as follows [36]:

$$x_{p_i} = x_c + \left(\tau_{p_i} + r_c\right)\cos\left(\theta + \varphi_{p_i}\right) - \eta_{p_i}\sin\left(\theta + \varphi_{p_i}\right), \tag{3a}$$

$$y_{p_i} = y_c + \left(\tau_{p_i} + r_c\right)\sin\left(\theta + \varphi_{p_i}\right) + \eta_{p_i}\cos\left(\theta + \varphi_{p_i}\right), \tag{3b}$$

where x_c and y_c are the position of the carrier in the absolute coordinate. τ_{p_i} and η_{p_i} are the location of p_i in the coordinate $\left\{\tau_{p_i}, \eta_{p_i}\right\}$. θ represents the rotation angle of the carrier.

And as shown in Figure 4, the variation of the meshing phase at the pitch point can be deduced as follows

$$\beta_{\text{start}} = \cos^{-1}\frac{r_{sd} \times \cos\alpha}{r_{as}}, \tag{4}$$

$$d_1 = \sqrt{r_{as}^2 - r_s^2} + \sqrt{r_{ap}^2 - r_p^2} - \left(r_s + r_p\right)\tan\alpha, \tag{5}$$

$$r_{\text{end}} = \sqrt{\left(\sqrt{r_{as}^2 - r_s^2} - d_1\right)^2 + r_s^2}, \tag{6}$$

$$\beta_{\text{end}} = \cos^{-1}\frac{r_{sd} \times \cos\alpha}{r_{\text{end}}}, \tag{7}$$

$$\gamma_{\text{evolve\_cycle}} = \left\{\tan\left(\beta_{\text{start}}\right) - \beta_{\text{start}}\right\} - \left\{\tan\left(\beta_{\text{start}}\right) - \beta_{\text{end}}\right\}, \tag{8}$$

$$\gamma_{\text{varyevolve\_}sp_i} = \left\{\tan\left(\alpha_{sp_i}\right) - \alpha_{sp_i}\right\} - \left\{\left(\tan\alpha\right) - \alpha\right\}, \tag{9a}$$

$$\gamma_{\text{varyevolve\_}rp_i} = \left\{\tan\left(\alpha_{rp_i}\right) - \alpha_{rp_i}\right\} - \left\{\left(\tan\alpha\right) - \alpha\right\}, \tag{9b}$$

$$\delta_{sp_i} = 2\pi\frac{\gamma_{\text{varyevolve\_}sp_i}}{\gamma_{\text{evolve\_cycle}}}, \tag{10a}$$

$$\delta_{rp_i} = 2\pi\frac{\gamma_{\text{varyevolve\_}rp_i}}{\gamma_{\text{evolve\_cycle}}}. \tag{10b}$$

Herein d_1 describes the length of the actual line of mesh. β_{start} stands for the pressure angle of addendum circle of the sun gear and β_{end} is the pressure angle for s-p_i at the mesh separation point as shown in Figure 4. r_{end} is the radius of the circle for the sun gear where the mesh separation point is located. $\gamma_{\text{evolve\_cycle}}$ denotes the evolving angle of the meshing tooth surface. $\gamma_{\text{varyevolve\_}sp_i}$ and $\gamma_{\text{varyevolve\_}rp_i}$ represent the variations of evolving angle relative to the evolving angle in the reference circle. δ_{sp_i} and $\delta_{rp_i}$are the variations of meshing phase of s-p_i and r-p_i relative to the standard meshing phase whose value is $2\pi f_m$ (f_m is the meshing frequency).

Therefore, the actual meshing phase is $(\delta_{sp_i} + 2\pi f_m)$ for s-p_i mesh, and the actual meshing phase is $(\delta_{rp_i} + 2\pi f_m)$ for r-p_i mesh. α is the standard pressure angle of reference circle. For the gear with a reference circle pressure angle of 20° is most widely used in standard gears, the value of α is set to 20°. For conjugate tooth profile, although their tooth profile shape is different in unit time, they change the same meshing phase.

For the mating gears, the meshing stiffness is not always the standard value in the progress of rotation. It changes periodically as shown in Figure 5. In one mesh cycle, when the mating gears are just coming into mesh,

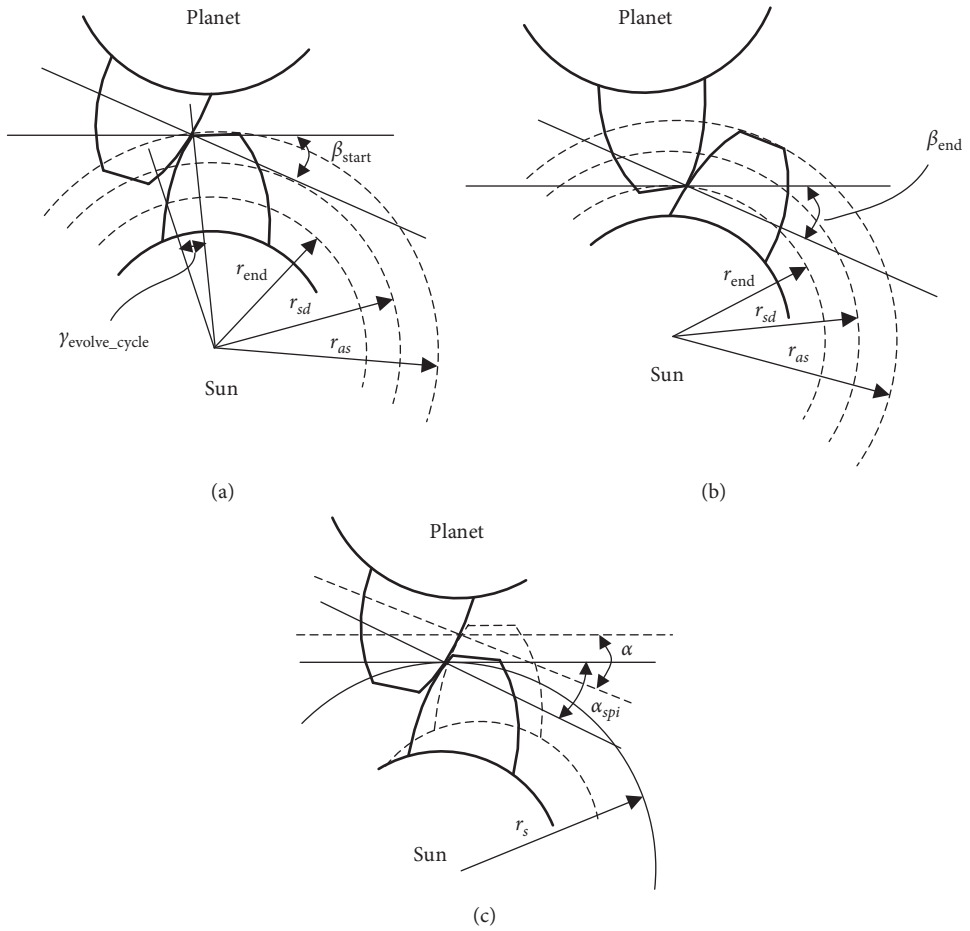

Figure 4: The meshing progress of the sun and planet gears. (a) The moment of meshing start. (b) The moment of meshing finish. (c) The meshing progress with the sun gear bounce.

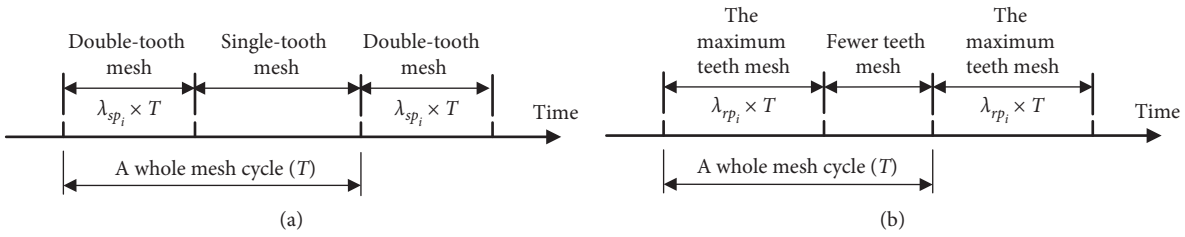

Figure 5: Meshing progress of one mesh cycle for the (a) external-external gear mesh and (b) internal-external gear mesh.

they are in the state of double-tooth mesh (for external-external mesh) or the most teeth mesh (for internal-external mesh) and become single-tooth mesh or the fewest teeth mesh near the pitch point. When the meshing teeth are going to be separated, they come into double-tooth mesh or the most teeth mesh again. The proportion of the double-tooth mesh or the most teeth mesh in a whole mesh cycle is determined by contact overlap ratio. However, the contact overlap ratio is also time-varying, which can be defined as follows [36]

$$\varepsilon_{sp_i} = \frac{\sqrt{r_{as}^2 - r_s^2} + \sqrt{r_{ap_i}^2 - r_{p_i}^2} - \left(r_s + r_p\right)\tan\alpha_{sp_i}}{p_b}, \tag{11a}$$

$$\varepsilon_{rp_i} = \frac{\sqrt{r_{ap_i}^2 - r_{p_i}^2} - \sqrt{r_{ar}^2 - r_r^2} + \left(r_s + r_p\right)\left(\sin\alpha_{rp_i}/\cos\alpha_{sp_i}\right)}{p_b}, \tag{11b}$$

where p_b is the base pitch. r_{as}, r_{ap_i}, and r_{ar} are the addendum radii of the sun gear, planet gear, and ring gear, respectively. α_{sp_i} and α_{rp_i} are the time-varying pressure angle of s-p_i and r-p_i.

The proportion of the mesh in which the maximum number of teeth participate can be expressed as follows:

$$\lambda_{sp_i} = \varepsilon_{sp_i} - \lfloor \varepsilon_{sp_i} \rfloor, \tag{12a}$$

$$\lambda_{rp_i} = \varepsilon_{rp_i} - \lfloor \varepsilon_{rp_i} \rfloor. \tag{12b}$$

In 12(a) and 12(b), $\lfloor \cdot \rfloor$ is defined as the rounding function.

Therefore, the time-varying meshing stiffness can be expressed as

$$k_{sp_i}(t) = \begin{cases} \Gamma, & \mathrm{mod}\left(\theta \times z_r + \varphi_{p_i} \times z_s + \delta_{sp_i}, 2\pi\right) \in \left[2\pi * \lambda_{sp_i}, 2\pi\left(\varepsilon_{sp_i} - \lambda_{sp_i}\right)\right], \\ 1.8\Gamma, & \mathrm{mod}\left(\theta \times z_r + \varphi_{p_i} \times z_s + \delta_{sp_i}, 2\pi\right) \in \left[0,\ 2\pi * \lambda_{sp_i}\right], \end{cases} \tag{13a}$$

$$k_{rp_i}(t) = \begin{cases} \Lambda, & \mathrm{mod}\left(\theta \times z_r + \varphi_{p_i} \times z_r + \rho + \delta_{rp_i}, 2\pi\right) \in \left[2\pi * \lambda_{rp_i}, 2\pi\left(\varepsilon_{rp_i} - \lambda_{rp_i}\right)\right], \\ 1.8\Lambda, & \mathrm{mod}\left(\theta \times z_r + \varphi_{p_i} \times z_r + \rho + \delta_{rp_i}, 2\pi\right) \in \left[0,\ 2\pi * \lambda_{rp_i}\right]. \end{cases} \tag{13b}$$

In 13(a) and 13(b), $\mathrm{mod}(\cdot)$ is defined as the remainder function. Γ is the meshing stiffness constant corresponding to the single-tooth mesh area of s-p_i and 1.8Γ is the internal-external mesh corresponding to the double-tooth mesh area of s-p_i. θ stands for the rotation angle of the carrier. Because of the vibration of gears and the TVPA, θ is not simply a linear function of time. In this model, it is calculated by numerical integral. φ_{p_i} is the circumferential location angle of the planet gear. A mesh cycle can be divided into single-tooth mesh and double-tooth mesh, and the whole mesh cycle is regarded as 2π radian. The ring gear is fixed, when the carrier rotates θ radian, the meshing phase variation of meshed gears is $\times z_r$, and the initial phase of meshed gears is $\varphi_{p_i} \times z_s$ which is caused by the location angle of planets. The initial meshing phase of s-p_1 is zero. δ_{sp_i} is the variation of meshing phase relative to the theoretical meshing phase whose value is $\theta \times z_r + \varphi_{p_i} \times z_s$ for s-p_i mesh and $\theta \times z_r + \varphi_{p_i} \times z_r + \rho$ for r-p_i mesh. ρ is the initial meshing phase difference of s-p_i and r-p_i. For different planet gears, ρ has the same value. Hence, when the carrier rotates θ radian, the meshing phase of s-p_i mesh is $\theta \times z_r + \varphi_{p_i} \times z_s + \delta_{sp_i}$, and the r-p_i mesh is $\theta \times z_r + \varphi_{p_i} \times z_r + \rho + \delta_{rp_i}$. As shown in Figure 6, the meshing stiffness mutates at the moment that the meshing teeth divorce. This is just because of the TVPA and the TVOR.

In the actual measurement, the sensor is generally arranged on the shell of the gearbox and its position is fixed. However, due to the rotation of the carrier, the meshing points of these gears periodically approach and then move away from the sensor, which will affect the energy of vibration signals collected by the sensor. Therefore, to simulate this pass-through effect of planetary gears, the Hanning window can be used as a weighting function which can be described as [13]

$$w = \frac{1}{2} - \frac{1}{2}\cos\left(\frac{2\pi n t}{T_c}\right). \tag{14}$$

For planet p_i, the weight function can be written as follows [13]:

$$w_{p_i} = \sigma_{p_i} \times w\left(t - \frac{\varphi_{p_i} T_c}{2\pi}\right), \tag{15}$$

$$\sigma_{p_i} = \begin{cases} 1, & \mathrm{mod}\left(t, T_c\right) \in \left[\frac{T_c}{n}(i-1), \frac{T_c}{n} i\right], \\ 0, & \mathrm{mod}\left(t, T_c\right) \notin \left[\frac{T_c}{n}(i-1), \frac{T_c}{n} i\right], \end{cases} \tag{16}$$

where T_c denotes the rotation cycle of the carrier and $\mathrm{mod}(\cdot)$ is defined as the remainder function.

The amplitude of vibration signal received by the sensor is calculated by the weight function when the meshing point is located in the action region. Outside the action area, the vibration energy of the meshing point has a great attenuation in the process of transferring to the sensor, so the vibration of the meshing point from the position outside the action region can be ignored. Therefore, the total acceleration measured by the sensor can be determined as follows [13]:

$$a = \sum_{i=1}^{n}\left(S_{sp_i} w_{p_i} a_{sp_i} + S_{rp_i} w_{p_i} a_{rp_i}\right), \tag{17}$$

where S_{sp_i} and S_{rp_i} are the attenuation coefficient of the energy during the transmission from the meshing point to the sensor. Because the transmission path for the external-external mesh is longer than that of the internal-external mesh, the value of S_{sp_i} should be smaller than S_{rp_i}. In this model, they are set as $S_{sp_i} = 0.4$ and $S_{rp_i} = 0.7$, respectively.

2.2. Dynamic Equations. Based on the above parameter definitions, the dynamic equilibrium equations can be listed out.

For the carrier, the dynamic equations can be expressed as

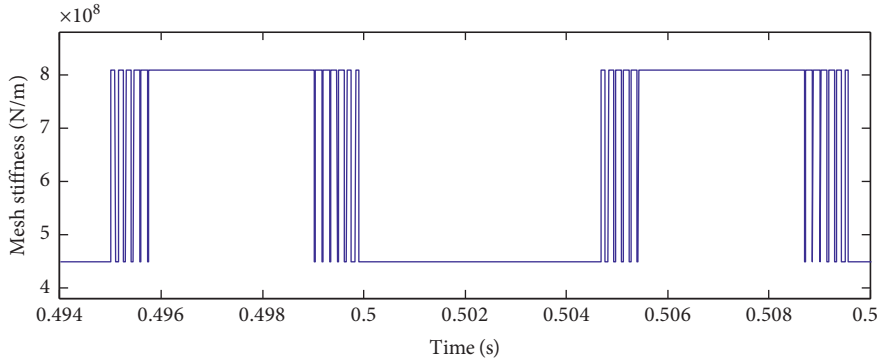

Figure 6: Meshing stiffness of s-p_1 mesh.

$$m_c\ddot{x}_c + k_c x_c + c_c\dot{x}_c - \sum_{i=1}^{n}\left(k_{p_i}\tau_{p_i} + c_{p_i}\dot{\tau}_{p_i}\right)\cos\varphi_{p_i} - \sum_{i=1}^{n}\left(k_{p_i}\eta_{p_i} + c_{p_i}\dot{\eta}_{p_i}\right)\sin\varphi_{p_i} = 0, \tag{18a}$$

$$m_c\ddot{y}_c + k_c y_c + c_c\dot{y}_c - \sum_{i=1}^{n}\left(k_{p_i}\tau_{p_i} + c_{p_i}\dot{\tau}_{p_i}\right)\sin\varphi_{p_i} + \sum_{i=1}^{n}\left(k_{p_i}\eta_{p_i} + c_{p_i}\dot{\eta}_{p_i}\right)\cos\varphi_{p_i} = 0, \tag{18b}$$

$$\frac{I_c}{r_c^2}\ddot{u}_c + \sum_{i=1}^{n}\left(k_{p_i}\eta_{p_i} + c_{p_i}\dot{\eta}_{p_i}\right) = \frac{T_c}{r_c}, \tag{18c}$$

where T_c is the input torque.

And the dynamic equations of the sun gear, ring gear, and planetary gears can be given referring to [37].

3. Numerical Simulation

3.1. Ideal Pressure Angle, Overlap Ratio, and Meshing Phase. The basic parameters used in this model are shown in Table 1. The input speed of the carrier is 100 rpm, and the input toque is 2500 Nm. The supporting stiffness of the sun gear, ring gear, carrier, and planet gears are set up as 5E7 N/m, 1E8 N/m, 1E8 N/m, and 2E9 N/m, respectively. The meshing stiffness constants Γ and Λ are 4.5E8 N/m and 5E8 N/m, respectively. All the gears are standard in this model. The transmission errors of s-p_i and r-p_i pairs are neglected. The dynamic differential equations of the model are solved by the numerical integration algorithm. Because the three planets can be seen as the same, the vibration responses of them are also the same except for the location angle difference. Therefore, in this study, we just consider the mesh of s-p_1.

Keeping the pressure angle, overlap ratio constant, and the meshing phase theoretical, the meshing stiffness of s-p_i and r-p_i is shown in Figure 7. Because the pressure angle and overlap ratio are constant, the cycle of meshing stiffness and phase difference φ between the sun gear and planet gear is also constant with the value of 120°. For the same planet p_i, the phase difference ρ between s-p_i and r-p_i is also constant. Figure 8 displays the meshing force of s-p_1, and it contains four times of carrier rotational frequency, meshing frequency, and its double frequency. Because of the planet location angle and the number of teeth of the ring gear, the spectrum is asymmetric and the amplitude of meshing frequency is suppressed to some extent [2].

3.2. Time-Varying Pressure Angle, Overlap Ratio, and Meshing Phase. When the TVPA, TVOR, and TVMP are introduced into the model, the dynamic response will change. Because of the floating set, the sun gear presents a triangular motion due to the meshing force of s-p_i which is shown in Figure 9, and the center track of the sun gear is shown in Figure 10. If the sun gear and planet gears have only rotational freedom and do not consider the effect of manufacturing errors, the deflection of ξ_{sp_1}, ξ_{sp_2}, and ξ_{sp_3} will have the same value during the rotation. However, the meshing stiffness of k_{sp_1}, k_{sp_2}, and k_{sp_3} is different. As a result, the sun gear is subject to unbalanced meshing forces Fi from the three planet gears which can be decomposed into Fi_x, Fi_y, and M as shown in Figure 9(a), and the resultant force is in the same direction as $F1$. Therefore, the sun gear will generate a translational motion trend along the direction of $F1$ to cause the resultant force of the meshing force $F1$, $F2$, and $F3$ to be zero. When the meshing phase of s-p_i changes φ radian, the force of the sun gear is shown in Figure 9(b) and the sun gear will generate a translational motion trend along the direction of $F2$. By the same token, when the meshing phase of s-p_i changes another φ radian, just like Figure 9(c), the sun gear will generate a translational motion trend along the direction of $F3$. This combination of translational and rotational motion of the sun gear presents a motion similar to triangle. And the triangular motion of the sun gear causes that the pressure angle and overlap ratio change in a nearly sinusoidal way whose period is the meshing cycle. And there are six turning points in one cycle which are caused by the six obvious mutations of meshing stiffness between the sun gear and three planets in one mesh cycle as shown in Figure 11. Comparing Figures 7 and 11, it can be seen that when the stiffness value changes suddenly at the critical point of meshing, the meshing pressure angle also changes suddenly. Correspondingly, there are also six turning points in one cycle of TVOR as shown in Figure 12. The meshing stiffness of s-p_1 is shown in Figure 6. Because of the TVPA and

Table 1: Basic parameters of the model.

Parameters name	Sun gear	Ring gear	Planet gear	The carrier
Number	1	1	3	1
Number of teeth	10	62	26	—
Mass (kg)	0.28	3.64	0.34	2
Gear module (mm)	2.25	2.25	2.25	—
Standard pressure angle (°)	20	20	20	—
Inertia moment (kg·m^2)	$2.10E-04$	$5.05E-04$	$2.90E-04$	$4.93E-03$
Fault feature frequency (Hz)	31	5	7.95	—
Rotation frequency (Hz)	12	0	2.31	1.67
Meshing frequency (Hz)	103.33	103.33	103.33	103.33

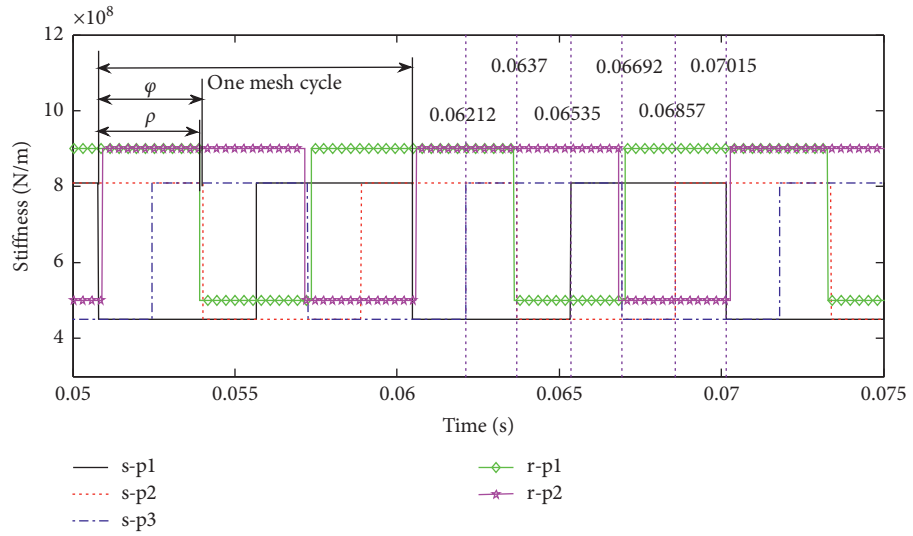

Figure 7: Meshing stiffness of different planets with the sun gear and ring gear.

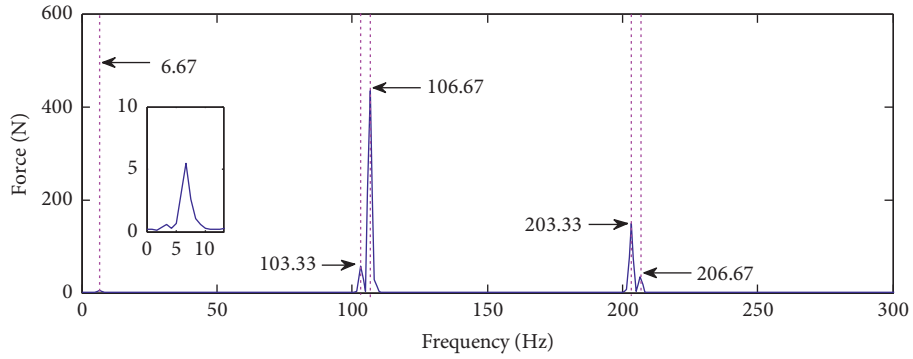

Figure 8: Meshing force spectrum of s-p_1 mesh.

TVOR, the value of meshing stiffness result in small fluctuations on the basis of theoretical value which can be easily observed at the alternation between single-tooth and double-tooth mesh in Figure 6. Figure 13 shows the spectrum of meshing force of s-p_1 in which the meshing frequency and its multiplication can be easily observed. And we can also see that there are more frequency components in the conditions of TVPA and TVOR than that in the constant conditions. This is because TVPA causes the variation of meshing phase as shown in Figure 14. The variation of meshing phase gives rise to phase modulation that produces the additional frequency components. But the variation value is small and its influence on meshing force spectrum reflected in the amplitude and there are more sharp points in the time-varying condition.

3.3. Comparison of Dynamic Response in Different Operating Conditions. To investigate the influence of operating conditions on TVPA and TVMP, the simulation is conducted in different input speeds and torques.

With other conditions unchanged and the input torques being 1500 Nm, 2000 Nm, and 2500 Nm, the TVPA and

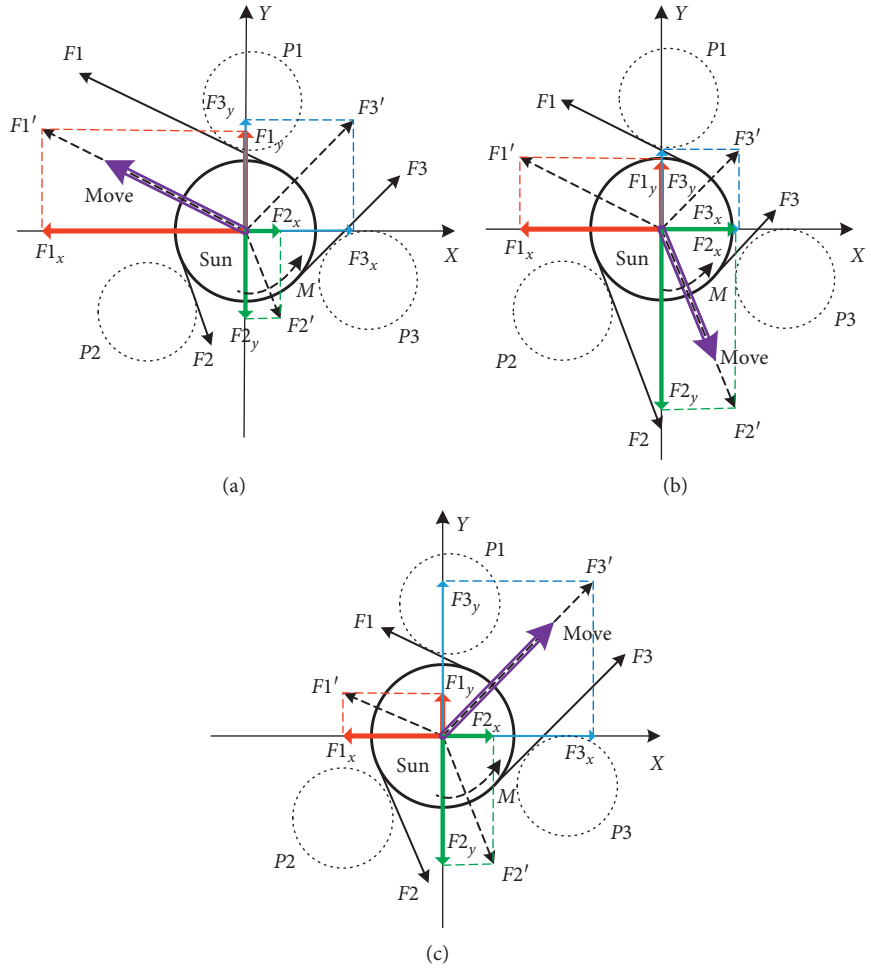

Figure 9: Diagram of meshing force on the sun gear.

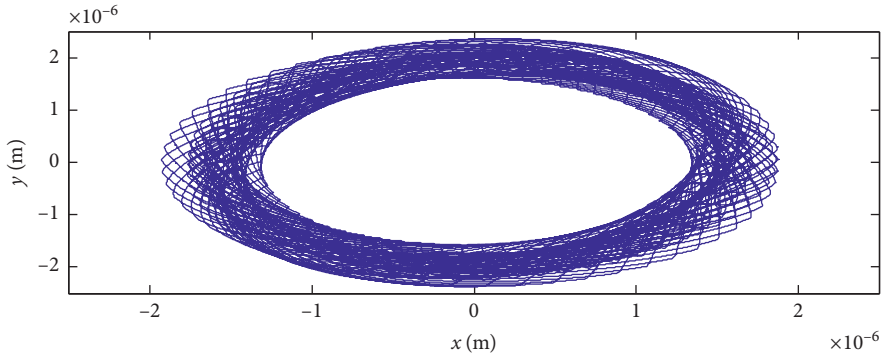

Figure 10: The center track of the sun gear.

TVMP of s-p_1 mesh are shown in Figures 15 and 16, respectively. With the increases of input torque, the range of variation for both of them is also increased. But the period and the form of sine is unchanged, which is nearly independent of the input torque. Also, there are six turning points in one cycle and the moment of them is almost unaffected by the different input torques. In different input torques, the pressure angle and meshing phase variation have the same amplitude modulation frequency. Figure 17 is the spectrum of the force for s-p_1 mesh in different input torques. It is clear that with the increase of input torques, the meshing force is also increased. However, due to the increases of meshing phase variation, the frequency offset will also increase, so there will be a different frequency offset in both sides of meshing frequency. In order to study the influence of phase modulation on the vibration response, the signal energy shown in Figure 18 is calculated (19999 sampling points).

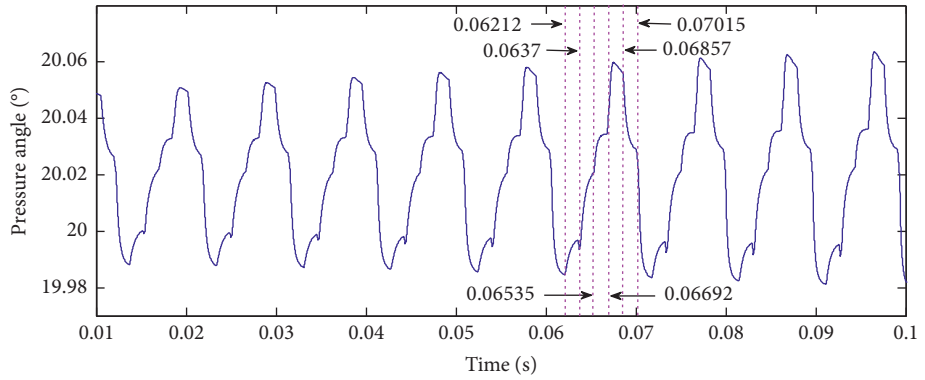

Figure 11: Time-varying pressure angle of s-p_1 mesh.

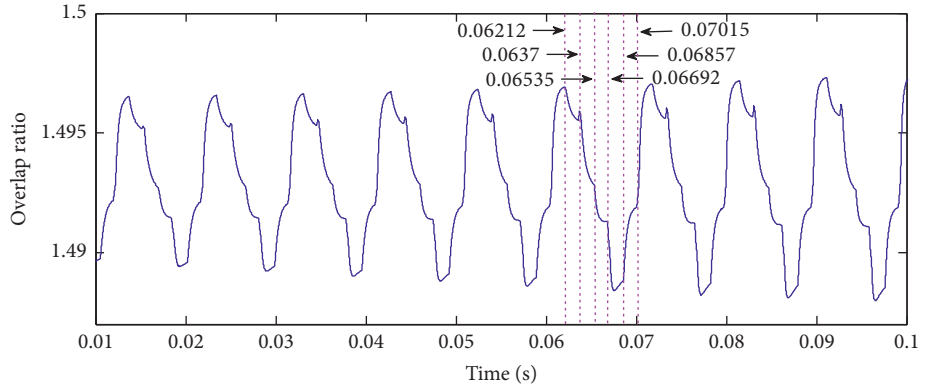

Figure 12: Time-varying overlap ratio of s-p_1 mesh.

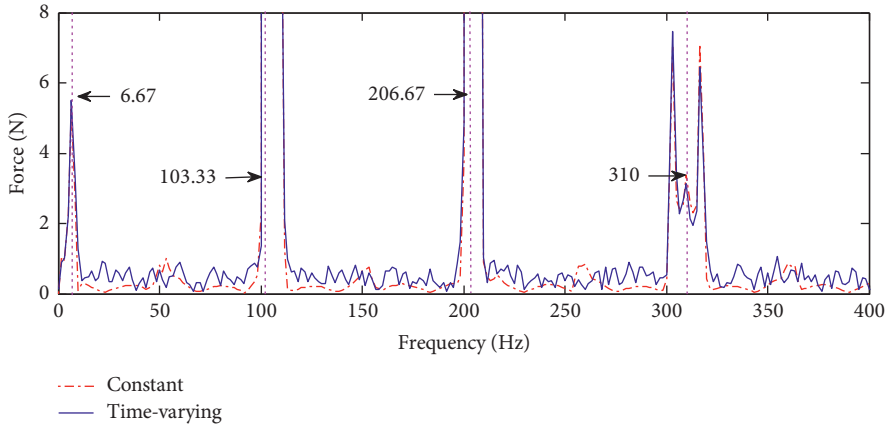

Figure 13: Meshing force spectrum of s-p_1 mesh in constant and time-varying pressure angle and overlap ratio.

The simulation numbers corresponding to the operation conditions are shown in Table 2. For both constant and TVPA conditions, it is calculated under the constant rotation speed and different input torques. And for the same simulation number, both of them are calculated in the same rotation speed and input torque whose energy difference is presented in Figure 19. It is obvious that as the torque increases, the signal energy is also increased linearly. This is because with the increase of torque, the amplitude of meshing vibration will also increase significantly which leads to the increase of signal energy. However, the signal energy of constant pressure angle is larger than that of TVPA. Due to the phase modulation generated by TVPA, the amplitude of some vibrations is suppressed which makes the energy of the signal reduce. As shown in Figure 19, when the torque exceeds 2000 N/m, the suppression of signal vibration by phase modulation will be reduced. Therefore, it can conclude that the suppression of signal vibration by phase modulation does not always increase with the increase of torque.

With change in the input speed and the input torque being constant (input torque = 2500 Nm), the variations of

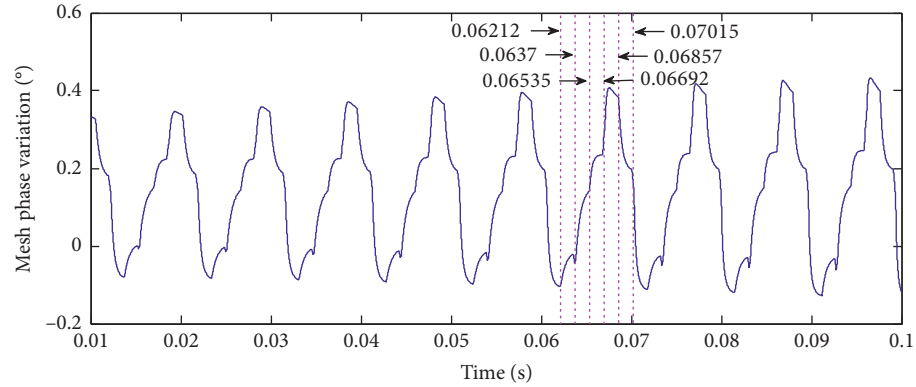

Figure 14: Meshing phase variation of s-p_1 mesh.

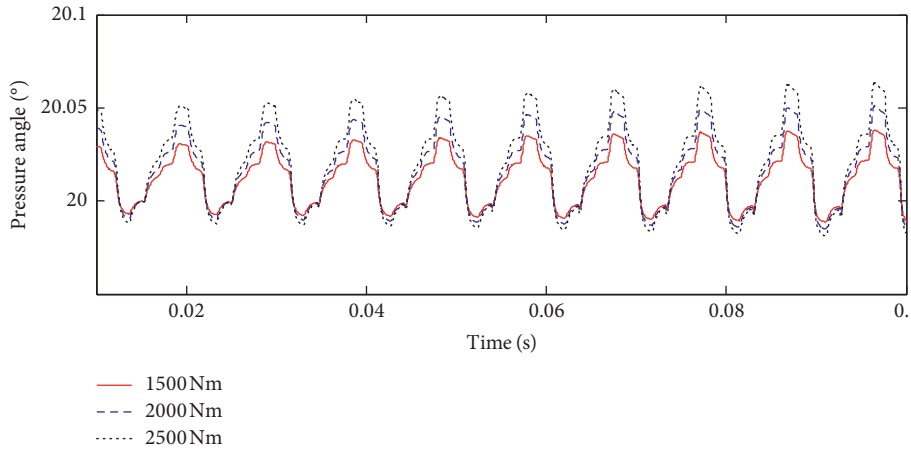

Figure 15: Pressure angle of s-p_1 mesh in different input torques.

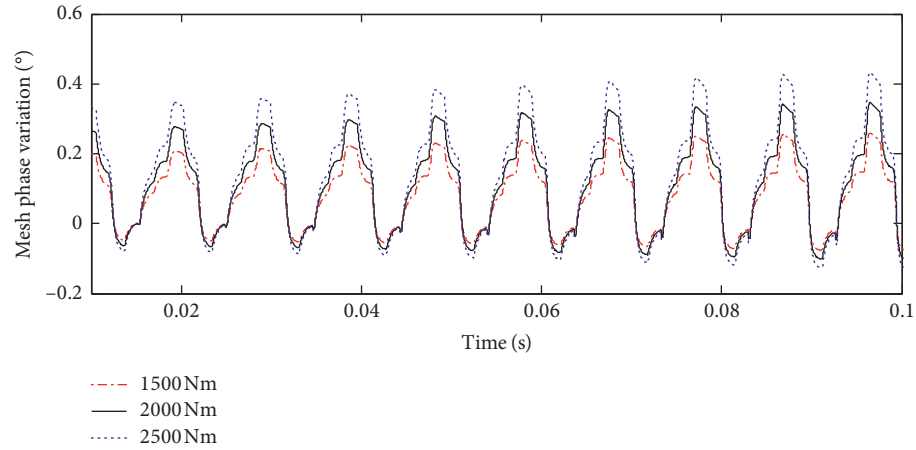

Figure 16: Meshing phase variation of s-p_1 mesh in different input torques.

TVPA and TVMP are shown in Figures 20 and 21. On account of the speed changes, the meshing frequency also changes. From Figures 20 and 21, it can be seen that the input speed influences both the amplitude and the period. However, the variation cycle of pressure angle equaling the meshing cycle is unchanged. And the higher the speed, the higher the variation frequency and amplitude modulation frequency will be. The energy variation of the vibration signal in different speeds is shown in Figure 22. The signal energy for both conditions of constant and TVPA is calculated in the same range of the carrier rotation angle to ensure the comparability of signal energy at different

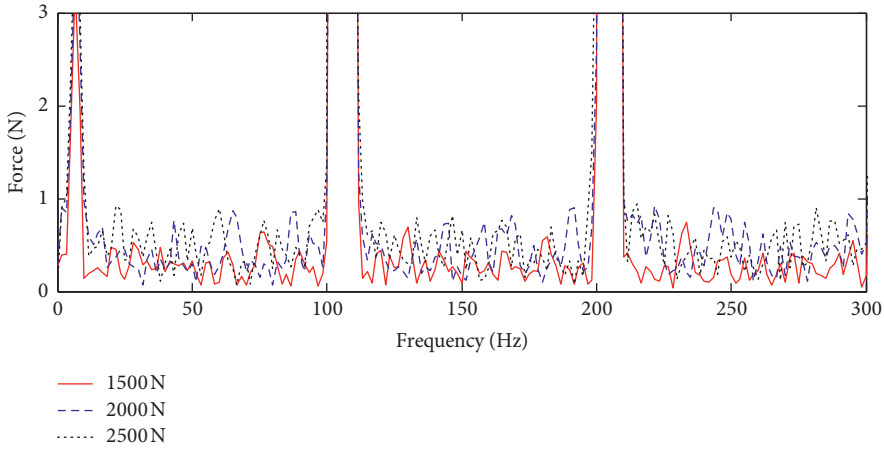

Figure 17: Meshing force spectrum of s-p_1 mesh in different input torques.

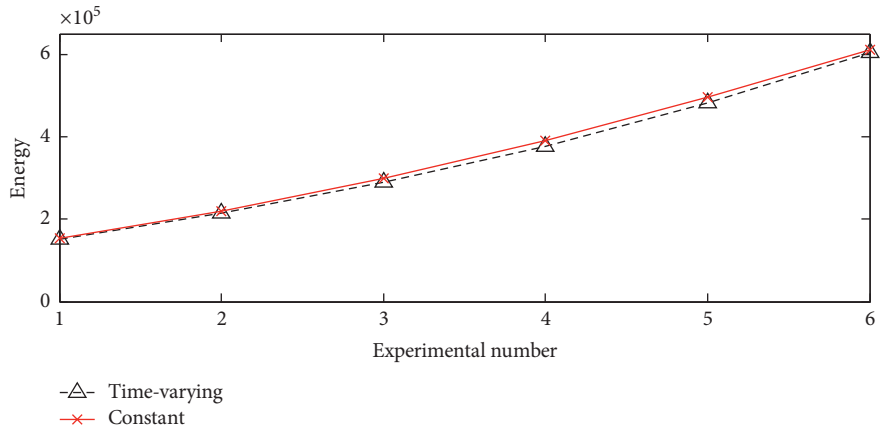

Figure 18: Signal energy of s-p_1 mesh in different input torques.

Table 2: Operating conditions.

Number of operations	1	2	3	4	5	6
Input torque (Nm)	1250	1500	1750	2000	2250	2500
Input speed (rpm)	100	100	100	100	100	100

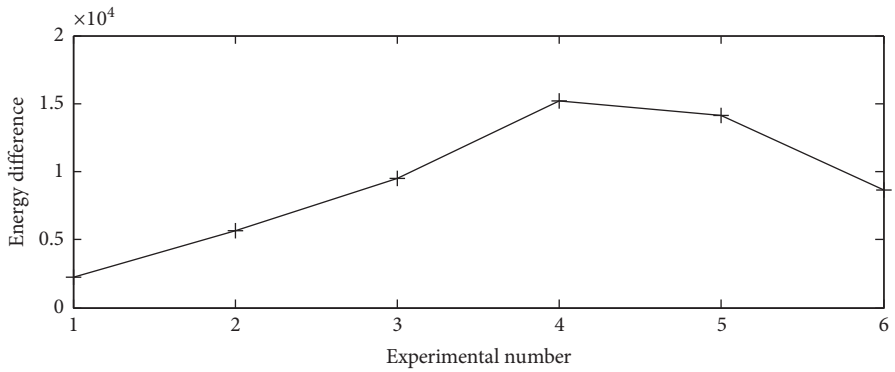

Figure 19: Signal energy difference between constant and time-varying conditions of s-p_1 mesh in different input torques.

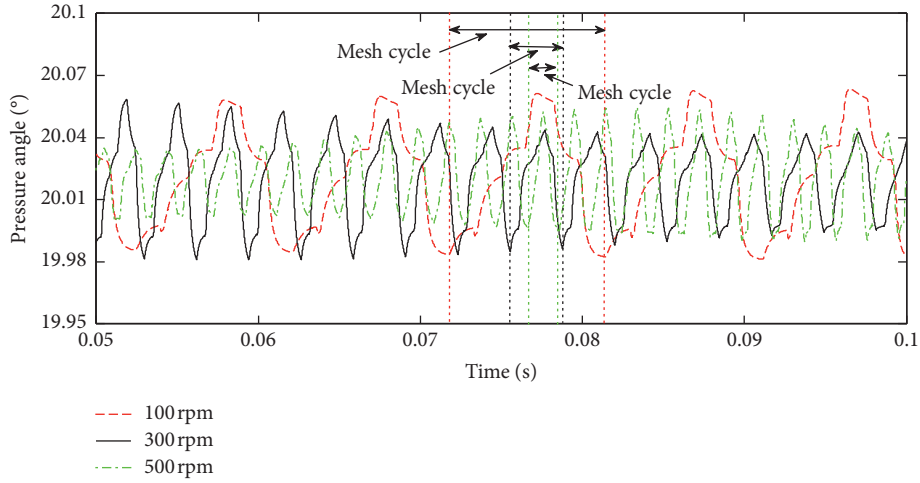

Figure 20: Pressure angle of s-p_1 mesh in different input speeds.

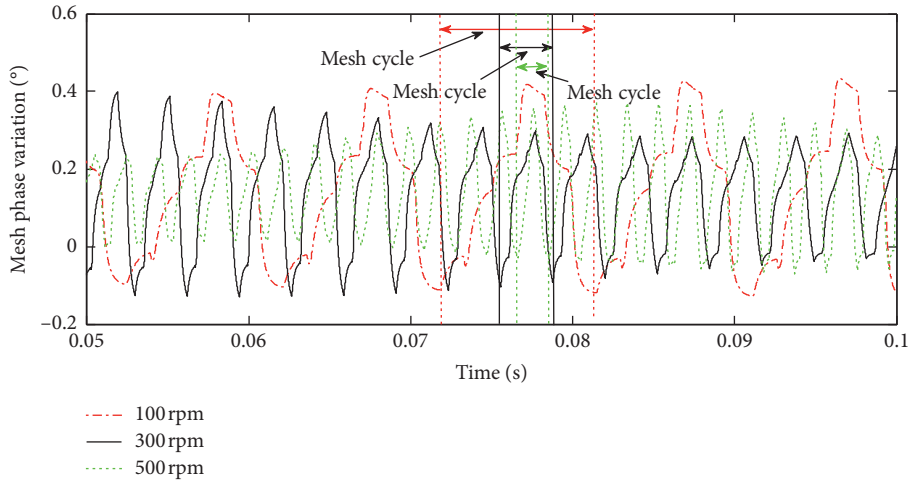

Figure 21: Meshing phase variation of s-p_1 mesh in different input speeds.

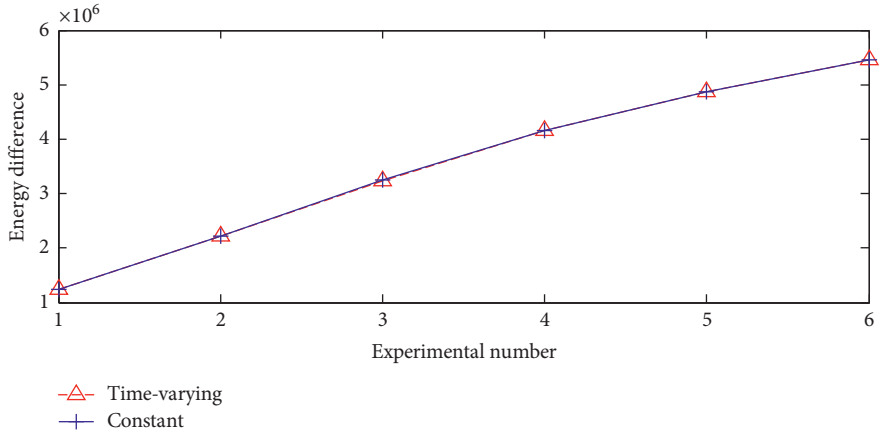

Figure 22: Signal energy of s-p_1 mesh in different input speeds.

rotating speeds. The simulation numbers corresponding to the operation conditions are shown in Table 3. In Figure 22, for both of the constant and TVPA conditions, it is calculated under the constant input torque and different input speeds. And for the same simulation number, both of them are calculated in the same rotation speed and input torque whose energy difference is shown in Figure 23. From Figure 22, it can be observed that the energy in both conditions

Table 3: Operating conditions.

Number of operations	1	2	3	4	5	6
Input torque (Nm)	2500	2500	2500	2500	2500	2500
Input speed (rpm)	100	200	300	400	500	600

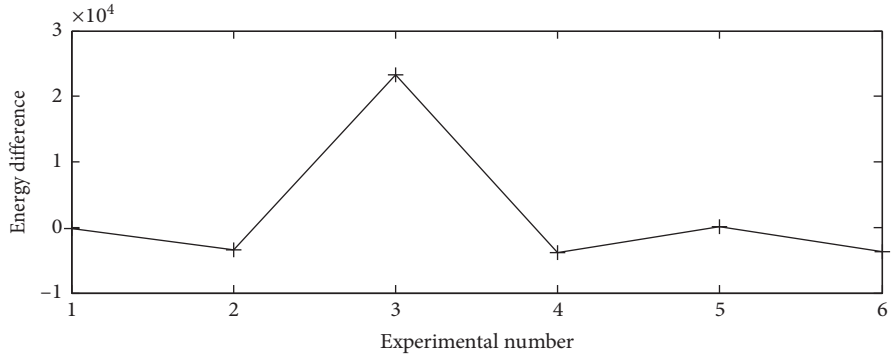

Figure 23: Signal energy difference between constant and TVPA conditions of s-p_1 in different speeds.

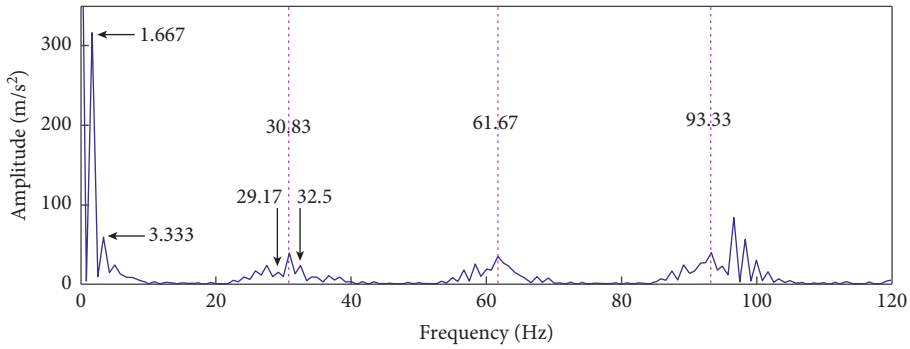

Figure 24: Envelope spectrum of meshing force for s-p_1 mesh in constant pressure angle.

increases linearly with the speed increasing which is because the amplitude of meshing vibration increases significantly. And at the same speed, the energy difference between the two is small except for some special speeds. Therefore, the speed variation mainly affects the phase varying period.

3.4. The Response of the System with Sun Gear Fault. To study the dynamic response of the system when a gear fault occurs, a sun gear fault is taken as an example and introduced into the model. And the fault is expressed by the attenuation of the meshing stiffness. Set the input speed 100 rpm and the input torque 2500 Nm. The vibration signal modulates the rotation frequency of the carrier and fault characteristic frequency of the sun gear. The envelope spectrum of the meshing force for s-p_1 in a constant pressure angle is shown in Figure 24. The rotation frequency of carrier (1.667 Hz) and the fault characteristic frequency (30.83 Hz) of the sun gear can be clearly seen. And Figure 25 shows the comparison of meshing force spectrum for s-p_1 in conditions of constant pressure angle and TVPA. Due to the influence of TVPA, some frequency components in the vibration signal are strengthened and some are weakened. Therefore, the amplitude of the meshing force is not always higher than that of the constant condition, and more frequency components appear. And the response of the system under different fault severity is compared. The meshing phase variation is shown in Figure 26. The more serious the fault severity is, the greater variation of the meshing phase will be when the fault gear tooth is meshing. The variation of meshing phase is affected not only by the fault severity but also by the relative motion between the sun gear and the planet which has been explained in Section 3.2 based on Figure 8. Therefore, the value of the meshing phase variation is not the same when the fault gear tooth and the three planets mesh, respectively, under the same fault severity. Hence the change of meshing phase will affect the phase modulation in the vibration signal and the meshing stiffness can be presented in Figure 27. It can be seen that the more serious the fault severity is, the greater the mutation value is, and so is the meshing stiffness. From the meshing force spectrum which is shown in Figure 28, it can be concluded that with the increase of fault severity, the influence of TVPA is also strengthened. The amplitude of meshing force is different under various fault severity.

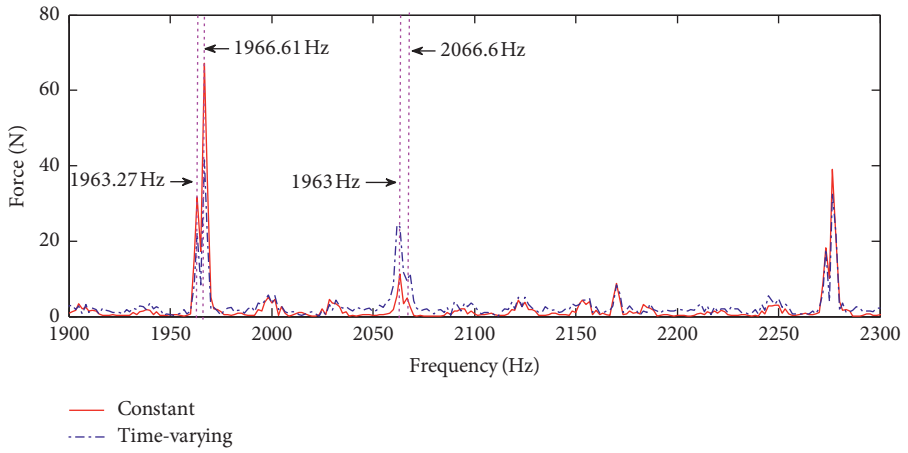

Figure 25: Spectral of meshing force for s-p_1 mesh in constant and time-varying pressure angle.

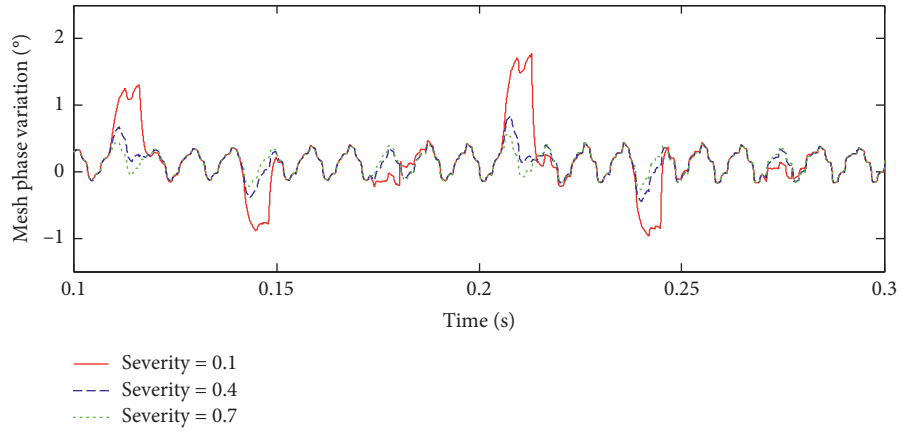

Figure 26: Meshing phase variation of s-p_1 mesh in different fault severity.

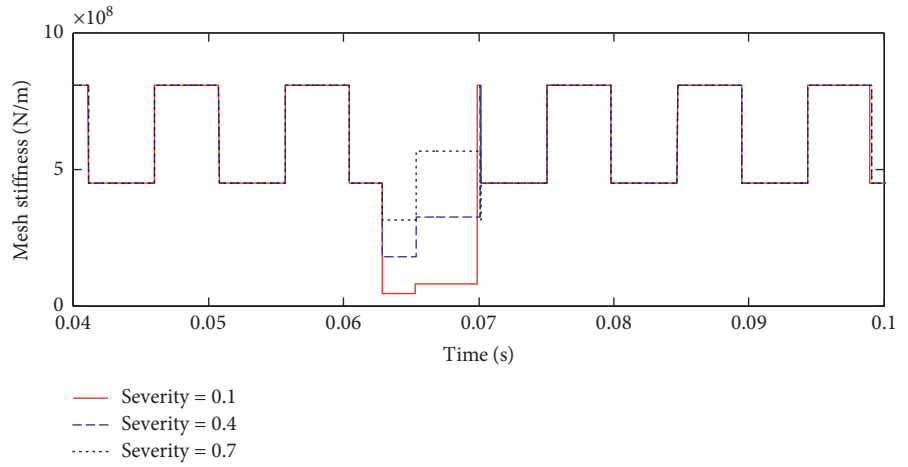

Figure 27: Meshing stiffness in different fault severity.

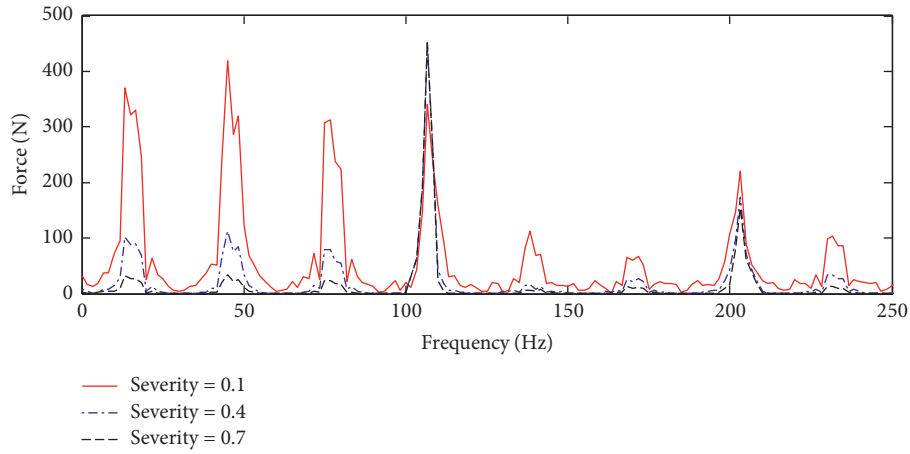

Figure 28: Meshing force of s-p_1 in different fault severity.

4. Conclusions

This paper studies the vibration mechanism of the sun gear when it is set to float in a planetary gearbox and introduces time-varying pressure angle, time-varying overlap ratio, and time-varying meshing phase to investigate the influence of these dynamic parameters on the vibration response of the system under different operating conditions. Subjected to the action of the meshing force, the sun gear presents a triangular movement in the mesh progress. And through analyzing the characteristics of the dynamic responses based on the proposed planetary gearbox model, the conclusions can be obtained:

(1) The time-varying pressure angle and overlap ratio vary with an approximate sine function at the period of meshing cycle, which results in more frequency components in the vibration response. Due to the floating set and bearing deflection, the pressure angle, overlap ratio, and meshing phase also change with time, which causes the meshing stiffness leading to mutation during the mesh progress.

(2) The meshing phase changes with the operating loads and rotation speeds. The rotation speed mainly affects the phase modulation period. When the load increases, the meshing phase variation will increase accordingly. Hence the phase modulation amplitude is mainly affected by the operating loads.

(3) Both the amplitude modulation and phase modulation are affected by gear faults. And when a gear fault occurs, the fault characteristic frequency will be modulated in the meshing force spectrum. The variation of time-varying pressure angle, overlap ratio, and meshing phase will increase with the fault severity.

Considering that the variation of meshing phase affects the meshing stiffness which is a main factor of gear vibration, in the future work, we will study the effect of meshing stiffness on the meshing vibration waveform to reveal the vibration mechanism, and then combine with fault feature extraction algorithm to conduct planetary gearbox fault diagnosis.

Data Availability

The datasets supporting the conclusions of this article are included within the article.

Conflicts of Interest

The authors declare that they have no conflicts of interest.

Acknowledgments

This work was supported by the National Natural Science Foundation of China (51875166, U1813222, and 51705127).

References

[1] Y. Lei, J. Lin, M. J. Zuo, and Z. He, "Condition monitoring and fault diagnosis of planetary gearboxes: a review," *Measurement*, vol. 48, pp. 292–305, 2014.

[2] P. D. McFadden and J. D. Smith, "An explanation for the asymmetry of the modulation sidebands about the tooth meshing frequency in epicyclic gear vibration," *Proceedings of the Institution of Mechanical Engineers, Part C: Journal of Mechanical Engineering Science*, vol. 199, no. 1, pp. 65–70, 1985.

[3] S. Wang, M. Huo, C. Zhang et al., "Effect of mesh phase on wave vibration of spur planetary ring gear," *European Journal of Mechanics - A/Solids*, vol. 30, no. 6, pp. 820–827, 2011.

[4] J. Helsen, F. Vanhollebeke, B. Marrant, D. Vandepitte, and W. Desmet, "Multibody modelling of varying complexity for modal behaviour analysis of wind turbine gearboxes," *Renewable Energy*, vol. 36, no. 11, pp. 3098–3113, 2011.

[5] S. T. Kandukuri, A. Klausen, H. R. Karimi, and K. G. Robbersmyr, "A review of diagnostics and prognostics of low-speed machinery towards wind turbine farm-level health management," *Renewable and Sustainable Energy Reviews*, vol. 53, no. 11, pp. 697–708, 2016.

[6] G. He, K. Ding, X. Wu, and X. Yang, "Dynamics modeling and vibration modulation signal analysis of wind turbine planetary gearbox with a floating sun gear," *Renewable Energy*, vol. 139, pp. 718–729, 2019.

[7] A. S. Milani and A. Shanian, "Gear material selection with uncertain and incomplete data. material performance indices and decision aid model. material performance indices and decision aid model," *International Journal of Mechanics and Materials in Design*, vol. 3, no. 3, pp. 209–222, 2006.

[8] C. Zhou, F. Huang, X. Han, and Y. Gu, "An elastic-plastic asperity contact model and its application for micro-contact analysis of gear tooth profiles," *International Journal of Mechanics and Materials in Design*, vol. 13, no. 3, pp. 335–345, 2017.

[9] C. Fu, X. Ren, Y. Yang, Y. Xia, and W. Deng, "An interval precise integration method for transient unbalance response analysis of rotor system with uncertainty," *Mechanical Systems and Signal Processing*, vol. 107, pp. 137–148, 2018.

[10] S. Wei, Q. Han, Z. Peng, and F. Chu, "Dynamic analysis of parametrically excited system under uncertainties and multi-frequency excitations," *Mechanical Systems and Signal Processing*, vol. 72-73, pp. 762–784, 2016.

[11] E. Wehrle, F. Concli, and L. Cortese, "Design optimization of planetary gear trains under dynamic constraints and parameter uncertainty," in *Proceedings of the 8th ECCOMAS Thematic Conference on Multibody Dynamics , MBD 2017*, pp. 527–538, Free University of Bozen-Bolzano, Bozen-Bolzano, Italy, January 2017.

[12] A. Kahraman, "Load sharing characteristics of planetary transmissions," *Mechanism and Machine Theory*, vol. 29, no. 8, pp. 1151–1165, 1994.

[13] M. Inalpolat and A. Kahraman, "A dynamic model to predict modulation sidebands of a planetary gear set having manufacturing errors," *Journal of Sound and Vibration*, vol. 329, no. 4, pp. 371–393, 2010.

[14] M. Inalpolat and A. Kahraman, "A theoretical and experimental investigation of modulation sidebands of planetary gear sets," *Journal of Sound and Vibration*, vol. 323, no. 3–5, pp. 677–696, 2009.

[15] H. Zhai, C. Zhu, C. Song, H. Liu, and H. Bai, "Influences of carrier assembly errors on the dynamic characteristics for wind turbine gearbox," *Mechanism and Machine Theory*, vol. 103, pp. 138–147, 2016.

[16] J. Lin and R. G. Parker, "Analytical characterization of the unique properties of planetary gear free vibration," *Journal of Vibration and Acoustics*, vol. 121, no. 3, pp. 316–321, 1999.

[17] R. G. Parker and X. Wu, "Vibration modes of planetary gears with unequally spaced planets and an elastic ring gear," *Journal of Sound and Vibration*, vol. 329, no. 11, pp. 2265–2275, 2010.

[18] F. Concli, L. Cortese, R. Vidoni, F. Nalli, and G. Carabin, "A mixed FEM and lumped-parameter dynamic model for evaluating the modal properties of planetary gearboxes," *Journal of Mechanical Science and Technology*, vol. 32, no. 7, pp. 3047–3056, 2018.

[19] Y. Lei, Z. Liu, J. Lin, and F. Lu, "Phenomenological models of vibration signals for condition monitoring and fault diagnosis of epicyclic gearboxes," *Journal of Sound and Vibration*, vol. 369, pp. 266–281, 2016.

[20] L. Liu, X. Liang, and M. J. Zuo, "Vibration signal modeling of a planetary gear set with transmission path effect analysis," *Measurement*, vol. 85, pp. 20–31, 2016.

[21] X. Liang, M. J. Zuo, and M. R. Hoseini, "Vibration signal modeling of a planetary gear set for tooth crack detection," *Engineering Failure Analysis*, vol. 48, pp. 185–200, 2015.

[22] T. Yang, S. Yan, and Z. Han, "Nonlinear model of space manipulator joint considering time-variant stiffness and backlash," *Journal of Sound and Vibration*, vol. 341, pp. 246–259, 2015.

[23] J.-f. Shi, X.-f. Gou, and L.-y. Zhu, "Modeling and analysis of a spur gear pair considering multi-state mesh with time-varying parameters and backlash," *Mechanism and Machine Theory*, vol. 134, pp. 582–603, 2019.

[24] H. Zhang, C. Qi, J. Fan, S. Dai, and B. You, "Vibration characteristics analysis of planetary gears with a multi-clearance coupling in space mechanism," *Energies*, vol. 11, no. 10, p. 2687, 2018.

[25] M. Zhao and J. C. Ji, "Nonlinear torsional vibrations of a wind turbine gearbox," *Applied Mathematical Modelling*, vol. 39, no. 16, pp. 4928–4950, 2015.

[26] A. Singh, "Load sharing behavior in epicyclic gears: physical explanation and generalized formulation," *Mechanism and Machine Theory*, vol. 45, no. 3, pp. 511–530, 2010.

[27] Y. Li, K. Ding, G. He, and H. Lin, "Vibration mechanisms of spur gear pair in healthy and fault states," *Mechanical Systems and Signal Processing*, vol. 81, pp. 183–201, 2016.

[28] J. Parra and C. M. Vicuña, "Two methods for modeling vibrations of planetary gearboxes including faults: comparison and validation," *Mechanical Systems and Signal Processing*, vol. 92, pp. 213–225, 2017.

[29] Z. Feng and M. J. Zuo, "Vibration signal models for fault diagnosis of planetary gearboxes," *Journal of Sound and Vibration*, vol. 331, no. 22, pp. 4919–4939, 2012.

[30] X. Liu, Y. Yang, and J. Zhang, "Resultant vibration signal model based fault diagnosis of a single stage planetary gear train with an incipient tooth crack on the sun gear," *Renewable Energy*, vol. 122, pp. 65–79, 2018.

[31] Z. G. Chen and Y. M. Shao, "Dynamic features of a planetary gear system with tooth crack under different sizes and inclination angles," *Journal of Vibration and Acoustics–Transactions of the ASME*, vol. 135, Article ID 031004, 2013.

[32] R. G. Parker, "A physical explanation for the effectiveness of planet phasing to suppress planetary gear vibration," *Journal of Sound and Vibration*, vol. 236, no. 4, pp. 561–573, 2000.

[33] R. G. Parker and J. Lin, "Mesh phasing relationships in planetary and epicyclic gears," *Journal of Mechanical Design*, vol. 126, no. 2, pp. 365–370, 2004.

[34] D. Peng, W. A. Smith, P. Borghesani, R. B. Randall, and Z. Peng, "Comprehensive planet gear diagnostics: use of transmission error and mesh phasing to distinguish localised fault types and identify faulty gears," *Mechanical Systems and Signal Processing*, vol. 127, pp. 531–550, 2019.

[35] D. Peng, W. A. Smith, R. B. Randall, and Z. Peng, "Use of mesh phasing to locate faulty planet gears," *Mechanical Systems and Signal Processing*, vol. 116, pp. 12–24, 2019.

[36] W. Kim, J. Y. Lee, and J. Chung, "Dynamic analysis for a planetary gear with time-varying pressure angles and contact ratios," *Journal of Sound and Vibration*, vol. 331, no. 4, pp. 883–901, 2012.

[37] Z. X. He, Q. T. liu, and L. H. Chang, "Transverse–torsional vibrations of the high–speed planetary gear transmission," *The Open Mechanical Engineering Journal*, vol. 8, no. 1, pp. 396–401, 2014.